

**CFD simulation of bubbly flow around an obstacle in a vertical pipe with
a focus on breakup and coalescence modelling**

Tas-Köhler, S.; Neumann-Kipping, M.; Liao, Y.; Krepper, E.; Hampel, U.;

Originally published:

November 2020

International Journal of Multiphase Flow 135(2021), 103528

DOI: <https://doi.org/10.1016/j.ijmultiphaseflow.2020.103528>

Perma-Link to Publication Repository of HZDR:

<https://www.hzdr.de/publications/Publ-31210>

Release of the secondary publication
on the basis of the German Copyright Law § 38 Section 4.

CC BY-NC-ND

CFD simulation of bubbly flow around an obstacle in a vertical pipe with a focus on breakup and coalescence modelling

Sibel Tas-Koehler ^{a*}, Martin Neumann-Kipping ^b, Yixiang Liao ^a, Eckhard Krepper ^a, Uwe Hampel ^{a,b}

^a Helmholtz-Zentrum Dresden-Rossendorf, Institute of Fluid Dynamics, Bautzner Landstr. 400, 01328 Dresden, Germany

^b Technische Universität Dresden, Chair of Imaging Techniques in Energy and Process Engineering, 01062 Dresden, Germany

* CORRESPONDING AUTHOR (E-MAIL: s.tas@hzdr.de)

ABSTRACT

In the present study, we assessed the capabilities of Eulerian-Eulerian CFD two-phase flow simulation with the homogeneous Multiple Size Group Model (MUSIG) and consideration of breakup and coalescence under three-dimensional flow conditions. We compared void fraction, bubble size and bubble velocity distributions against experimental data from vertical gas-disperse two-phase flow in a pipe with a flow obstruction. The simulation results generally agree well upstream the obstacle, where we have a typically developed pipe flow. Downstream of the obstacle void fraction is overpredicted while bubble velocity is underpredicted. The bubble size distribution has no clear trend. With higher liquid velocities, the deviations increase. As a conclusion, the simulation has difficulties to balance the gas fraction in the strong vortex in the shadow of the obstacle. Here further model improvement is needed.

Keywords: CFD, bubbly flow, model validation, bubble breakup, bubble coalescence

Nomenclature

Latin symbols

d_B	bubble diameter [m]	S_K	source term due to turbulent kinetic energy [N·m ⁻² ·s ⁻¹]
d_{cr}	critical bubble diameter [m]	S_ε	source term due to turbulent dissipation rate [N·m ⁻² ·s ⁻²]
C_D	drag coefficient [-]	S_ω	source term due to turbulent frequency [N·m ⁻⁴]
C_L	lift coefficient [-]	u	velocity [m·s ⁻¹]
C_W	wall lubrication coefficient [-]	Greek symbols	
C_{VM}	virtual mass coefficient [-]	α	gas volume fraction [-]
d_\perp	maximum horizontal bubble dimension [mm]	ρ	density [kg·m ⁻³]
Eo_\perp	Eötvös number depending on d_\perp [-]	τ	bubble-induced time scale [s]
Eo	Eötvös number [-]	τ_{ij}^{Lam}	laminar stress tensor [kg·m ⁻¹ ·s ⁻²]
F_D	drag force per unit volume [N·m ⁻³]	τ_{ij}^{Turb}	turbulent stress tensor [kg·m ⁻¹ ·s ⁻²]
F_L	lift force per unit volume [N·m ⁻³]	ω	turbulence frequency [s ⁻¹]
F_W	wall lubrication force per unit volume [N·m ⁻³]	ν_L^{turb}	kinematic viscosity [m ² ·s ⁻¹]
F_{Disp}	turbulent dispersion force per unit volume [N·m ⁻³]	σ_{TD}	Schmidt number [-]
F_{VM}	virtual mass force per unit volume [N·m ⁻³]	ε	turbulence dissipation rate [m ² ·s ⁻³]
k	phase indicator, turbulent kinetic energy [m ² ·s ⁻²]	Subscripts	
M_i	source term in i-th direction [kg·m ⁻² ·s ⁻²]	B	bubble
p	pressure [Pa]	L	liquid phase
Re	Reynolds number [-]	G	gas phase

26

27 Acronyms

28 BIT: Bubble-Induced Turbulence

29 CFD: Computational Fluid Dynamics

30 FAD: Favre-Averaged Drag

31 MUSIG: Multiple Size Group Model

32 SST: Shear Stress Transport

33 UFXCT: Ultrafast X-ray Computed Tomography

1. Introduction

Bubbly flows are encountered in different industrial applications such as chemical, petroleum and nuclear engineering. In these applications, it is important to know the flow behavior to enhance efficiency such as in chemical reactors or to increase safety margins such as in nuclear reactors. For this purpose, computational fluid dynamics (CFD) that is based on the Eulerian-Eulerian framework has become a popular tool. However, the accuracy of CFD simulations highly relies on correct modeling of phase interactions including interfacial forces (i.e. drag, lift, wall lubrication, turbulent dispersion, and virtual mass), bubble-induced turbulence (BIT) and bubble breakup/coalescence. The modeling of the latter one is possible by a poly-dispersed approach in which the gas phase is divided into a number of size groups. In most of the industrial applications, there is a wide distribution of bubble sizes and a non-uniform radial gas fraction profiles. Thus, the correct prediction of bubble size by breakup and coalescence plays an important role in the accuracy of CFD simulations.

For adiabatic bubbly flow, numerous numerical studies were done, especially focusing on the interfacial forces and BIT. Frank *et al.* (2008) indicated for two-phase pipe flow that a mono-dispersed simulation model, including the Tomiyama lift force, the Frank wall lubrication force, the Favre-averaged drag (FAD) turbulent dispersion force and the Shear Stress Turbulence (SST) model, gives good agreement with the experimental data in terms of gas void fraction. Besagni *et al.* (2018) investigated the effects of the interfacial forces for small-scale and large-scale bubble columns with the mono-dispersed approach. The authors suggested a baseline model with the following interfacial forces: the Tomiyama drag force, the Antal wall lubrication force and the Lopez or Burns turbulence dispersion force. Jin *et al.* (2019) investigated the influence of different models of interfacial forces on the phase distribution for vertical and inclined bubbly flow. They reported that the combination of the Ishii-Zuber drag force, the Saffman-Mei lift force, the Hosokawa wall lubrication force and the FAD turbulent dispersion force provides good radial void fraction results for vertical bubbly flow. Rzehak *et al.* (2012) examined different wall lubrication force models in case of bubbly flow. They compared the Antal, Tomiyama and Hosokawa wall force models and found that the Hosokawa model provides the best performance. Jareteg *et al.* (2017) investigated the effect of a virtual mass force on the stability of the bubbly flow simulations. The authors showed that the implementation of virtual mass force importantly changes the growth rate of void instabilities. Colombo *et al.* (2019) showed the capability of Eulerian-Eulerian CFD for a bubbly flow in a pipe and square duct by focusing on the lift and turbulence forces. According to the results, the effect of turbulence on the phase distribution is as important as the lift force. They further concluded that the wall lubrication force is not necessary if the near-wall region is appropriately resolved.

BIT was also taken into account in many studies. Rzehak *et al.* (2017) developed a closure model for bubbly flow simulations including bubble forces and BIT. However, they did not consider bubble breakup and coalescence yet. The simulation results were compared to experimental data for gas volume fraction, axial liquid velocity and turbulent kinetic energy. Although an overall satisfying agreement between experiments and simulations was found, the authors pointed out that further improvements in turbulence modeling and implementation of bubble breakup/coalescence are highly necessary. Colombo *et al.* (2015) presented the validation of the two-phase Eulerian-Eulerian mono-dispersed model for pipe flow by using experimental data from 6 different literature sources. They reported that their BIT model gives better results in terms of r.m.s velocity fluctuations as compared to Troshko *et al.* (2001) and Rzehak *et al.* (2013). Besagni *et al.* (2018) reported that while BIT inclusion causes convergence problems for large-scale bubble columns, the model of Sato improves the results slightly compared to Simonin *et al.* (1990) for small-scale bubble columns. Parekh *et al.* (2018) compared Launder, Reece, Rodi (LRR) RSM and Speziale-Sarkar-Gatski (SSG) RSM turbulence models as well as the SST model

for air-water pipe flow to capture the anisotropy of turbulent fluctuations concerning BIT. The simulation results showed that predictions of LRR and SSG RSM including BIT are comparable to the SST model over radial profiles of the liquid velocity and gas fraction. However, all three models underestimated the wall peaks of the turbulent kinetic energy and Reynolds stresses by comparing them with the experimental data. Liao *et al.* (2018) applied the MUSIG approach for air-water bubbly flow to test the performance of the BIT model developed by Ma *et al.* (2017). The results showed that the model of Ma *et al.* (2017) predicts the radial gas void fraction and gas velocity well compared to the experiments.

Bubble breakup and coalescence was less considered in the literature compared to interfacial forces and BIT. Frank *et al.* (2008) showed that the inhomogeneous MUSIG (i-MUSIG) model predicts radial void fraction profiles well but further investigation is needed in terms of bubble breakup and coalescence. Liao *et al.* (2015) performed simulations to assess the capability of the bubble breakup and coalescence modeling which was proposed by Liao *et al.* (2011). The results showed that the mean bubble size is overestimated at low superficial liquid velocities and is slightly underestimated at high superficial liquid velocities. The authors concluded that further studies are necessary considering BIT, which has a high impact on bubble breakup and coalescence mechanisms.

While CFD codes have meanwhile been well qualified for simple pipe and column geometries there is yet little analysis and qualification for more complex three-dimensional flow domains. One reason is the lack of appropriate experimental validation data. Prasser *et al.* (2008) provided such data for bubbly flow in a pipe with a semi-circular obstacle using a wire-mesh sensor. Follow-up CFD simulations assuming mono-disperse bubbles provided good void fraction estimation upstream the obstacle but overestimated void fraction downstream. Krepper *et al.* (2009) used the i-MUSIG model including bubble breakup and coalescence and found that the standard breakup and coalescence models (Luo *et al.* (1996), Prince *et al.* (1990)) do not predict the bubble size distribution (BSD) well. Continuing in this line the objectives of this study were to show the capability of bubble breakup and coalescence modelling (Liao *et al.* (2015)) under complex flow conditions with new high-resolution two-phase flow data around an obstacle in a pipe. The 3D flow field was simulated for two different liquid velocity conditions using the MUSIG model. For the simulations, a baseline model for air-water bubbly flow was applied that includes the model of Rzehak *et al.* (2017) for interfacial forces, the model of Liao *et al.* (2015) for the bubble breakup/coalescence and the model of Ma *et al.* (2017) for the BIT. Moreover, the performance of a new discretization scheme for bubble coalescence and breakup modelling developed by Liao (2020) was also tested within this work.

By validation against experimental benchmark data, the capability of bubble breakup/coalescence model is demonstrated in terms of gas volume fraction, gas velocity, mean bubble diameter and bubble size distribution with the aid of Ultrafast X-ray Computed Tomography (UFXCT) measurements (Neumann-Kipping *et al.* (2020)). Furthermore, hydrodynamics of the 3D bubbly flow is analyzed and bubble interaction within the vortex region formed by the obstacle is examined under different liquid velocities. Thus, this paper contributes to two main fields: (i) the assessment of breakup and coalescence model accuracy under 3D flow conditions: (ii) understanding of two-phase flow hydrodynamics in complex geometries.

2. Experimental setup

The experimental study used for validation is described in detail in Neumann-Kipping *et al.* (2020). The experiments were performed in an acrylic pipe with an inner diameter of 54 mm and a total length of 4950 mm. A semi-circular obstacle that blocks half of the inner pipe cross-section was utilized to generate 3D flow fields. A sketch of the test facility, as well as the gas injection module, is illustrated

in Figure 1. The experiments were performed at 4 bar pressure and a liquid temperature of 30°C. Deionized water and compressed air are injected at the bottom of the test section as the liquid and gas phase, respectively.

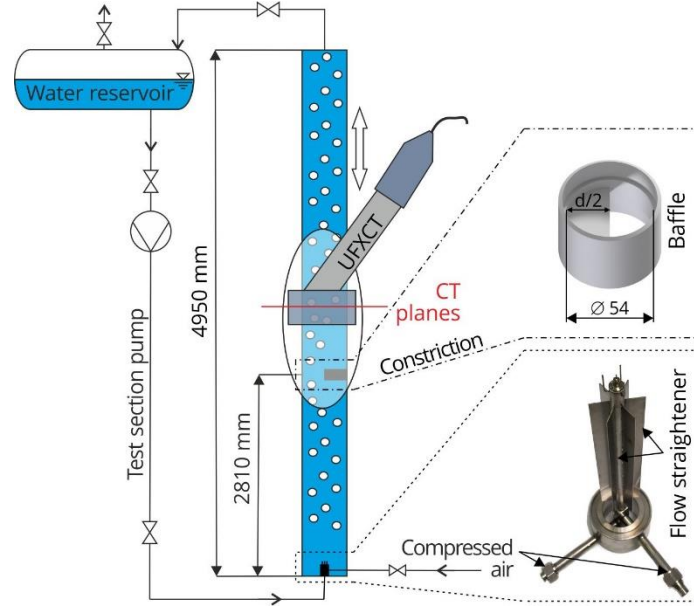


Figure 1: Schematic representations of the vertical test section (left) with details of the gas injection module (bottom right) and the flow obstacle for generation of three-dimensional flow fields (top right). Various operating conditions in bubbly flow regime were tested by setting appropriate liquid and gas flow rates. Two operating conditions that are used for the present study are described in Table 1.

Table 1: Experimental operating conditions based on combinations of liquid and gas superficial velocities.

Test run	j_l [m·s ⁻¹]	j_g [m·s ⁻¹]
#072	0.4050	0.0368
#074	1.0170	0.0368

Ultrafast X-ray computed tomography (UFXCT), which is a well-established non-invasive imaging technique for multiphase flow, was applied to quantitatively analyze the distribution of gas and liquid within the test section. The UFXCT scanner can be freely moved to allow for imaging of the flow field in several imaging planes up- and downstream of the flow obstacle, as depicted in Table 2 (Neumann-Kipping *et al.* (2020)). By the means of UFXCT, cross-sectional information of the gas velocity and gas volume fraction, as well as bubble size distribution were determined. A detailed discussion of measurement uncertainty UFXCT and quality evaluation of the experimental results can be found in Neumann-Kipping *et al.* (2020). Here, the time-averaged cross-sectional gas holdup and axial gas velocity were used to calculate the inlet superficial gas velocity. This estimated velocity was compared to the set value, showing maximum deviation of $\pm 15\%$ for all cases.

Table 2: Image plane identifier along the vertical test section with relative distances of the upper image plane to the center of the flow constriction.

Identifier	A	B	C	D	E	F	G	H	I
Z (mm)	-200	-60	0	5	20	50	100	200	400

3. Numerical method

3.1 General remarks

For simulation, the geometry was defined as a vertical half tube using a symmetry xz-plane. All simulations were performed using the solver ANSYS CFX 19.2. The fluid domain was modelled from 1.5 m upstream to 1 m downstream the obstacle (Figure 2). The results were obtained by applying the Multiple Size Group Model (Lo (1996)). The dispersed phase was divided into 15 size fractions where the bubble diameters ($d_b = 0 \dots 15 \text{ mm}$) were defined with equidistant bubble diameter. As inlet conditions, a developed flow condition for liquid velocity, liquid turbulent kinetic energy and turbulent dissipation obtained from previous single-phase simulations were assigned. Further, experimentally determined radial void fraction and bubble size distribution at the largest upstream ($Z = -211 \text{ mm}$) position were applied. A constant pressure was defined as outlet condition. All the simulations were performed at steady state condition. Turbulence was modeled only for the liquid phase using the SST model (Menter (1994)). The dimensionless wall distance value for the liquid phase y^+ was kept greater than 30. The single-phase law of wall was used for the wall treatment. The density change of gas was considered by treating the gas phase as ideal gas and its change depending on the height was considered according to

$$\rho_G(P) = \rho_{G,atm} \frac{P_H}{P_{atm}}, \quad (1)$$

where P_{atm} is the atmospheric pressure and $\rho_{G,atm}$ is the gas density depending on atmospheric pressure. P_H is the pressure depending on the height and it is calculated with the following equation:

$$P_H = 4P_{atm} + \rho_L gh. \quad (2)$$

Here, ρ_L is the liquid density, g is the gravitational acceleration and h is the height. On the pipe wall, a no-slip condition was applied for the liquid phase and a free-slip condition for the gas phase. The convergence criteria were set to $RMS < 10^{-6}$.

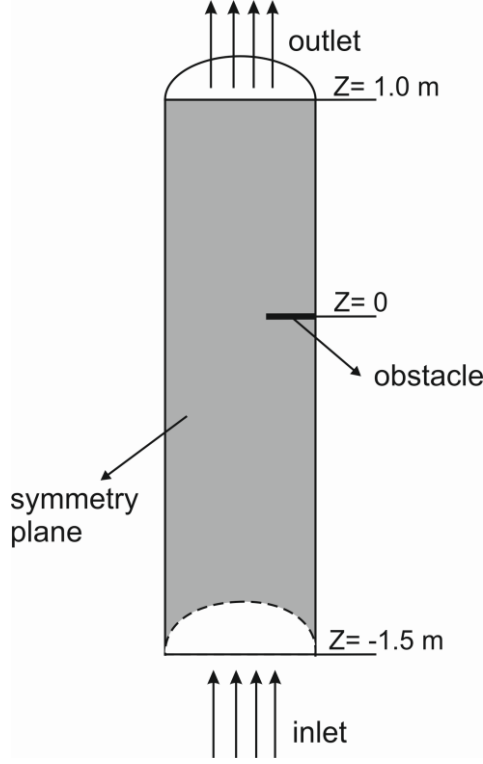


Figure 2: Schematic view of computational domain.

3.2 Governing equations

An Eulerian-Eulerian two-fluid model was applied in the present simulations. This framework defines every phase by a set of averaged conservation equations. Detailed information and derivations of the conservation equations were given by Yeoh *et al.* (2009). Since there is no heat transfer considered for the current study, the conservation equations include only the continuity equation

$$\frac{\partial(\alpha_k \rho_k)}{\partial t} + \frac{\partial}{\partial x_i}(\alpha_k \rho_k \mathbf{u}_{i,k}) = 0 \quad (3)$$

and the momentum equation

$$\begin{aligned} \frac{\partial}{\partial t}(\alpha_k \rho_k \mathbf{u}_{i,k}) + \frac{\partial}{\partial x_i}(\alpha_k \rho_k \mathbf{u}_{i,k} \mathbf{u}_{j,k}) \\ = -\alpha_k \frac{\partial p_k}{\partial x_i} + \frac{\partial}{\partial x_j}[\alpha_k (\tau_{ij,k}^{Lam} + \tau_{ij,k}^{Turb})] + \alpha_k \rho_k \mathbf{g}_i + \mathbf{M}_{i,k}. \end{aligned} \quad (4)$$

Here, k is the phase indicator, α is the volume fraction, ρ is the density, \mathbf{u}_i is the velocity component in the i -th direction, p is the pressure, τ_{ij}^{Lam} is the laminar stress tensor, τ_{ij}^{Turb} is the turbulence stress tensor and \mathbf{M}_i is the source term in the i -th direction, which will be explained in the following section.

3.3 Interfacial momentum transfer

The Eulerian-Eulerian framework considers interpenetrating continua and therefore closure models for interfacial momentum transfer are applied by means of a source term of the form

$$\mathbf{M}_k = \mathbf{F}_D + \mathbf{F}_L + \mathbf{F}_W + \mathbf{F}_{Disp} + \mathbf{F}_{VM} \quad (5)$$

that is added in the momentum equation including drag force \mathbf{F}_D , lift force \mathbf{F}_L , wall lubrication force \mathbf{F}_W , turbulent dispersion force \mathbf{F}_{Disp} and virtual mass force \mathbf{F}_{VM} . In the present study, all these forces were considered for the simulations.

The drag force

$$\mathbf{F}_D = -\frac{3}{4} \frac{C_D}{d_B} \alpha \rho_L |\mathbf{u}_G - \mathbf{u}_L| (\mathbf{u}_G - \mathbf{u}_L) \quad (6)$$

acts opposite to the relative motion of bubbles relative to the surrounding liquid. Here, d_B is the bubble diameter, α is the gas void fraction, ρ_L is the liquid density, \mathbf{u}_G is the gas velocity, \mathbf{u}_L is the liquid velocity and C_D is the drag coefficient calculated by the correlation of Ishii *et al.* (1979).

The lift force

$$\mathbf{F}_L = -C_L \alpha \rho_L (\mathbf{u}_G - \mathbf{u}_L) \times (\nabla \times \mathbf{u}_L) \quad (7)$$

occurs due to the interaction of the bubble with the shear flow of the liquid. Here, C_L is the lift force coefficient and determined by Tomiyama *et al.* (2002). The lift force coefficient changes its sign from positive to negative if the bubble diameter exceeds a critical bubble diameter. For water-air at ambient conditions, as is the case here, this critical diameter has a value of $d_{cr} = 5.8 \text{ mm}$. (Tomiyama *et al.* (1998)).

The wall lubrication force

$$\mathbf{F}_W = \frac{2}{d_B} C_W \rho_L \alpha |\mathbf{u}_G - \mathbf{u}_L|^2 \hat{\mathbf{y}} \quad (8)$$

drives the bubbles away from the wall to avoid the maximum gas fraction at the wall. Here, $\hat{\mathbf{y}}$ is the unit normal perpendicular to the wall and C_W is the wall force coefficient. The model of Hosokawa *et al.* (2002) was applied to predict the wall force coefficient.

The turbulent dispersion force

$$\mathbf{F}_{Disp} = -\frac{3}{4} \frac{C_D}{d_B} \alpha \rho_L |\mathbf{u}_G - \mathbf{u}_L| \frac{\nu_L^{turb}}{\sigma_{TD}} \left(\frac{1}{(1-\alpha)} + \frac{1}{\alpha} \right) \nabla \alpha \quad (9)$$

describes the impact of liquid phase turbulent fluctuations on the gas phase. Here, ν_L^{turb} is the kinematic viscosity of the liquid phase and σ_{TD} is the Schmidt number, generally taken as 0.9. The turbulent dispersion force was modeled by Burns *et al.* (2004).

The virtual mass force

$$\mathbf{F}_{VM} = -C_{VM} \alpha \rho_L \left(\frac{D_G \mathbf{u}_G}{Dt} - \frac{D_L \mathbf{u}_L}{Dt} \right) \quad (10)$$

acts on the bubbles in case of bubble sudden acceleration. Here, C_{VM} is the virtual mass coefficient, which was set to 0.5 for the simulations. Table 3 shows the equations for calculating the force coefficients.

Table 3: Mathematical description for interfacial force coefficients.

Force	Reference	Mathematical description
Drag	Ishii <i>et al.</i> (1979)	$C_D = \max[C_{Dsphere}, \min(C_{Dellipse}, C_{Dcap})]$
		$C_{Dsphere} = \frac{24}{Re_d} (1 + 0.1 Re_d^{3/4}), C_{Dellipse} = \frac{2}{3} \sqrt{Eo}, C_{Dcap} = \frac{8}{3}$
Lift	Tomiyama <i>et al.</i> (2002)	$C_L = \begin{cases} \min[0.288 \tanh(0.121 Re), f(Eo_\perp)] & Eo_\perp < 4 \\ f(Eo_\perp) & 4 < Eo_\perp < 10 \\ -0.27 & 10 < Eo_\perp \end{cases}$
		$f(Eo_\perp) = 0.00105 Eo_\perp^3 - 0.0159 Eo_\perp^2 - 0.0204 Eo_\perp + 0.474$
		$Eo_\perp = \frac{g(\rho_L - \rho_L)d_\perp^2}{\sigma} \quad d_\perp = d_B \sqrt[3]{1 + 0.163 Eo^{0.757}}$
Wall lubrication	Hosokawa <i>et al.</i> (2002)	$C_W(y) = f(Eo) \left(\frac{d_B}{2y}\right)^2, \quad f(Eo) = 0.021 Eo$
Turbulent dispersion	Burns <i>et al.</i> (2004)	Favre averaging the drag force
Virtual mass	Auton <i>et al.</i> (1988)	Constant coefficient $C_{VM} = 0.5$

210

211 3.4 Bubble induced turbulence

212 Two turbulence sources affect the gas-liquid two-phase flow. The first one is the shear-induced
 213 turbulence that calculates the turbulence parameters by the applied single-phase flow turbulence model.
 214 Therefore, the SST turbulence model was applied to the continuous phase in this study. Dispersed phase
 215 turbulence was obtained from continuous phase calculations. This approximation is valid for flows with
 216 a low-density ratio, such as air-water flows (Colombo *et al.* (2015)).

217 The second one is the BIT, which accounts for the turbulence generation due to bubble-liquid
 218 interaction. Ma *et al.* (2017) proposed a BIT model with the source terms

$$S_K = C_I \mathbf{F}_D (\mathbf{u}_G - \mathbf{u}_L), \quad (11)$$

$$S_\varepsilon = \frac{C_\varepsilon}{\tau} S_K, \quad (12)$$

219 and

$$S_\omega = \frac{1}{C_\mu k} S_\varepsilon - \frac{\omega}{k} S_K. \quad (13)$$

220 Here, k is the turbulent kinetic energy, ω is the turbulent frequency, C_μ is the shear-induced turbulence
 221 coefficient that is taken as 0.09, τ is the BIT time scale

$$\tau = \frac{d_B}{|\mathbf{u}_G - \mathbf{u}_L|} \quad (14)$$

222 and C_I and C_ε are the model coefficients defined as

$$C_I = \min(0.18Re_B^{0.23}, 1) \quad (15)$$

223 and

$$C_\varepsilon = 0.3C_D. \quad (16)$$

224 These BIT source terms are added in the SST turbulent equations and the turbulent viscosity is calculated
225 with the aid of standard equation

$$\mu_L^{Turb} = C_\mu \rho_L \frac{k_L^2}{\varepsilon_L}. \quad (17)$$

226

227 **3.5 Bubble breakup and coalescence**

228 As can be seen from the literature review, less attention has been paid to bubble breakup and coalescence
229 mechanisms in the Eulerian modelling of bubbly flow. However, for the bubbly flow systems, there are
230 strong interactions between bubbles from different classes, which results in bubble breakup and
231 coalescence. The MUSIG model (Lo (1996)), which is based on population balance approach was
232 applied to the simulations. In the MUSIG model, the dispersed phase is divided into M size fractions
233 and the population balance equation is used to determine the mass conservation of the size fractions
234 considering the interaction mass transfer due to bubble breakup and coalescence. The size fraction
235 equations are given as

$$\frac{\partial \rho_G \alpha f_i}{\partial t} + \frac{\partial}{\partial x_i} (\rho_G \alpha f_i \mathbf{u}_{i,G}) = B_{Ci} - D_{Ci} + B_{Bi} - D_{Bi}. \quad (18)$$

236 The source and sink terms contain the birth rates due to coalescence and breakup, B_{Ci} , B_{Bi} , and death
237 rates due to coalescence and breakup of the bubbles, D_{Ci} , D_{Bi} . They are calculated as

$$B_{Ci} = (\rho_G \alpha)^2 \left(\frac{1}{2} \sum_{j \leq i} \sum_{k \leq i} Q(m_j, m_k) X_{jki} \frac{m_j + m_k}{m_j m_k} f_j f_k \right) \quad (19)$$

$$B_{Bi} = \rho_G \alpha \sum_{j > i} g(m_j, m_i) f_j \quad (20)$$

$$D_{Ci} = (\rho_G \alpha)^2 \left(\sum_j Q(m_i, m_j) \frac{1}{m_j} f_i f_j \right) \quad (21)$$

$$D_{Bi} = \rho_G \alpha f_i \sum_{j < i} g(m_i, m_j) \quad (22)$$

where the functions Q denotes the coalescence rate and g denotes the breakup rate. In this context, the coalescence and breakup model of Liao *et al.* (2015) was applied to determine these rates, which considers various bubble interaction mechanisms such as turbulent fluctuation, shear, buoyancy and wake. In the simulations, the change of bubble size due to pressure changes was considered in the calculation of the Sauter mean diameter (d_{32}) by

$$d_{32}^* = d_{32}(\rho_{ref}/\rho_g)^{1/3} \quad (23)$$

where ρ_{ref} is the reference gas density at the inlet and ρ_g is the gas density at a certain height.

Recently, Liao (2020) found that the formulations from Eq. (19) to Eq. (22) preserve only the mass of bubbles but not their number when assigning the breakup/coalescence source term to size groups. A consequence is underprediction of the bubble size, especially in breakup-dominant cases. She developed an internally consistent discretization scheme for the terms of birth rates, which is:

$$B_{Ci}' = (\rho_G \alpha)^2 \left(\frac{1}{2} \sum_{j \leq i} \sum_{k \leq i} Q(m_j; m_k) X_{jki} \frac{m_i}{m_j m_k} f_j f_k \right) \quad (24)$$

$$B_{Bi}' = \rho_G \alpha \sum_{j > i} \frac{m_i}{m_j} f_j \left(g(m_j; m_i) + \sum_{k < j} g(m_j; m_k) Y_{jki} \right) \quad (25)$$

Note that $m_j + m_k$ in Eq. (19) has now been replaced by m_i yielding Eq. (24). The size fraction equation of Eq. (18) is derived from the population balance equation for the bubble number concentration N_i by multiplying it with m_i , so m_i instead of $m_j + m_k$ should be contained in the coalescence source term. The computation of the breakup source term according to Eq. (25) considers two situations of the daughter bubble positioning. One is that the daughter bubble size coincides with the representative value of a size class, and the other is that the daughter bubble size lies between two representative values. In the former case, the source term can be calculated in a similar way given in Eq. (20) or the first term in the bracket of Eq. (25). In the latter one, a mass matrix Y_{jki} like X_{jki} in the coalescence representing the fraction of mass going to group i is needed for the calculation of the source term. In binary breakage, if the parent bubble and one daughter bubble are fixed at a representative value, the size of the second daughter usually does not coincide with any representative values. Therefore, the formulation in Eq. (25) is general. This scheme preserves both the mass and the number of bubbles. The effect of this discretization scheme was investigated in the present study.

4. Mesh independence studies

The flow domain was discretized using structured meshes. Mesh study was done for test 072 with three different meshes (Figure 3): 103,050 elements (mesh 1, subfigure a), 252,000 elements (mesh 2, subfigure b), and 553,850 elements (mesh 3, subfigure c). The mesh refinement was applied both in axial and lateral directions.

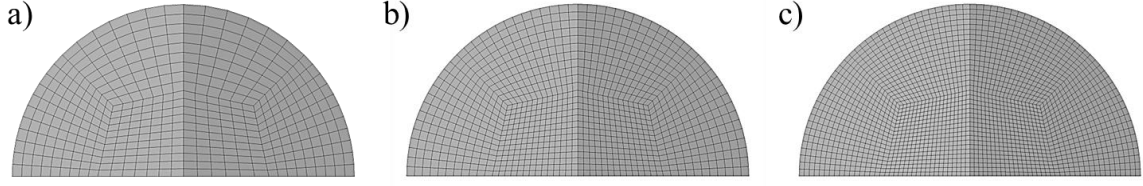


Figure 3: Mesh views: a) mesh 1 b) mesh 2 and c) mesh 3.

Figure 4 shows the simulated average gas fraction along the axial direction for different mesh densities. Upstream of the obstacle $Z < 0$ mm, the mean gas fraction is very much mesh independent. The effect of the mesh refinement is largely noticeable downstream the obstacle $0 \text{ mm} < Z < 200 \text{ mm}$ where high flow complexity occurs. This mesh sensibility to the flow complexity is in line with that previously reported by Tas-Koehler *et al.* (2020). Whereas a maximum relative difference between mesh 1 and mesh 2 is 29%, it is 8% between mesh 2 and mesh 3. Hence, to reduce the computational effort, mesh 2 is applied for this study.

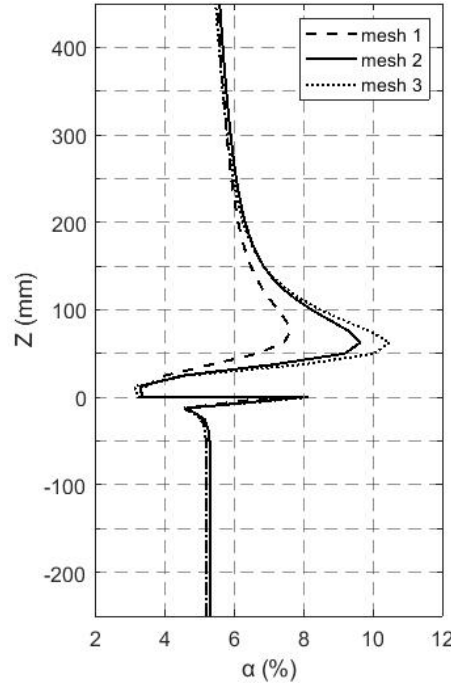


Figure 4: Effect of grid refinement on the average gas fraction for test 072.

5. Results

5.1 Phase distribution

Figure 5 shows the evolution of the averaged gas fraction in the axial direction of the pipe for test cases 072 and 074. Upstream of the obstacle, both cases agree well with the experiments. For test 072, void fraction decreases dramatically downstream the obstacle. After that point, it starts to increase up to around $Z = 60 \text{ mm}$ and it decreases again. Although the peaks that occur after the obstacle in the experiment and simulation do not coincide, generally there is a good agreement between experiment and simulation. For test section 074, void fraction increases downstream the obstacle up to $Z = 40 \text{ mm}$ and it starts to decrease after that point. However, the averaged void fraction is highly overestimated downstream of the obstacle.

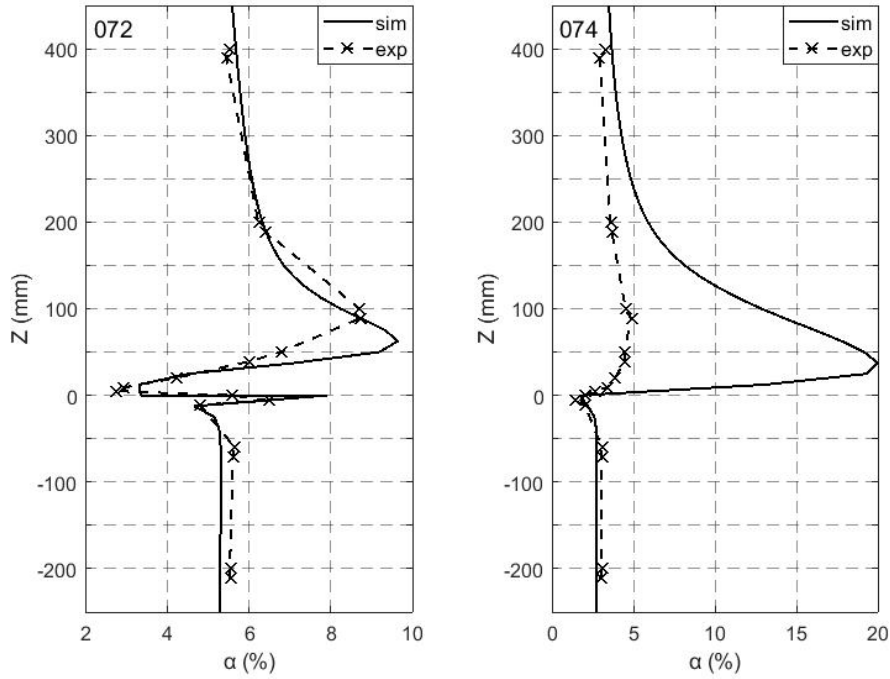


Figure 5: Cross-sectional averaged void fraction along the axial direction for test cases 072 and 074.

Figure 6 shows the void fraction for test 072 and 074. The strong gas accumulation after the obstacle for both tests is calculated. For test 072, a very small near-wall maximum void fraction region underneath the obstacle and the region with void accumulation after the obstacle are well captured by the simulation. However, in line with Figure 5 for test 074, there is a high void region after the obstacle that shows a large discrepancy in terms of its magnitude compared to the experiment. Another finding is that whereas void starts to accumulate just behind the obstacle for test 074, it begins to accumulate after a certain Z position that is around 25 mm for test 072.

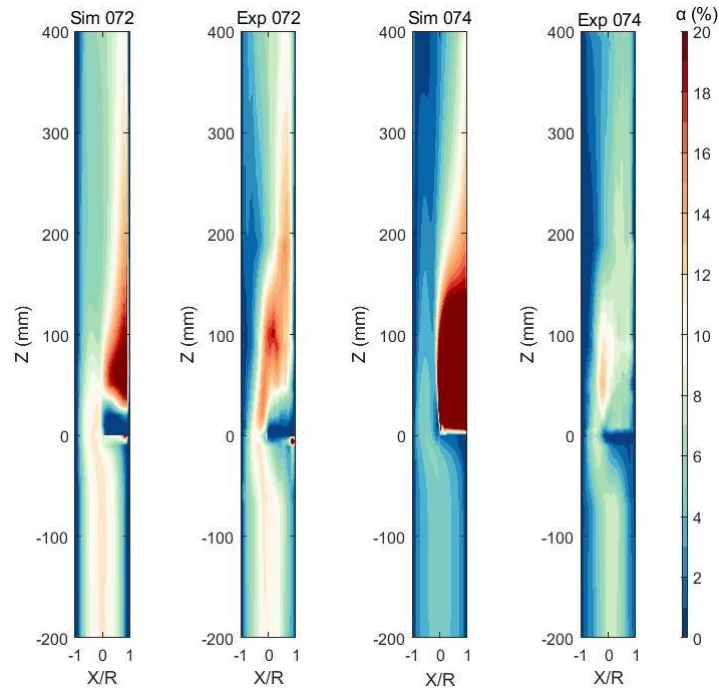


Figure 6: Visualization plots of simulated and measured void fraction for test cases 072 and 074.

In order to explain the different void fraction peaks of test cases 072 and 074, streamlines of the gas velocity of are shown in Figure 7 for $-200 \text{ mm} < Z < 200 \text{ mm}$. While there is a region free of bubbles

directly behind the obstacle for test case 072, this region nearly vanishes for test case 074. Here, the obstacle causes a downstream wake region (vortex region) due to lateral pressure differences (Figure 8). As the liquid superficial velocity increases, the pressure differences increase and so does the wake region. The vortex flow in the wake region leads to void fraction accumulation due to the density difference between the liquid and gas phases. For test case 072, the wake region appears between around $30 \text{ mm} < Z < 80 \text{ mm}$, while for test case 074 it develops between around $10 \text{ mm} < Z < 150 \text{ mm}$. This is in good accordance with the averaged void fraction peaks and changes that are shown in Figure 5 and Figure 6.

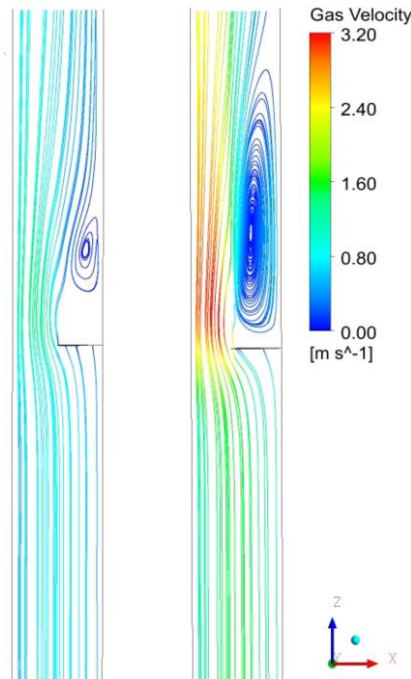


Figure 7: Streamline for test 072 (left) and 074 (right).

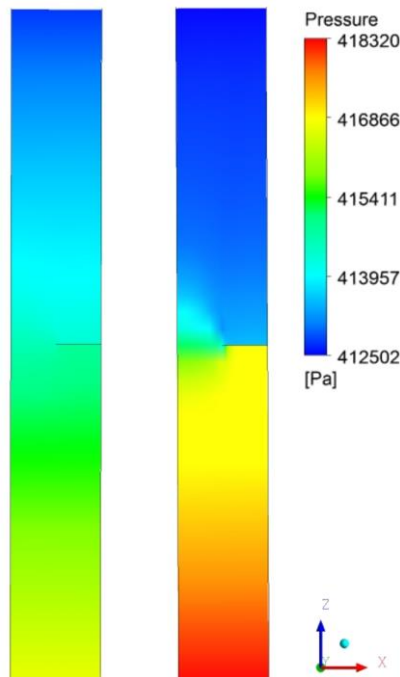


Figure 8: Pressure distribution for test 072 (left) and 074 (right).

Radial void fraction distributions at different cross sections are given in Figure 9 and Figure 10 for both test cases 072 and 074, respectively. At $Z = -200$ mm, the results of test case 072 are in good agreement with the experiments, but in the case of 074, the void fraction is underestimated in the pipe center. At $Z = -11$ mm, better agreement for the obstructed (right) side of the pipe is obtained for test case 074 than for 072. This is in contrast to the results of the unobstructed (left) side of the pipe. At $Z = 20$ mm both test cases provide better results for the unobstructed side of the pipe. Further downstream, the inconsistencies between the experiments and simulations for both sides of the pipe significantly increase for $Z = 100$ mm and both test cases, but decrease again at higher Z positions, respectively. However, discrepancies for test case 074 are significantly higher than for test case 072. Downstream of the obstacle, test case 074 is generally overestimated, especially at the obstructed side of the pipe.

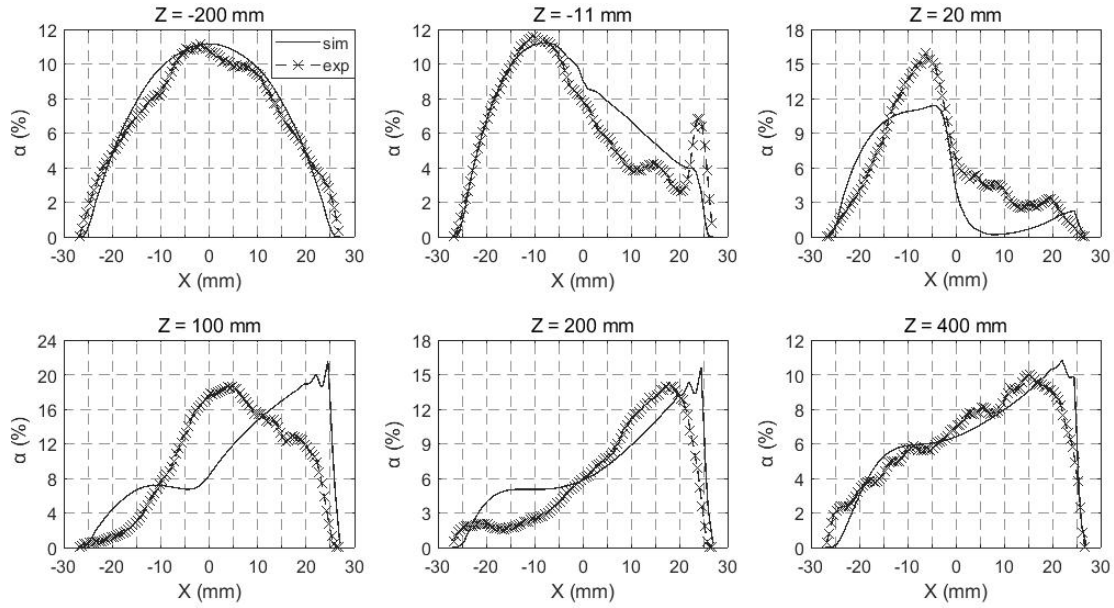


Figure 9: Radial gas fraction distribution for test 072 for different Z positions.

Another point is that without any disturbance, bubbles accumulate in the center of the pipe. Consequently, they change their position near the obstacle to the unobstructed side of the pipe until they reach the wake region. Here, they are drawn into the recirculating flow area. Thus, the bubbles start to accumulate on the obstructed side of the pipe.

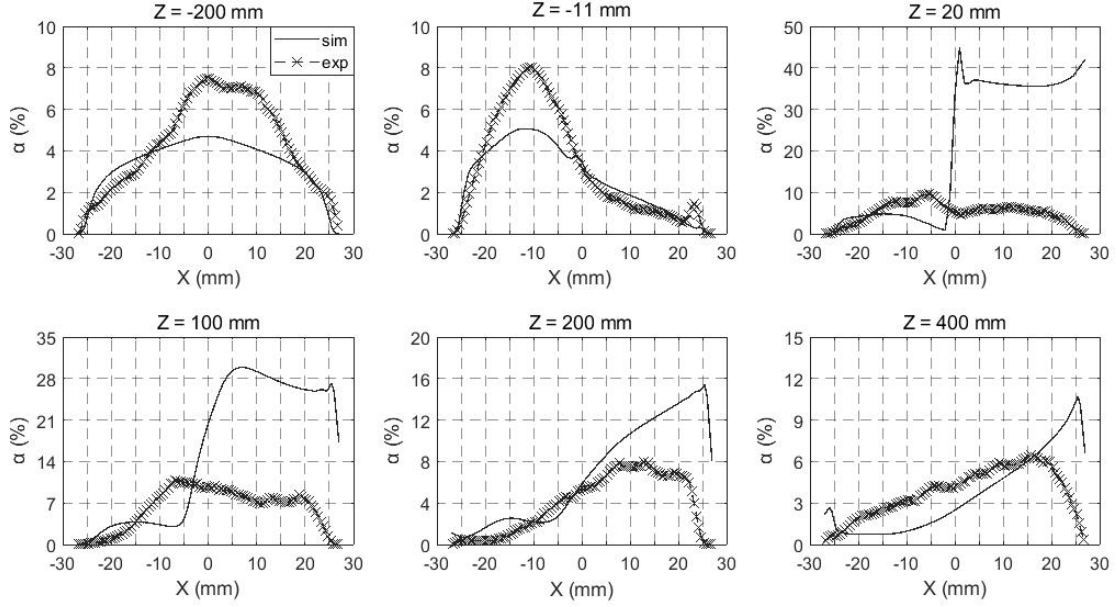


Figure 10: Radial gas fraction distribution for test 074 for different Z positions.

5.2 Bubble dynamics

In Figure 11 the average bubble diameter changes along the axial direction for both test cases are presented, showing a slight overestimation of the bubble size upstream of the flow obstacle for test case 072. However, here, simulation results for test case 074 are in better accordance with experimental results. Although simulation results are in satisfying agreement with experimental data for both tests at the obstacle, peaks that are obtained from the experiments could not be captured by the simulations. Also, according to the experiments, the average bubble diameter peaks downstream the obstacle at around $Z = 200$ mm for both test cases. None of the simulations can capture these peaks. In addition, the average bubble size is underestimated for $Z > 30$ mm for test case 074. For test case 072, though average bubble size is underestimated for $70 \text{ mm} < Z < 350$, it gives good agreement between around $350 \text{ mm} < Z < 400$ mm.

Liao (2020) investigated the inconsistencies of the population balance equation in MUSIG, and updated the model by discretizing the source and sink terms that result from bubble coalescence and breakup with an internally consistent scheme, which preserves both the mass and the number of bubbles. The comparison with the updated model is also shown in Figure 11. Whereas the updated MUSIG model provides similar results to the standard MUSIG model upstream the obstacle, it predicts differently at the downstream. For the test case 072, simulation results with the updated model are overestimated compared to experimental results, but the breakup and coalescence tendency behind the obstacle is well captured. For the test case 074, it provides better average bubble diameter prediction than the standard one.

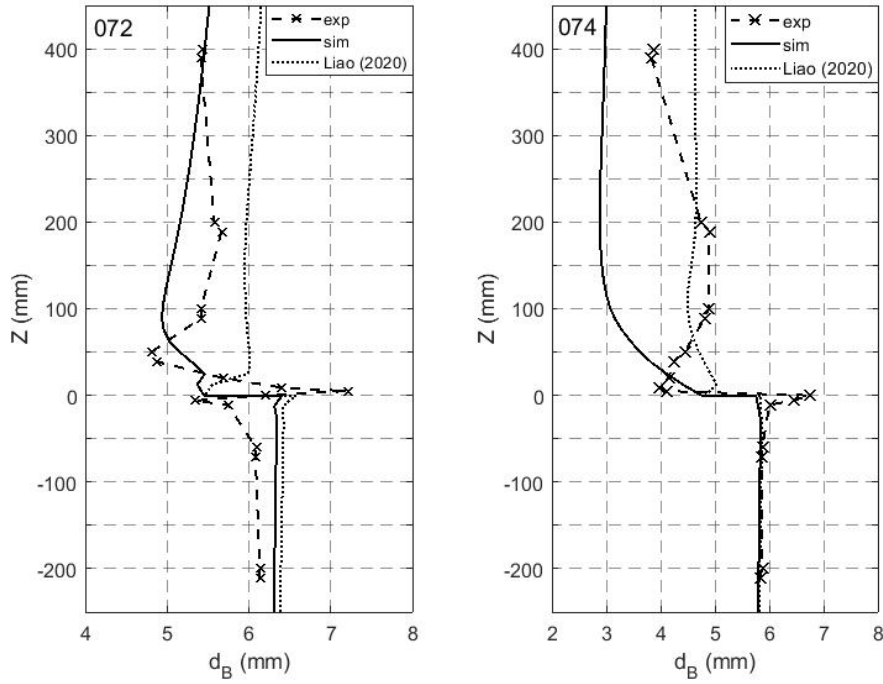


Figure 11: Average bubble diameter for test cases 072 and 074.

Figure 12 presents the average bubble diameter and turbulent dissipation visualization for $-200 \text{ mm} < Z < 200 \text{ mm}$ and both test cases. Upstream of the obstacle, the average bubble diameter near the pipe wall is larger than in the pipe center for test case 072, while it is vice versa for test case 074. This can be explained by the bubble breakup that is dominant for test case 074 due to higher turbulence as compared to test case 072, where more coalescence events take place in the near wall region. Due to the obstacle, a strong liquid jet with high velocity is established, creating a strong shear flow. This, in turn, leads to higher turbulent dissipation as can be seen from the comparison of both test cases in Figure 12. Thus, higher bubble breakup rates are induced. Downstream of the obstacle larger bubble sizes are found on the unobstructed side of the pipe, whereas smaller bubbles occur on the obstructed side because of bubble breakup and liquid circulation for both test cases. This effect increases for test case 074 due to the higher turbulent dissipation. Thus, bubble breakup is more dominant than bubble coalescence in the downstream wake region of the flow obstacle. The accumulation of small bubbles in the circulation region is more obvious (see Figure 7).

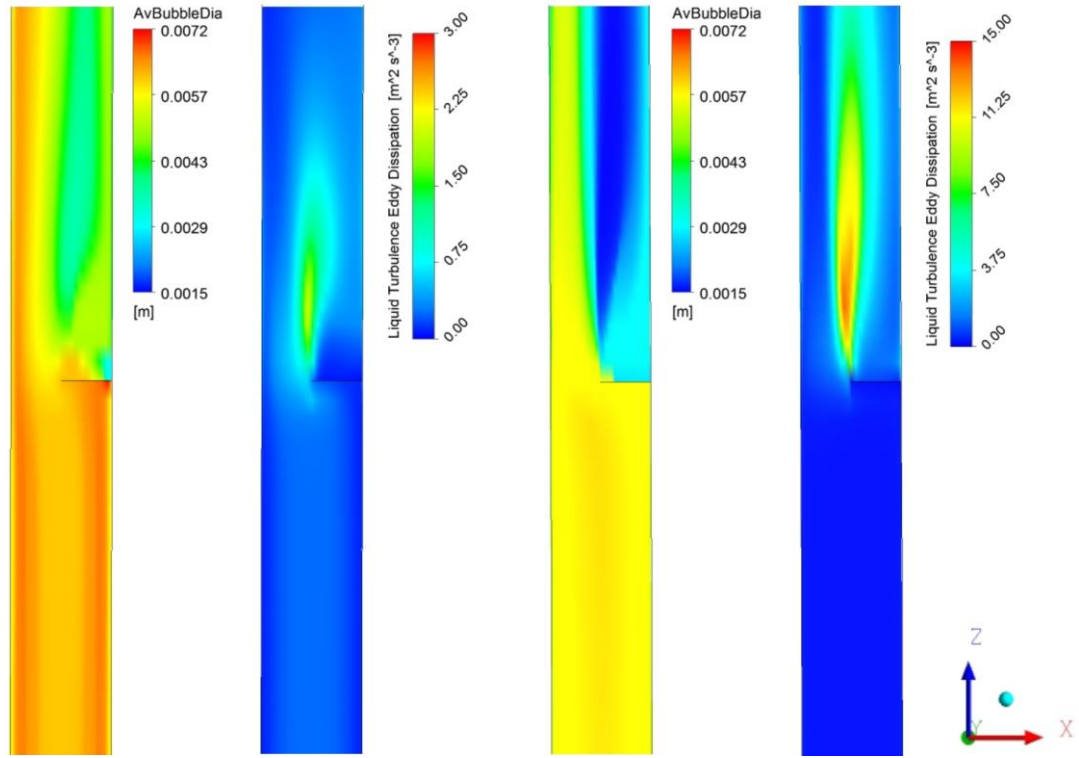


Figure 12: Comparison of average bubble diameter and turbulent dissipation for test cases 072 (left) and 074 (right).

Figure 13 presents the lift and turbulent dispersion force vectors for $-200 \text{ mm} < Z < 200 \text{ mm}$ and both test cases. For test 072, by the lift force, all the bubbles are directed to the pipe center upstream the obstacle due to a negative lift force coefficient. Unlike the lift force, the turbulent dispersion force directs the bubbles to the pipe walls, where the volume fraction is lower, and the magnitude of the turbulent dispersion force is bigger than the magnitude of the lift force near the pipe walls. As a result, as the lift force directs the bubbles to the pipe center and increases further the void fraction there. At the obstacle downstream, bubbles that are in the jet region directed to the pipe center by the lift force. On the other hand, bubbles that are in the wake region behind the obstacle are directed by the lift force to the pipe wall, because of a smaller average diameter. Besides this, the turbulent dispersion force directs the bubbles, which are in the jet region, to the pipe wall as expected to counterwork the accumulation of bubbles. Yet, on the obstacle side, the turbulent dispersion force directs the bubbles to the pipe center. The reason is that turbulent dispersion force influences from high void fraction to low void fraction since it is related to the void fraction gradient.

For test 074, whereas some bubbles, which are close to the wall, are directed to the pipe wall by the lift force upstream the obstacle, the others move to the pipe center. The turbulent dispersion forces direct all the bubbles to the pipe walls due to a core-peak volume fraction profile as shown in Figure 10. Bubbles which have higher lift force magnitude than dispersion force, move to the pipe center. At the obstacle downstream, for the bubbles that are located undisturbed part of the pipe, the lift force directs them further to pipe wall except for the area that is between the jet region and the region behind the obstacle, where negative velocity gradients prevail. Additionally, whereas turbulent dispersion force directs the bubbles, which are on the left-hand side of the pipe and right-hand side just after the obstacle, to the wall, it changes its direction from pipe wall to pipe center after a certain Z distance on the right-hand side of the pipe, because of high accumulation of bubbles there.

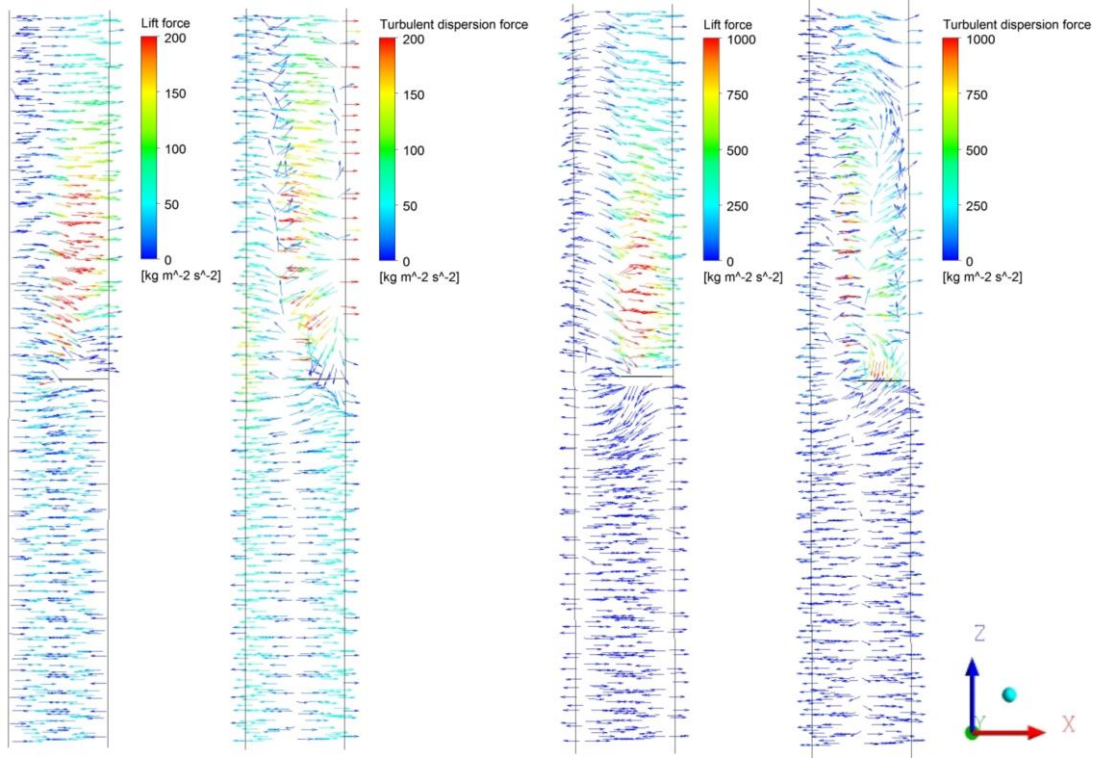


Figure 13: Bubble lift and turbulent dispersion vectors for test 072 (left) and 074 (right).

The average axial gas velocity is shown in Figure 14. It is clear that the flow experiences strong accelerations due to the obstacle. Both simulation results are generally in good agreement with the experiments. However, there are some inconsistencies according to the experiments like that the simulations could not predict the velocity peaks where are $Z = 100 \text{ mm}$ for both tests.

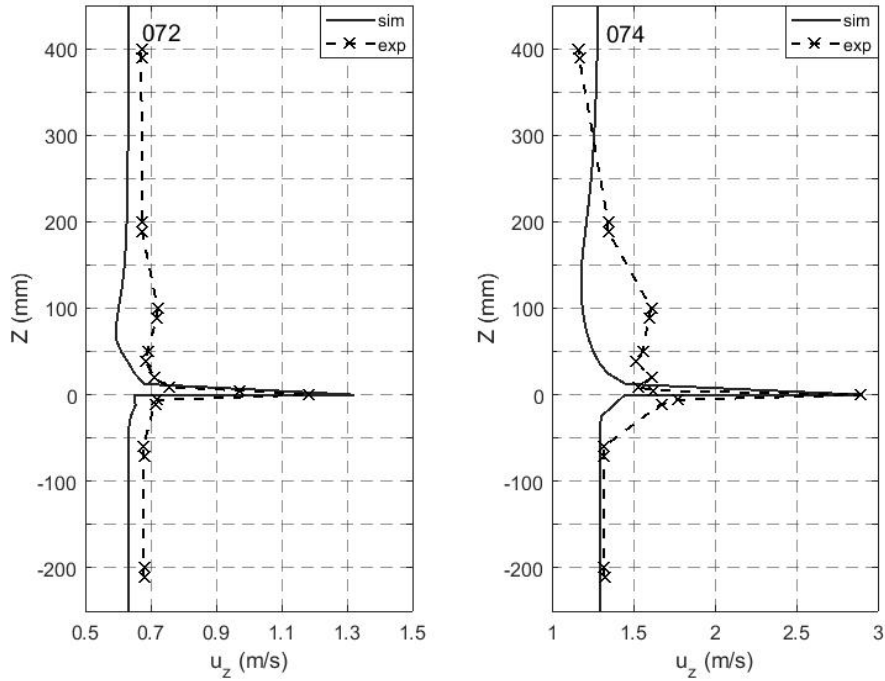


Figure 14: Cross-sectional averaged gas velocity for test 072 and 074.

5.3 Bubble breakup and coalescence

According to Liao *et al.* (2015), there are four mechanisms leading to bubble breakup: laminar shear, turbulent shear, interfacial slip and turbulence fluctuation and likewise five mechanisms leading to coalescence: buoyancy, eddy capture, velocity gradient, wake entrainment and turbulence fluctuation.

The laminar and turbulent shear mechanisms account for viscous shear force in the bulk flow and eddies, respectively. The interfacial slip mechanism considers the impact of interfacial friction. The turbulence fluctuation mechanism describes the effect of turbulent velocity fluctuation on bubble breakup. For coalescence modeling, the buoyancy mechanism accounts for the collision if a faster bubble approaches a slower one. The eddy capture mechanism occurs between bubbles, which are smaller than the Kolmogorov length scale. The velocity gradient mechanism is due to the velocity gradient in the bulk flow. The wake entrainment mechanism acts in the wake region of a bubble where relatively small bubbles can accelerate and catch up with the big one that forms the wake.

The effects of these breakup and coalescence mechanisms were investigated in this study. Thereby, we neglected the turbulent shear mechanism for breakup modelling and the eddy capture mechanism for coalescence modelling as these mechanisms are only important when bubbles are much smaller than the Kolmogorov length scale.

5.3.1 Bubble coalescence mechanisms

Bubble coalescence occurs due to bubble-bubble collision and can be described by different mechanisms as mentioned in Section 5.3. Detailed information can be found in Liao *et al.* (2015). Figure 15 shows the impact of turbulence, velocity gradient, wake entrainment and buoyancy mechanisms on the bubble size distribution at different cross-sections for test case 072. The mechanisms are switched on or off by setting C_{turb} , C_{shear} , C_{wake} and C_{buoy} respectively equal to one or zero. As can be seen from the Figure 15, considering each mechanism separately provide similar results for all Z positions. Here, calculated coalescence rate of all mechanisms might be negligible in comparison to breakup rates, leading to approximately the same predictions. Consequently, the combination of different coalescence mechanisms does not improve the simulation results, as can be seen in Figure 16.

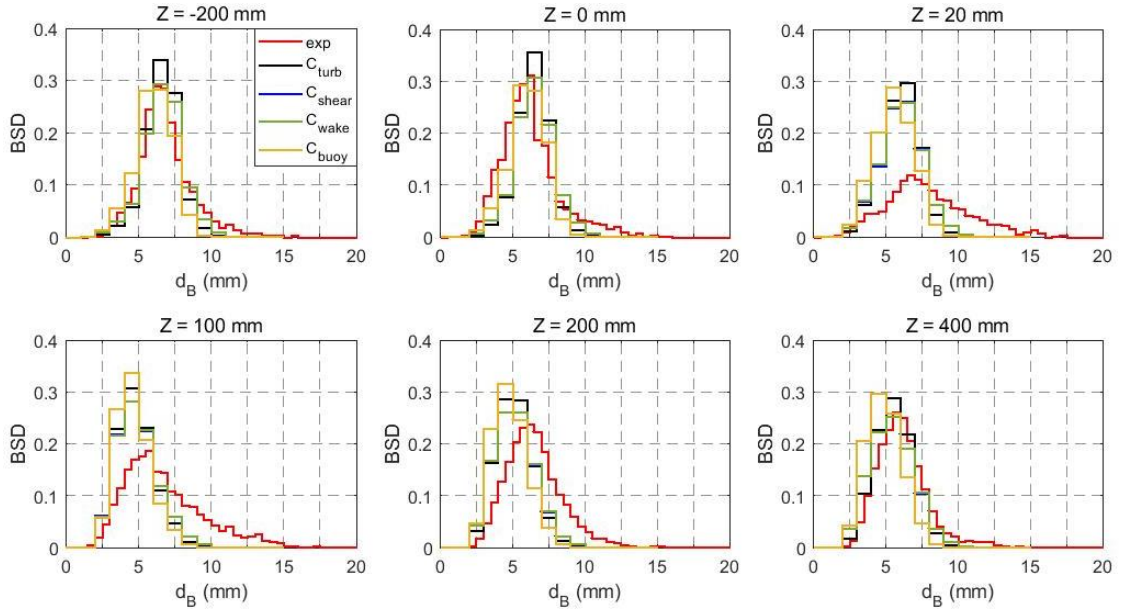


Figure 15: Comparison of bubble coalescence mechanisms for test case 072: C_{turb} , C_{shear} , C_{wake} and C_{buoy} (a legend is given in the first graph).

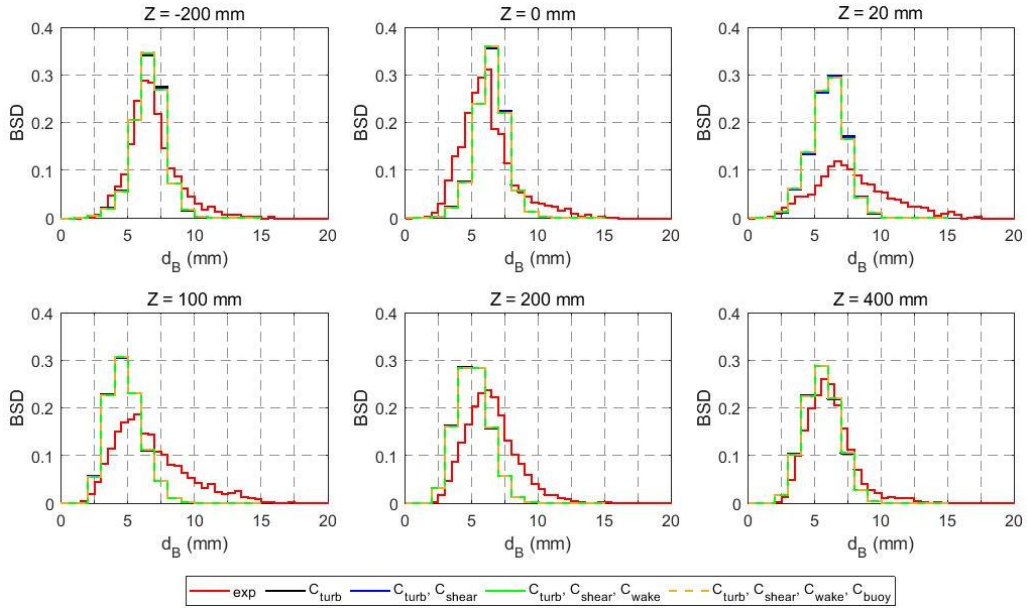


Figure 16: Comparison of bubble coalescence mechanisms for test case 072: C_{turb} , $C_{turb} + C_{shear}$, $C_{turb} + C_{shear} + C_{wake}$ and $C_{turb} + C_{shear} + C_{wake} + C_{buoy}$ (a legend is given below the graphs).

5.3.2 Bubble breakup mechanisms

Bubble breakup takes place due to flow stresses that act on the bubble surface. As mentioned in Section 5.3, there are different mechanisms causing bubble breakup. Figure 17 presents the impacts of turbulent fluctuation (B_{turb}), laminar shear (B_{shear}) and interfacial slip (B_{slip}) on the bubble size distributions for the varied Z positions. B_{shear} and B_{slip} give almost similar results for every Z positions. Also, as can be seen from Figure 18, laminar shear and interfacial slip play a negligible effect in the breakup, since it is mainly caused by turbulence.

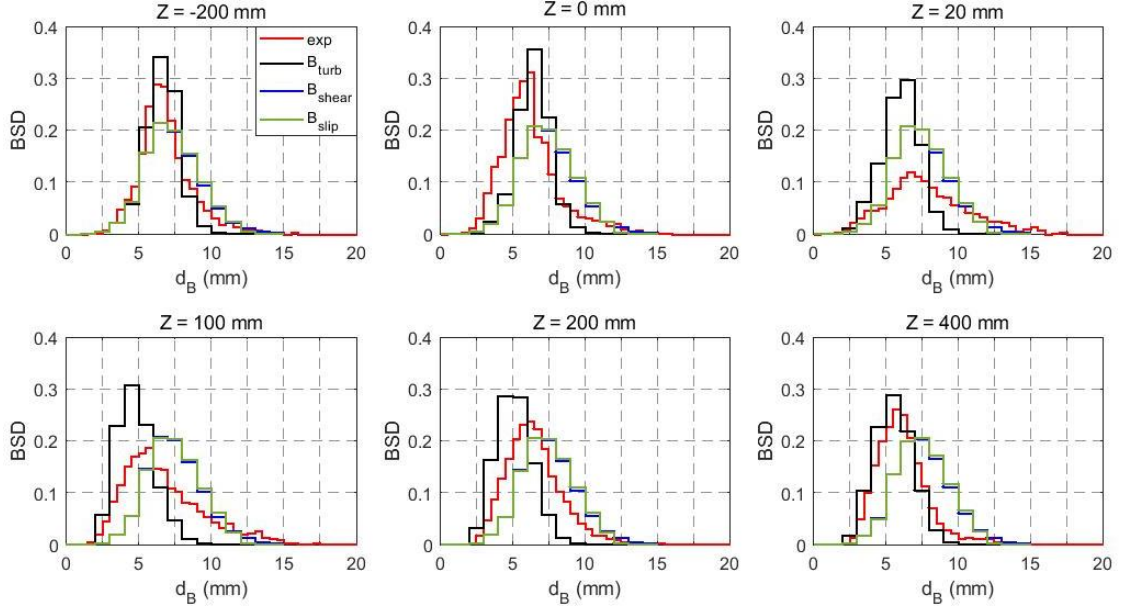


Figure 17: Comparison of bubble breakup mechanisms for test 072: B_{turb} , B_{shear} and B_{slip} (a legend is given in the first graph).

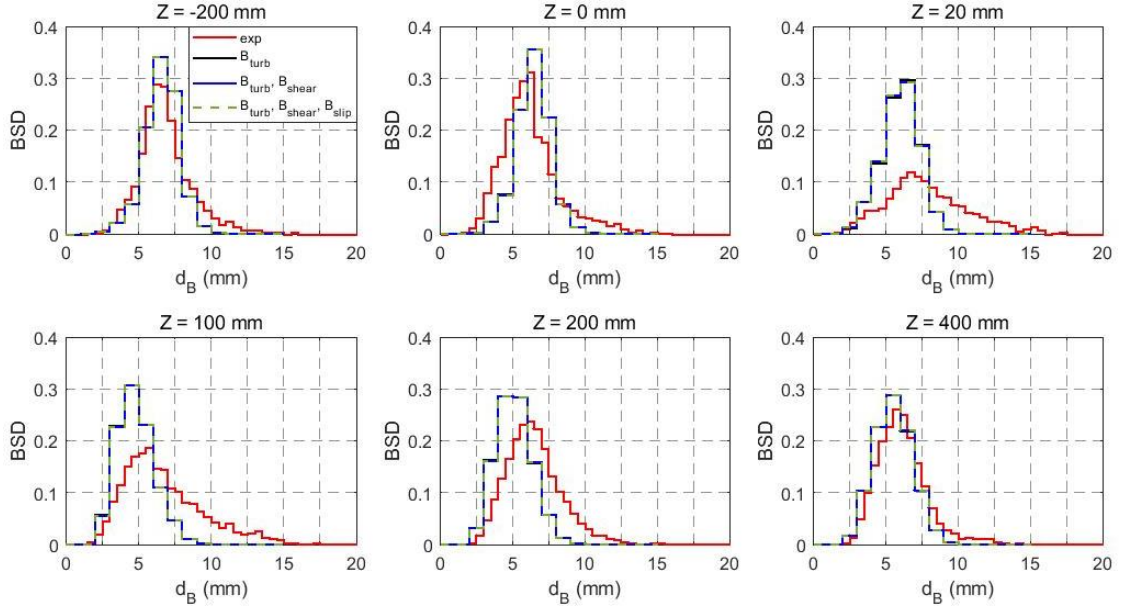


Figure 18: Comparison of bubble breakup mechanisms for test 072: B_{turb} , $B_{turb} + B_{shear}$ and $B_{turb} + B_{shear} + B_{slip}$ (a legend is given in the first graph).

As can be seen from Figure 15 to 18, other mechanisms than turbulence fluctuation have negligible effects. Thus, we considered only the turbulence fluctuation mechanism to model the breakup and coalescence in this study.

Figure 19 and Figure 20 present the bubble size distribution at different Z positions for both test cases. The bubble size distribution (BSD) is determined as gas volume fraction of each bubble size class divided by the class width and total gas void fraction. For the standard MUSIG model, there is a good agreement of simulation and experiment at position $Z = -200$ mm for test case 072. Although the simulation gives satisfying results for the larger bubbles ($d_B > 7.5$ mm) at position $Z = 0$ mm, it is underestimated for smaller ones ($d_B < 6.5$ mm). Here, slight breakup and coalescence tendency as compared to position $Z = -200$ mm is observed in the experiment, but the model captures none of them. At positions $Z = 20$ mm, $Z = 100$ mm and $Z = 200$ mm, the gas fraction of the bubbles in the size class

below 2.5 mm are well predicted. However, the simulation overestimates the gas fraction of bubbles around $2.5 \text{ mm} < d_B < 7.5 \text{ mm}$ for position $Z = 20 \text{ mm}$ and around $2.5 \text{ mm} < d_B < 6.5 \text{ mm}$ for positions $Z = 100 \text{ mm}$ and $Z = 200 \text{ mm}$, but underestimates in the remaining size classes for all three positions. Behind the obstacle, more coalescence events take place leading to a coalescence-dominant trend in the experiments, which is obviously under-predicted by the model. From position $Z = 200 \text{ mm}$ to $Z = 400 \text{ mm}$ bubble breakup is slightly overweighted, while the model predicts almost no change. However, similar to position $Z = -200 \text{ mm}$, good agreement is captured at position $Z = 400 \text{ mm}$ again. The updated MUSIG model predicts a slightly larger coalescence to breakup ratio, which leads to a larger mean bubble size as shown in Figure 11.

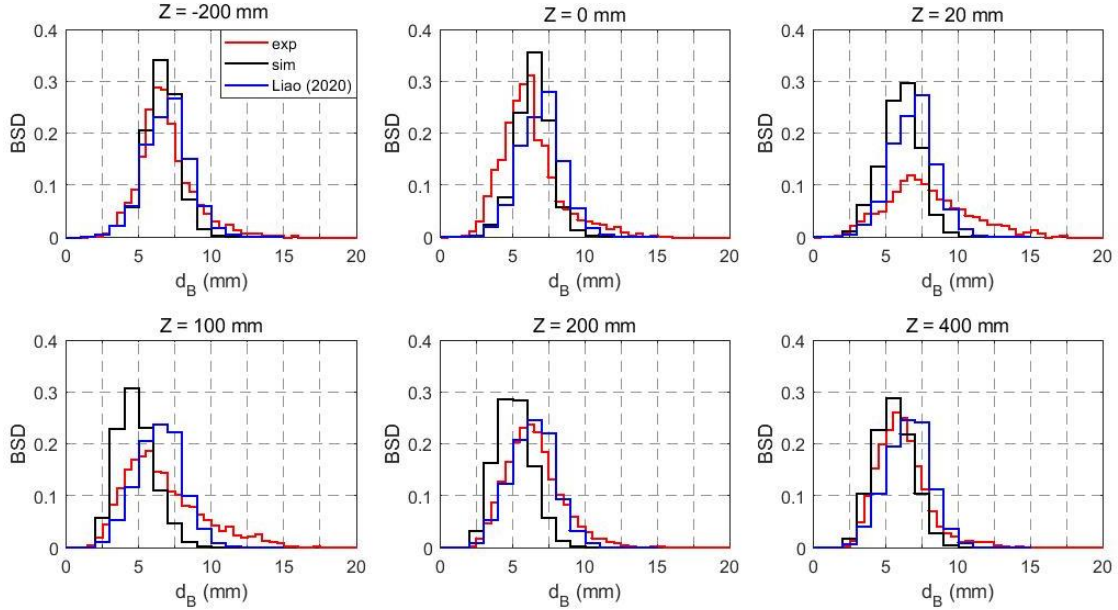


Figure 19: Bubble size distribution at different sections for test case 072 (a legend is given in the first graph).

For the standard MUSIG model, test case 074 shows similar tendencies as compared to test case 072. Good agreement is obtained at position $Z = -200 \text{ mm}$. However, a slight coalescence trend from position $Z = -200 \text{ mm}$ to $Z = 0 \text{ mm}$ is observed in the experiment, while in the simulation coalescence and breakup are almost in balance. In addition, from position $Z = 0 \text{ mm}$ to $Z = 20 \text{ mm}$ breakup seems to be dominant, which may be captured in the simulation, but the breakup rate is highly overestimated. One of the reasons may be the overprediction of the turbulence dissipation rate. Further, slight coalescence is observed again in the experiment from position $Z = 0 \text{ mm}$ to $Z = 20 \text{ mm}$ that cannot be captured by the simulation. Unlike for test case 072, the obvious inconsistency between experiment and simulation continues to exist also at position $Z = 400 \text{ mm}$.

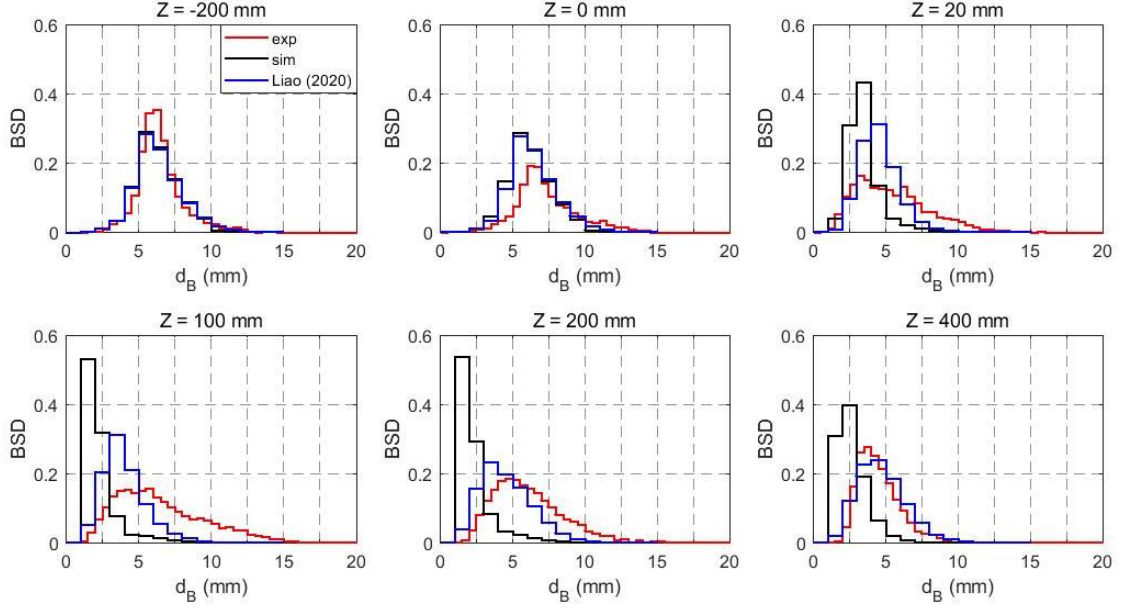


Figure 20: Bubble size distribution at different sections for test case 074 (a legend is given in the first graph).

On the one hand, the updated MUSIG model gives similar results to standard one at the positions $Z = -200$ mm and $Z = 0$ mm, where the coalescence and breakup is nearly in equilibrium. On the other hand, it improves the downstream results significantly, and captures the coalescence trend well. The improvement increases from position $Z = 20$ mm to $Z = 400$ mm. However, there are still notable inconsistencies between experiments and updated MUSIG predictions at the positions $Z = 20$ mm and $Z = 100$ mm where the flow is highly complex.

6. Conclusion

We investigated the performance of state-of-the-art bubble breakup and coalescence modelling for 3D bubbly flow around an obstacle in a pipe. For this purpose, we performed simulations with the homogeneous MUSIG model for two different liquid velocities and compared gas velocity, void fraction, mean bubble diameter and bubble size distribution with 3D UFXCT data. A main feature of the flow is that there is a vortex region behind the obstacle. This vortex region causes a strong gas accumulation downstream the obstacle. While in the high-velocity case void accumulates directly behind the obstacle it does so further downstream in the low-velocity case. The reason is that the obstacle leads to a downstream wake region whose length increases with velocity. Thus, this wake region causes void accumulation depending on the area where it acts.

While the prediction of axial and radial void fractions for the low-velocity case agrees generally well with the experimental results for both the upstream and downstream region of the obstacle, the prediction for the high-velocity case overestimates the average void fraction compared to experimental data downstream of the obstacle. Moreover, downstream of the obstacle the average bubble diameter and average gas velocity are underestimated while they are in good agreement for both the low-velocity and high-velocity cases upstream of the obstacle.

Considering the BSD, we found that coalescence is the dominant mechanism behind the obstacle for the low-velocity case in the experiments. However, the simulations could not capture it. In addition, for the high-velocity case the breakup rate is highly overestimated compared to the experimental data. The difference between experimental data and numerical results may be because of the overestimation of turbulence, which is related to the shear-induced and bubble-induced turbulence models. Simulation

results show that the predicted coalescence rate of all mechanisms might be negligible in comparison to breakup rates since all the coalescence mechanisms provide approximately the same predictions. In addition, it is clear that turbulence is the dominant mechanism for both breakup and coalescence.

The performance of the updated MUSIG model recently developed by Liao (2020) was also tested in the present study. The results show that the updated MUSIG model predicts an obviously lower breakup rate. Consequently, it is able to reproduce the coalescence-dominant trend for the low-velocity test, and predicts a reasonable mean bubble size for the high-velocity test, where turbulence-induced breakup is significant. Investigation on the effect of two-phase turbulence models and improving the coalescence and breakup model in the updated MUSIG model will be topics of future work.

As already mentioned, the low-velocity case shows good agreement with the experimental data downstream of the obstacle, whereas this is not the case for the high-velocity case. The explanation of void fraction overestimation for the high-velocity case may be due to more than one reason. Firstly, applied bubble force models, which are widely used in the literature, do not consider the turbulence effects. Turbulence effects are thought to have an impact, especially on drag force. Secondly, the bubble breakup and coalescence model may need to be improved. Thirdly, the applicability of bubble-induced turbulence that was used for the simulations is still not clear for high shear-induced turbulence cases, since it has been obtained under low turbulence conditions.

References

- Auton, T. R., Hunt, J. C. R., & Prudhomme, M. (1988). The Force Exerted on a Body in Inviscid Unsteady Non-Uniform Rotational Flow. *Journal of Fluid Mechanics*, 197, 241-257. doi:10.1017/S0022112088003246
- Besagni, G., Guedon, G. R., & Inzoli, F. (2018). Computational fluid-dynamic modeling of the mono-dispersed homogeneous flow regime in bubble columns. *Nuclear Engineering and Design*, 331, 222-237. doi:10.1016/j.nucengdes.2018.03.003
- Burns, A. D., Frank, T., Hamill, I., & Shi, J.-M. (2004). *The Favre averaged drag model for turbulent dispersion in Eulerian multi-phase flows*. Paper presented at the 5th International Conference on Multiphase Flow, ICMF, Yokohama, Japan.
- Colombo, M., & Fairweather, M. (2015). Multiphase turbulence in bubbly flows: RANS simulations. *International Journal of Multiphase Flow*, 77, 222-243. doi:10.1016/j.ijmultiphaseflow.2015.09.003
- Colombo, M., & Fairweather, M. (2019). Influence of multiphase turbulence modelling on interfacial momentum transfer in two-fluid Eulerian-Eulerian CFD models of bubbly flows. *Chemical Engineering Science*, 195, 968-984. doi:10.1016/j.ces.2018.10.043
- Frank, T., Zwart, P. J., Krepper, E., Prasser, H. M., & Lucas, D. (2008). Validation of CFD models for mono- and polydisperse air-water two-phase flows in pipes. *Nuclear Engineering and Design*, 238(3), 647-659. doi:10.1016/j.nucengdes.2007.02.056
- Hosokawa, S., Tomiyama, A., Misaki, S., & Hamada, T. (2002). *Lateral migration of single bubbles due to the presence of wall*. Paper presented at the Proceedings of the ASME Joint U.S.-European Fluids Engineering Division Conference, FEDSM2002, Montreal, Canada.
- Ishii, M., & Zuber, N. (1979). Drag Coefficient and Relative Velocity in Bubbly, Droplet or Particulate Flows. *Aiche Journal*, 25(5), 843-855. doi:10.1002/aic.690250513
- Jareteg, K., Strom, H., Sasic, S., & Demaziere, C. (2017). On the dynamics of instabilities in two-fluid models for bubbly flows. *Chemical Engineering Science*, 170, 184-194. doi:10.1016/j.ces.2017.03.063
- Jin, D., Xiong, J. B., & Cheng, X. (2019). Investigation on interphase force modeling for vertical and inclined upward adiabatic bubbly flow. *Nuclear Engineering and Design*, 350, 43-57. doi:10.1016/j.nucengdes.2019.05.005

- Krepper, E., Beyer, M., Frank, T., Lucas, D., & Prasser, H. M. (2009). CFD modelling of polydispersed bubbly two-phase flow around an obstacle. *Nuclear Engineering and Design*, 239(11), 2372-2381. doi:10.1016/j.nucengdes.2009.06.015
- Liao, Y. X. (2020). Update to the MUSIG model in ANSYS CFX for reliable modelling of bubble coalescence and breakup. *Applied Mathematical Modelling*, 81, 506-521. doi:10.1016/j.apm.2020.01.033
- Liao, Y. X., Lucas, D., Krepper, E., & Schmidtke, M. (2011). Development of a generalized coalescence and breakup closure for the inhomogeneous MUSIG model. *Nuclear Engineering and Design*, 241(4), 1024-1033. doi:10.1016/j.nucengdes.2010.04.025
- Liao, Y. X., Ma, T., Liu, L., Ziegenhein, T., Krepper, E., & Lucas, D. (2018). Eulerian modelling of turbulent bubbly flow based on a baseline closure concept. *Nuclear Engineering and Design*, 337, 450-459. doi:10.1016/j.nucengdes.2018.07.021
- Liao, Y. X., Rzehak, R., Lucas, D., & Krepper, E. (2015). Baseline closure model for dispersed bubbly flow: Bubble coalescence and breakup. *Chemical Engineering Science*, 122, 336-349. doi:10.1016/j.ces.2014.09.042
- Lo, S. (1996). *Application of the MUSIG model to bubbly flows*. Paper presented at the AEAT-1096, AEA Technology.
- Luo, H., & Svendsen, H. F. (1996). Theoretical model for drop and bubble breakup in turbulent dispersions. *Aiche Journal*, 42(5), 1225-1233. doi:10.1002/aic.690420505
- Ma, T., Santarelli, C., Ziegenhein, T., Lucas, D., & Frohlich, J. (2017). Direct numerical simulation-based Reynolds-averaged closure for bubble-induced turbulence. *Physical Review Fluids*, 2(3). doi:10.1103/PhysRevFluids.2.034301
- Menter, F. R. (1994). 2-Equation Eddy-Viscosity Turbulence Models for Engineering Applications. *Aiaa Journal*, 32(8), 1598-1605. doi:10.2514/3.12149
- Neumann-Kipping, M., Bieberle, A., & Hampel, U. (2020). Investigations on bubbly two-phase flow in a constricted vertical pipe. *International Journal of Multiphase Flow*, 130. doi:10.1016/j.ijmultiphaseflow.2020.103340
- Parekh, J., & Rzehak, R. (2018). Euler-Euler multiphase CFD-simulation with full Reynolds stress model and anisotropic bubble-induced turbulence. *International Journal of Multiphase Flow*, 99, 231-245. doi:10.1016/j.ijmultiphaseflow.2017.10.012
- Prasser, H. M., Beyer, M., Frank, T., Al Issaa, S., Carl, H., Pietruske, H., & Schutz, P. (2008). Gas-liquid flow around an obstacle in a vertical pipe. *Nuclear Engineering and Design*, 238(7), 1802-1819. doi:10.1016/j.nucengdes.2007.11.007
- Prince, M. J., & Blanch, H. W. (1990). Bubble Coalescence and Break-up in Air-Sparged Bubble-Columns. *Aiche Journal*, 36(10), 1485-1499. doi:10.1002/aic.690361004
- Rzehak, R., & Krepper, E. (2013). CFD modeling of bubble-induced turbulence. *International Journal of Multiphase Flow*, 55, 138-155. doi:10.1016/j.ijmultiphaseflow.2013.04.007
- Rzehak, R., Krepper, E., & Lifante, C. (2012). Comparative study of wall-force models for the simulation of bubbly flows. *Nuclear Engineering and Design*, 253, 41-49. doi:10.1016/j.nucengdes.2012.07.009
- Rzehak, R., Ziegenhein, T., Kriebitzsch, S., Krepper, E., & Lucas, D. (2017). Unified modeling of bubbly flows in pipes, bubble columns, and airlift columns. *Chemical Engineering Science*, 157, 147-158. doi:10.1016/j.ces.2016.04.056
- Simonin, O., & Viollet, P. L. (1990). *Predictions of an oxygen droplet pulverization in a compressible subsonic coflowing hydrogen flow*. Paper presented at the Numerical Methods for Multiphase Flows, FED91.
- Tas-Koehler, S., Lecrivain, G., Krepper, E., Unger, S., & Hampel, U. (2020). Numerical investigation on the effect of transversal fluid field deformation on heat transfer in a rod bundle with mixing vanes. *Nuclear Engineering and Design*, 361. doi:10.1016/j.nucengdes.2020.110575
- Tomiyama, A., Kataoka, I., Zun, I., & Sakaguchi, T. (1998). Drag coefficients of single bubbles under normal and micro gravity conditions. *Jsme International Journal Series B-Fluids and Thermal Engineering*, 41(2), 472-479. doi:10.1299/jsmeb.41.472
- Tomiyama, A., Tamai, H., Zun, I., & Hosokawa, S. (2002). Transverse migration of single bubbles in simple shear flows. *Chemical Engineering Science*, 57(11), 1849-1858. doi:10.1016/S0009-2509(02)00085-4

609 Troshko, A. A., & Hassan, Y. A. (2001). A two-equation turbulence model of turbulent bubbly flows.
610 *International Journal of Multiphase Flow*, 27(11), 1965-2000. doi:10.1016/S0301-
611 9322(01)00043-X
612 Yeoh, G. H., & Tu, J. Y. (2009). *Computational Techniques for Multiphase Flows*: Butterworth-
613 Heinemann.
614

CFD simulation of bubbly flow around an obstacle in a vertical pipe with a focus on breakup and coalescence modelling

Sibel Tas-Koehler ^{a*}, Martin Neumann-Kipping ^b, Yixiang Liao ^a, Eckhard Krepper ^a, Uwe Hampel ^{a,b}

^a Helmholtz-Zentrum Dresden-Rossendorf, Institute of Fluid Dynamics, Bautzner Landstr. 400, 01328 Dresden, Germany

^b Technische Universität Dresden, Chair of Imaging Techniques in Energy and Process Engineering, 01062 Dresden, Germany

* CORRESPONDING AUTHOR (E-MAIL: s.tas@hzdr.de)

ABSTRACT

In the present study, we assessed the capabilities of Eulerian-Eulerian CFD two-phase flow simulation with the homogeneous Multiple Size Group Model (MUSIG) and consideration of breakup and coalescence under three-dimensional flow conditions. We compared void fraction, bubble size and bubble velocity distributions against experimental data from vertical gas-disperse two-phase flow in a pipe with a flow obstruction. The simulation results generally agree well upstream the obstacle, where we have a typically developed pipe flow. Downstream of the obstacle void fraction is overpredicted while bubble velocity is underpredicted. The bubble size distribution has no clear trend. With higher liquid velocities, the deviations increase. As a conclusion, the simulation has difficulties to balance the gas fraction in the strong vortex in the shadow of the obstacle. Here further model improvement is needed.

Keywords: CFD, bubbly flow, model validation, bubble breakup, bubble coalescence

Nomenclature

Latin symbols

d_B	bubble diameter [m]	S_K	source term due to turbulent kinetic energy [N·m ⁻² ·s ⁻¹]
d_{cr}	critical bubble diameter [m]	S_ε	source term due to turbulent dissipation rate [N·m ⁻² ·s ⁻²]
C_D	drag coefficient [-]	S_ω	source term due to turbulent frequency [N·m ⁻⁴]
C_L	lift coefficient [-]	u	velocity [m·s ⁻¹]
C_W	wall lubrication coefficient [-]	Greek symbols	
C_{VM}	virtual mass coefficient [-]	α	gas volume fraction [-]
d_\perp	maximum horizontal bubble dimension [mm]	ρ	density [kg·m ⁻³]
Eo_\perp	Eötvös number depending on d_\perp [-]	τ	bubble-induced time scale [s]
Eo	Eötvös number [-]	τ_{ij}^{Lam}	laminar stress tensor [kg·m ⁻¹ ·s ⁻²]
F_D	drag force per unit volume [N·m ⁻³]	τ_{ij}^{Turb}	turbulent stress tensor [kg·m ⁻¹ ·s ⁻²]
F_L	lift force per unit volume [N·m ⁻³]	ω	turbulence frequency [s ⁻¹]
F_W	wall lubrication force per unit volume [N·m ⁻³]	ν_L^{turb}	kinematic viscosity [m ² ·s ⁻¹]
F_{Disp}	turbulent dispersion force per unit volume [N·m ⁻³]	σ_{TD}	Schmidt number [-]
F_{VM}	virtual mass force per unit volume [N·m ⁻³]	ε	turbulence dissipation rate [m ² ·s ⁻³]
k	phase indicator, turbulent kinetic energy [m ² ·s ⁻²]	Subscripts	
M_i	source term in i-th direction [kg·m ⁻² ·s ⁻²]	B	bubble
p	pressure [Pa]	L	liquid phase
Re	Reynolds number [-]	G	gas phase

26

27 Acronyms

28 BIT: Bubble-Induced Turbulence

29 CFD: Computational Fluid Dynamics

30 FAD: Favre-Averaged Drag

31 MUSIG: Multiple Size Group Model

32 SST: Shear Stress Transport

33 UFXCT: Ultrafast X-ray Computed Tomography

1. Introduction

Bubbly flows are encountered in different industrial applications such as chemical, petroleum and nuclear engineering. In these applications, it is important to know the flow behavior to enhance efficiency such as in chemical reactors or to increase safety margins such as in nuclear reactors. For this purpose, computational fluid dynamics (CFD) that is based on the Eulerian-Eulerian framework has become a popular tool. However, the accuracy of CFD simulations highly relies on correct modeling of phase interactions including interfacial forces (i.e. drag, lift, wall lubrication, turbulent dispersion, and virtual mass), bubble-induced turbulence (BIT) and bubble breakup/coalescence. The modeling of the latter one is possible by a poly-dispersed approach in which the gas phase is divided into a number of size groups. In most of the industrial applications, there is a wide distribution of bubble sizes and a non-uniform radial gas fraction profiles. Thus, the correct prediction of bubble size by breakup and coalescence plays an important role in the accuracy of CFD simulations.

For adiabatic bubbly flow, numerous numerical studies were done, especially focusing on the interfacial forces and BIT. Frank *et al.* (2008) indicated for two-phase pipe flow that a mono-dispersed simulation model, including the Tomiyama lift force, the Frank wall lubrication force, the Favre-averaged drag (FAD) turbulent dispersion force and the Shear Stress Turbulence (SST) model, gives good agreement with the experimental data in terms of gas void fraction. Besagni *et al.* (2018) investigated the effects of the interfacial forces for small-scale and large-scale bubble columns with the mono-dispersed approach. The authors suggested a baseline model with the following interfacial forces: the Tomiyama drag force, the Antal wall lubrication force and the Lopez or Burns turbulence dispersion force. Jin *et al.* (2019) investigated the influence of different models of interfacial forces on the phase distribution for vertical and inclined bubbly flow. They reported that the combination of the Ishii-Zuber drag force, the Saffman-Mei lift force, the Hosokawa wall lubrication force and the FAD turbulent dispersion force provides good radial void fraction results for vertical bubbly flow. Rzehak *et al.* (2012) examined different wall lubrication force models in case of bubbly flow. They compared the Antal, Tomiyama and Hosokawa wall force models and found that the Hosokawa model provides the best performance. Jareteg *et al.* (2017) investigated the effect of a virtual mass force on the stability of the bubbly flow simulations. The authors showed that the implementation of virtual mass force importantly changes the growth rate of void instabilities. Colombo *et al.* (2019) showed the capability of Eulerian-Eulerian CFD for a bubbly flow in a pipe and square duct by focusing on the lift and turbulence forces. According to the results, the effect of turbulence on the phase distribution is as important as the lift force. They further concluded that the wall lubrication force is not necessary if the near-wall region is appropriately resolved.

BIT was also taken into account in many studies. Rzehak *et al.* (2017) developed a closure model for bubbly flow simulations including bubble forces and BIT. However, they did not consider bubble breakup and coalescence yet. The simulation results were compared to experimental data for gas volume fraction, axial liquid velocity and turbulent kinetic energy. Although an overall satisfying agreement between experiments and simulations was found, the authors pointed out that further improvements in turbulence modeling and implementation of bubble breakup/coalescence are highly necessary. Colombo *et al.* (2015) presented the validation of the two-phase Eulerian-Eulerian mono-dispersed model for pipe flow by using experimental data from 6 different literature sources. They reported that their BIT model gives better results in terms of r.m.s velocity fluctuations as compared to Troshko *et al.* (2001) and Rzehak *et al.* (2013). Besagni *et al.* (2018) reported that while BIT inclusion causes convergence problems for large-scale bubble columns, the model of Sato improves the results slightly compared to Simonin *et al.* (1990) for small-scale bubble columns. Parekh *et al.* (2018) compared Launder, Reece, Rodi (LRR) RSM and Speziale-Sarkar-Gatski (SSG) RSM turbulence models as well as the SST model

for air-water pipe flow to capture the anisotropy of turbulent fluctuations concerning BIT. The simulation results showed that predictions of LRR and SSG RSM including BIT are comparable to the SST model over radial profiles of the liquid velocity and gas fraction. However, all three models underestimated the wall peaks of the turbulent kinetic energy and Reynolds stresses by comparing them with the experimental data. Liao *et al.* (2018) applied the MUSIG approach for air-water bubbly flow to test the performance of the BIT model developed by Ma *et al.* (2017). The results showed that the model of Ma *et al.* (2017) predicts the radial gas void fraction and gas velocity well compared to the experiments.

Bubble breakup and coalescence was less considered in the literature compared to interfacial forces and BIT. Frank *et al.* (2008) showed that the inhomogeneous MUSIG (i-MUSIG) model predicts radial void fraction profiles well but further investigation is needed in terms of bubble breakup and coalescence. Liao *et al.* (2015) performed simulations to assess the capability of the bubble breakup and coalescence modeling which was proposed by Liao *et al.* (2011). The results showed that the mean bubble size is overestimated at low superficial liquid velocities and is slightly underestimated at high superficial liquid velocities. The authors concluded that further studies are necessary considering BIT, which has a high impact on bubble breakup and coalescence mechanisms.

While CFD codes have meanwhile been well qualified for simple pipe and column geometries there is yet little analysis and qualification for more complex three-dimensional flow domains. One reason is the lack of appropriate experimental validation data. Prasser *et al.* (2008) provided such data for bubbly flow in a pipe with a semi-circular obstacle using a wire-mesh sensor. Follow-up CFD simulations assuming mono-disperse bubbles provided good void fraction estimation upstream the obstacle but overestimated void fraction downstream. Krepper *et al.* (2009) used the i-MUSIG model including bubble breakup and coalescence and found that the standard breakup and coalescence models (Luo *et al.* (1996), Prince *et al.* (1990)) do not predict the bubble size distribution (BSD) well. Continuing in this line the objectives of this study were to show the capability of bubble breakup and coalescence modelling (Liao *et al.* (2015)) under complex flow conditions with new high-resolution two-phase flow data around an obstacle in a pipe. The 3D flow field was simulated for two different liquid velocity conditions using the MUSIG model. For the simulations, a baseline model for air-water bubbly flow was applied that includes the model of Rzehak *et al.* (2017) for interfacial forces, the model of Liao *et al.* (2015) for the bubble breakup/coalescence and the model of Ma *et al.* (2017) for the BIT. Moreover, the performance of a new discretization scheme for bubble coalescence and breakup modelling developed by Liao (2020) was also tested within this work.

By validation against experimental benchmark data, the capability of bubble breakup/coalescence model is demonstrated in terms of gas volume fraction, gas velocity, mean bubble diameter and bubble size distribution with the aid of Ultrafast X-ray Computed Tomography (UFXCT) measurements (Neumann-Kipping *et al.* (2020)). Furthermore, hydrodynamics of the 3D bubbly flow is analyzed and bubble interaction within the vortex region formed by the obstacle is examined under different liquid velocities. Thus, this paper contributes to two main fields: (i) the assessment of breakup and coalescence model accuracy under 3D flow conditions: (ii) understanding of two-phase flow hydrodynamics in complex geometries.

2. Experimental setup

The experimental study used for validation is described in detail in Neumann-Kipping *et al.* (2020). The experiments were performed in an acrylic pipe with an inner diameter of 54 mm and a total length of 4950 mm. A semi-circular obstacle that blocks half of the inner pipe cross-section was utilized to generate 3D flow fields. A sketch of the test facility, as well as the gas injection module, is illustrated

in Figure 1. The experiments were performed at 4 bar pressure and a liquid temperature of 30°C. Deionized water and compressed air are injected at the bottom of the test section as the liquid and gas phase, respectively.

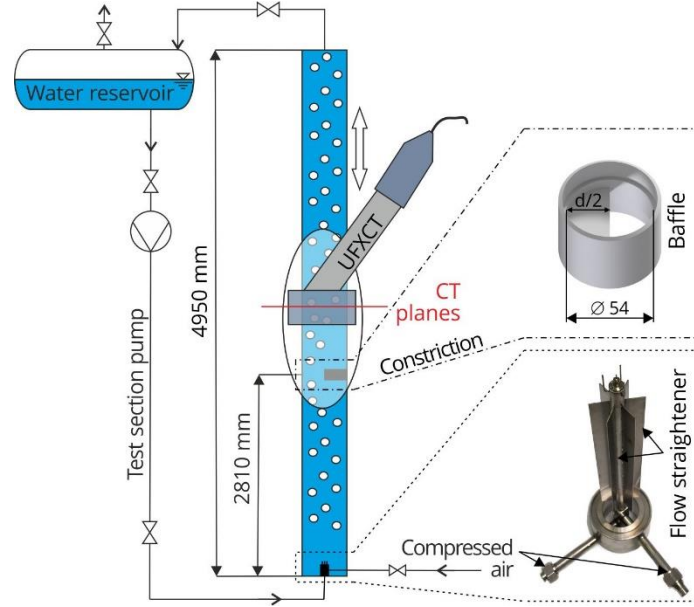


Figure 1: Schematic representations of the vertical test section (left) with details of the gas injection module (bottom right) and the flow obstacle for generation of three-dimensional flow fields (top right).

Various operating conditions in bubbly flow regime were tested by setting appropriate liquid and gas flow rates. Two operating conditions that are used for the present study are described in Table 1.

Table 1: Experimental operating conditions based on combinations of liquid and gas superficial velocities.

Test run	j_l [m·s ⁻¹]	j_g [m·s ⁻¹]
#072	0.4050	0.0368
#074	1.0170	0.0368

Ultrafast X-ray computed tomography (UFXCT), which is a well-established non-invasive imaging technique for multiphase flow, was applied to quantitatively analyze the distribution of gas and liquid within the test section. The UFXCT scanner can be freely moved to allow for imaging of the flow field in several imaging planes up- and downstream of the flow obstacle, as depicted in Table 2 (Neumann-Kipping *et al.* (2020)). By the means of UFXCT, cross-sectional information of the gas velocity and gas volume fraction, as well as bubble size distribution were determined. A detailed discussion of measurement uncertainty UFXCT and quality evaluation of the experimental results can be found in Neumann-Kipping *et al.* (2020). Here, the time-averaged cross-sectional gas holdup and axial gas velocity were used to calculate the inlet superficial gas velocity. This estimated velocity was compared to the set value, showing maximum deviation of $\pm 15\%$ for all cases.

Table 2: Image plane identifier along the vertical test section with relative distances of the upper image plane to the center of the flow constriction.

Identifier	A	B	C	D	E	F	G	H	I
Z (mm)	-200	-60	0	5	20	50	100	200	400

3. Numerical method

3.1 General remarks

For simulation, the geometry was defined as a vertical half tube using a symmetry xz-plane. All simulations were performed using the solver ANSYS CFX 19.2. The fluid domain was modelled from 1.5 m upstream to 1 m downstream the obstacle (Figure 2). The results were obtained by applying the Multiple Size Group Model (Lo (1996)). The dispersed phase was divided into 15 size fractions where the bubble diameters ($d_b = 0 \dots 15 \text{ mm}$) were defined with equidistant bubble diameter. As inlet conditions, a developed flow condition for liquid velocity, liquid turbulent kinetic energy and turbulent dissipation obtained from previous single-phase simulations were assigned. Further, experimentally determined radial void fraction and bubble size distribution at the largest upstream ($Z = -211 \text{ mm}$) position were applied. A constant pressure was defined as outlet condition. All the simulations were performed at steady state condition. Turbulence was modeled only for the liquid phase using the SST model (Menter (1994)). The dimensionless wall distance value for the liquid phase y^+ was kept greater than 30. The single-phase law of wall was used for the wall treatment. The density change of gas was considered by treating the gas phase as ideal gas and its change depending on the height was considered according to

$$\rho_G(P) = \rho_{G,atm} \frac{P_H}{P_{atm}}, \quad (1)$$

where P_{atm} is the atmospheric pressure and $\rho_{G,atm}$ is the gas density depending on atmospheric pressure. P_H is the pressure depending on the height and it is calculated with the following equation:

$$P_H = 4P_{atm} + \rho_L gh. \quad (2)$$

Here, ρ_L is the liquid density, g is the gravitational acceleration and h is the height. On the pipe wall, a no-slip condition was applied for the liquid phase and a free-slip condition for the gas phase. The convergence criteria were set to $RMS < 10^{-6}$.

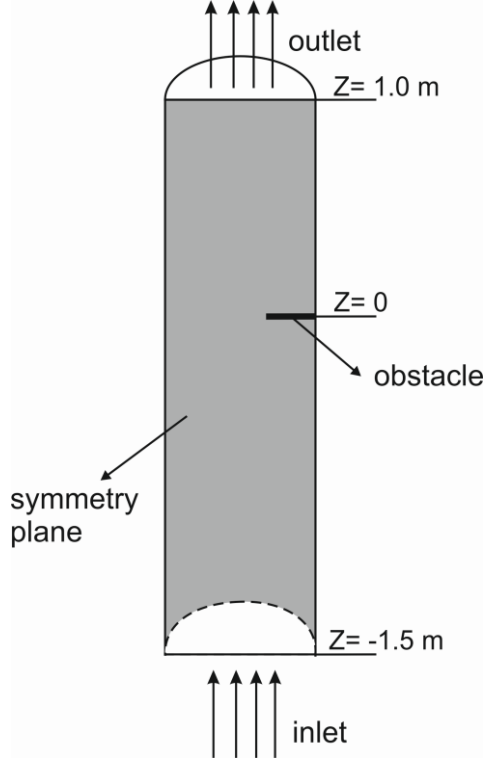


Figure 2: Schematic view of computational domain.

3.2 Governing equations

An Eulerian-Eulerian two-fluid model was applied in the present simulations. This framework defines every phase by a set of averaged conservation equations. Detailed information and derivations of the conservation equations were given by Yeoh *et al.* (2009). Since there is no heat transfer considered for the current study, the conservation equations include only the continuity equation

$$\frac{\partial(\alpha_k \rho_k)}{\partial t} + \frac{\partial}{\partial x_i}(\alpha_k \rho_k \mathbf{u}_{i,k}) = 0 \quad (3)$$

and the momentum equation

$$\begin{aligned} \frac{\partial}{\partial t}(\alpha_k \rho_k \mathbf{u}_{i,k}) + \frac{\partial}{\partial x_i}(\alpha_k \rho_k \mathbf{u}_{i,k} \mathbf{u}_{j,k}) \\ = -\alpha_k \frac{\partial p_k}{\partial x_i} + \frac{\partial}{\partial x_j}[\alpha_k (\tau_{ij,k}^{Lam} + \tau_{ij,k}^{Turb})] + \alpha_k \rho_k \mathbf{g}_i + \mathbf{M}_{i,k}. \end{aligned} \quad (4)$$

Here, k is the phase indicator, α is the volume fraction, ρ is the density, \mathbf{u}_i is the velocity component in the i -th direction, p is the pressure, τ_{ij}^{Lam} is the laminar stress tensor, τ_{ij}^{Turb} is the turbulence stress tensor and \mathbf{M}_i is the source term in the i -th direction, which will be explained in the following section.

3.3 Interfacial momentum transfer

The Eulerian-Eulerian framework considers interpenetrating continua and therefore closure models for interfacial momentum transfer are applied by means of a source term of the form

$$\mathbf{M}_k = \mathbf{F}_D + \mathbf{F}_L + \mathbf{F}_W + \mathbf{F}_{Disp} + \mathbf{F}_{VM} \quad (5)$$

that is added in the momentum equation including drag force \mathbf{F}_D , lift force \mathbf{F}_L , wall lubrication force \mathbf{F}_W , turbulent dispersion force \mathbf{F}_{Disp} and virtual mass force \mathbf{F}_{VM} . In the present study, all these forces were considered for the simulations.

The drag force

$$\mathbf{F}_D = -\frac{3}{4} \frac{C_D}{d_B} \alpha \rho_L |\mathbf{u}_G - \mathbf{u}_L| (\mathbf{u}_G - \mathbf{u}_L) \quad (6)$$

acts opposite to the relative motion of bubbles relative to the surrounding liquid. Here, d_B is the bubble diameter, α is the gas void fraction, ρ_L is the liquid density, \mathbf{u}_G is the gas velocity, \mathbf{u}_L is the liquid velocity and C_D is the drag coefficient calculated by the correlation of Ishii *et al.* (1979).

The lift force

$$\mathbf{F}_L = -C_L \alpha \rho_L (\mathbf{u}_G - \mathbf{u}_L) \times (\nabla \times \mathbf{u}_L) \quad (7)$$

occurs due to the interaction of the bubble with the shear flow of the liquid. Here, C_L is the lift force coefficient and determined by Tomiyama *et al.* (2002). The lift force coefficient changes its sign from positive to negative if the bubble diameter exceeds a critical bubble diameter. For water-air at ambient conditions, as is the case here, this critical diameter has a value of $d_{cr} = 5.8 \text{ mm}$. (Tomiyama *et al.* (1998)).

The wall lubrication force

$$\mathbf{F}_W = \frac{2}{d_B} C_W \rho_L \alpha |\mathbf{u}_G - \mathbf{u}_L|^2 \hat{\mathbf{y}} \quad (8)$$

drives the bubbles away from the wall to avoid the maximum gas fraction at the wall. Here, $\hat{\mathbf{y}}$ is the unit normal perpendicular to the wall and C_W is the wall force coefficient. The model of Hosokawa *et al.* (2002) was applied to predict the wall force coefficient.

The turbulent dispersion force

$$\mathbf{F}_{Disp} = -\frac{3}{4} \frac{C_D}{d_B} \alpha \rho_L |\mathbf{u}_G - \mathbf{u}_L| \frac{\nu_L^{turb}}{\sigma_{TD}} \left(\frac{1}{(1-\alpha)} + \frac{1}{\alpha} \right) \nabla \alpha \quad (9)$$

describes the impact of liquid phase turbulent fluctuations on the gas phase. Here, ν_L^{turb} is the kinematic viscosity of the liquid phase and σ_{TD} is the Schmidt number, generally taken as 0.9. The turbulent dispersion force was modeled by Burns *et al.* (2004).

The virtual mass force

$$\mathbf{F}_{VM} = -C_{VM} \alpha \rho_L \left(\frac{D_G \mathbf{u}_G}{Dt} - \frac{D_L \mathbf{u}_L}{Dt} \right) \quad (10)$$

acts on the bubbles in case of bubble sudden acceleration. Here, C_{VM} is the virtual mass coefficient, which was set to 0.5 for the simulations. Table 3 shows the equations for calculating the force coefficients.

Table 3: Mathematical description for interfacial force coefficients.

Force	Reference	Mathematical description
Drag	Ishii <i>et al.</i> (1979)	$C_D = \max[C_{Dsphere}, \min(C_{Dellipse}, C_{Dcap})]$
		$C_{Dsphere} = \frac{24}{Re_d} (1 + 0.1 Re_d^{3/4}), C_{Dellipse} = \frac{2}{3} \sqrt{Eo}, C_{Dcap} = \frac{8}{3}$
Lift	Tomiyama <i>et al.</i> (2002)	$C_L = \begin{cases} \min[0.288 \tanh(0.121 Re), f(Eo_\perp)] & Eo_\perp < 4 \\ f(Eo_\perp) & 4 < Eo_\perp < 10 \\ -0.27 & 10 < Eo_\perp \end{cases}$
		$f(Eo_\perp) = 0.00105 Eo_\perp^3 - 0.0159 Eo_\perp^2 - 0.0204 Eo_\perp + 0.474$
		$Eo_\perp = \frac{g(\rho_L - \rho_L)d_\perp^2}{\sigma} \quad d_\perp = d_B \sqrt[3]{1 + 0.163 Eo^{0.757}}$
Wall lubrication	Hosokawa <i>et al.</i> (2002)	$C_W(y) = f(Eo) \left(\frac{d_B}{2y}\right)^2, \quad f(Eo) = 0.021 Eo$
Turbulent dispersion	Burns <i>et al.</i> (2004)	Favre averaging the drag force
Virtual mass	Auton <i>et al.</i> (1988)	Constant coefficient $C_{VM} = 0.5$

210

211 3.4 Bubble induced turbulence

212 Two turbulence sources affect the gas-liquid two-phase flow. The first one is the shear-induced
 213 turbulence that calculates the turbulence parameters by the applied single-phase flow turbulence model.
 214 Therefore, the SST turbulence model was applied to the continuous phase in this study. Dispersed phase
 215 turbulence was obtained from continuous phase calculations. This approximation is valid for flows with
 216 a low-density ratio, such as air-water flows (Colombo *et al.* (2015)).

217 The second one is the BIT, which accounts for the turbulence generation due to bubble-liquid
 218 interaction. Ma *et al.* (2017) proposed a BIT model with the source terms

$$S_K = C_I \mathbf{F}_D (\mathbf{u}_G - \mathbf{u}_L), \quad (11)$$

$$S_\varepsilon = \frac{C_\varepsilon}{\tau} S_K, \quad (12)$$

219 and

$$S_\omega = \frac{1}{C_\mu k} S_\varepsilon - \frac{\omega}{k} S_K. \quad (13)$$

220 Here, k is the turbulent kinetic energy, ω is the turbulent frequency, C_μ is the shear-induced turbulence
 221 coefficient that is taken as 0.09, τ is the BIT time scale

$$\tau = \frac{d_B}{|\mathbf{u}_G - \mathbf{u}_L|} \quad (14)$$

222 and C_I and C_ε are the model coefficients defined as

$$C_I = \min(0.18Re_B^{0.23}, 1) \quad (15)$$

223 and

$$C_\varepsilon = 0.3C_D. \quad (16)$$

224 These BIT source terms are added in the SST turbulent equations and the turbulent viscosity is calculated
225 with the aid of standard equation

$$\mu_L^{Turb} = C_\mu \rho_L \frac{k_L^2}{\varepsilon_L}. \quad (17)$$

226

227 **3.5 Bubble breakup and coalescence**

228 As can be seen from the literature review, less attention has been paid to bubble breakup and coalescence
229 mechanisms in the Eulerian modelling of bubbly flow. However, for the bubbly flow systems, there are
230 strong interactions between bubbles from different classes, which results in bubble breakup and
231 coalescence. The MUSIG model (Lo (1996)), which is based on population balance approach was
232 applied to the simulations. In the MUSIG model, the dispersed phase is divided into M size fractions
233 and the population balance equation is used to determine the mass conservation of the size fractions
234 considering the interaction mass transfer due to bubble breakup and coalescence. The size fraction
235 equations are given as

$$\frac{\partial \rho_G \alpha f_i}{\partial t} + \frac{\partial}{\partial x_i} (\rho_G \alpha f_i \mathbf{u}_{i,G}) = B_{Ci} - D_{Ci} + B_{Bi} - D_{Bi}. \quad (18)$$

236 The source and sink terms contain the birth rates due to coalescence and breakup, B_{Ci} , B_{Bi} , and death
237 rates due to coalescence and breakup of the bubbles, D_{Ci} , D_{Bi} . They are calculated as

$$B_{Ci} = (\rho_G \alpha)^2 \left(\frac{1}{2} \sum_{j \leq i} \sum_{k \leq i} Q(m_j, m_k) X_{jki} \frac{m_j + m_k}{m_j m_k} f_j f_k \right) \quad (19)$$

$$B_{Bi} = \rho_G \alpha \sum_{j > i} g(m_j, m_i) f_j \quad (20)$$

$$D_{Ci} = (\rho_G \alpha)^2 \left(\sum_j Q(m_i, m_j) \frac{1}{m_j} f_i f_j \right) \quad (21)$$

$$D_{Bi} = \rho_G \alpha f_i \sum_{j < i} g(m_i, m_j) \quad (22)$$

where the functions Q denotes the coalescence rate and g denotes the breakup rate. In this context, the coalescence and breakup model of Liao *et al.* (2015) was applied to determine these rates, which considers various bubble interaction mechanisms such as turbulent fluctuation, shear, buoyancy and wake. In the simulations, the change of bubble size due to pressure changes was considered in the calculation of the Sauter mean diameter (d_{32}) by

$$d_{32}^* = d_{32}(\rho_{ref}/\rho_g)^{1/3} \quad (23)$$

where ρ_{ref} is the reference gas density at the inlet and ρ_g is the gas density at a certain height.

Recently, Liao (2020) found that the formulations from Eq. (19) to Eq. (22) preserve only the mass of bubbles but not their number when assigning the breakup/coalescence source term to size groups. A consequence is underprediction of the bubble size, especially in breakup-dominant cases. She developed an internally consistent discretization scheme for the terms of birth rates, which is:

$$B_{Ci}' = (\rho_G \alpha)^2 \left(\frac{1}{2} \sum_{j \leq i} \sum_{k \leq i} Q(m_j; m_k) X_{jki} \frac{m_i}{m_j m_k} f_j f_k \right) \quad (24)$$

$$B_{Bi}' = \rho_G \alpha \sum_{j > i} \frac{m_i}{m_j} f_j \left(g(m_j; m_i) + \sum_{k < j} g(m_j; m_k) Y_{jki} \right) \quad (25)$$

Note that $m_j + m_k$ in Eq. (19) has now been replaced by m_i yielding Eq. (24). The size fraction equation of Eq. (18) is derived from the population balance equation for the bubble number concentration N_i by multiplying it with m_i , so m_i instead of $m_j + m_k$ should be contained in the coalescence source term. The computation of the breakup source term according to Eq. (25) considers two situations of the daughter bubble positioning. One is that the daughter bubble size coincides with the representative value of a size class, and the other is that the daughter bubble size lies between two representative values. In the former case, the source term can be calculated in a similar way given in Eq. (20) or the first term in the bracket of Eq. (25). In the latter one, a mass matrix Y_{jki} like X_{jki} in the coalescence representing the fraction of mass going to group i is needed for the calculation of the source term. In binary breakage, if the parent bubble and one daughter bubble are fixed at a representative value, the size of the second daughter usually does not coincide with any representative values. Therefore, the formulation in Eq. (25) is general. This scheme preserves both the mass and the number of bubbles. The effect of this discretization scheme was investigated in the present study.

4. Mesh independence studies

The flow domain was discretized using structured meshes. Mesh study was done for test 072 with three different meshes (Figure 3): 103,050 elements (mesh 1, subfigure a), 252,000 elements (mesh 2, subfigure b), and 553,850 elements (mesh 3, subfigure c). The mesh refinement was applied both in axial and lateral directions.

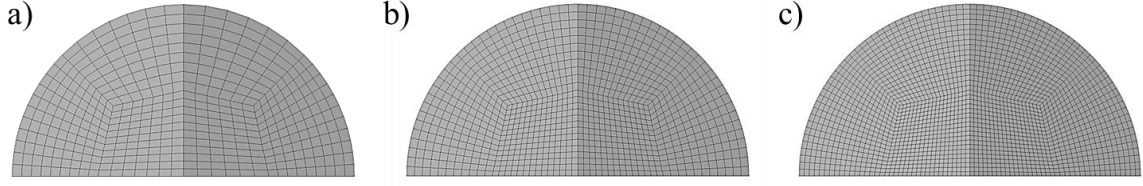


Figure 3: Mesh views: a) mesh 1 b) mesh 2 and c) mesh 3.

Figure 4 shows the simulated average gas fraction along the axial direction for different mesh densities. Upstream of the obstacle $Z < 0$ mm, the mean gas fraction is very much mesh independent. The effect of the mesh refinement is largely noticeable downstream the obstacle $0 \text{ mm} < Z < 200 \text{ mm}$ where high flow complexity occurs. This mesh sensibility to the flow complexity is in line with that previously reported by Tas-Koehler *et al.* (2020). Whereas a maximum relative difference between mesh 1 and mesh 2 is 29%, it is 8% between mesh 2 and mesh 3. Hence, to reduce the computational effort, mesh 2 is applied for this study.

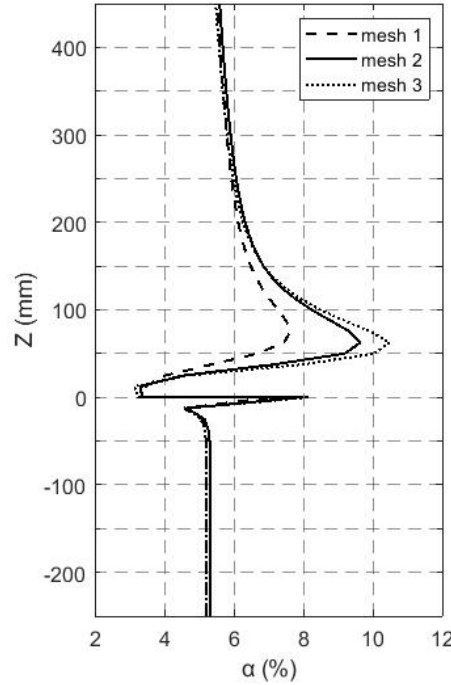


Figure 4: Effect of grid refinement on the average gas fraction for test 072.

5. Results

5.1 Phase distribution

Figure 5 shows the evolution of the averaged gas fraction in the axial direction of the pipe for test cases 072 and 074. Upstream of the obstacle, both cases agree well with the experiments. For test 072, void fraction decreases dramatically downstream the obstacle. After that point, it starts to increase up to around $Z = 60 \text{ mm}$ and it decreases again. Although the peaks that occur after the obstacle in the experiment and simulation do not coincide, generally there is a good agreement between experiment and simulation. For test section 074, void fraction increases downstream the obstacle up to $Z = 40 \text{ mm}$ and it starts to decrease after that point. However, the averaged void fraction is highly overestimated downstream of the obstacle.

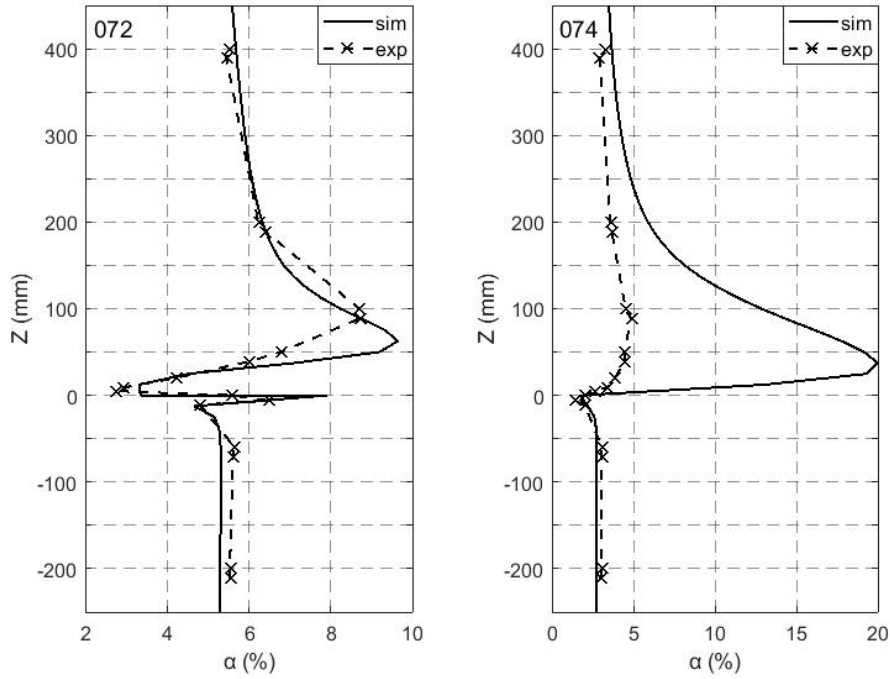


Figure 5: Cross-sectional averaged void fraction along the axial direction for test cases 072 and 074.

Figure 6 shows the void fraction for test 072 and 074. The strong gas accumulation after the obstacle for both tests is calculated. For test 072, a very small near-wall maximum void fraction region underneath the obstacle and the region with void accumulation after the obstacle are well captured by the simulation. However, in line with Figure 5 for test 074, there is a high void region after the obstacle that shows a large discrepancy in terms of its magnitude compared to the experiment. Another finding is that whereas void starts to accumulate just behind the obstacle for test 074, it begins to accumulate after a certain Z position that is around 25 mm for test 072.

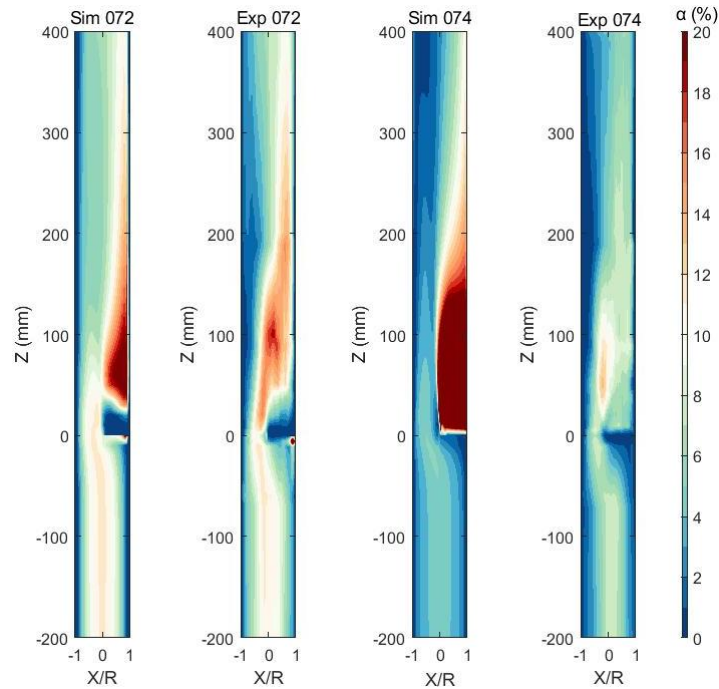


Figure 6: Visualization plots of simulated and measured void fraction for test cases 072 and 074.

In order to explain the different void fraction peaks of test cases 072 and 074, streamlines of the gas velocity of are shown in Figure 7 for $-200 \text{ mm} < Z < 200 \text{ mm}$. While there is a region free of bubbles

directly behind the obstacle for test case 072, this region nearly vanishes for test case 074. Here, the obstacle causes a downstream wake region (vortex region) due to lateral pressure differences (Figure 8). As the liquid superficial velocity increases, the pressure differences increase and so does the wake region. The vortex flow in the wake region leads to void fraction accumulation due to the density difference between the liquid and gas phases. For test case 072, the wake region appears between around $30 \text{ mm} < Z < 80 \text{ mm}$, while for test case 074 it develops between around $10 \text{ mm} < Z < 150 \text{ mm}$. This is in good accordance with the averaged void fraction peaks and changes that are shown in Figure 5 and Figure 6.

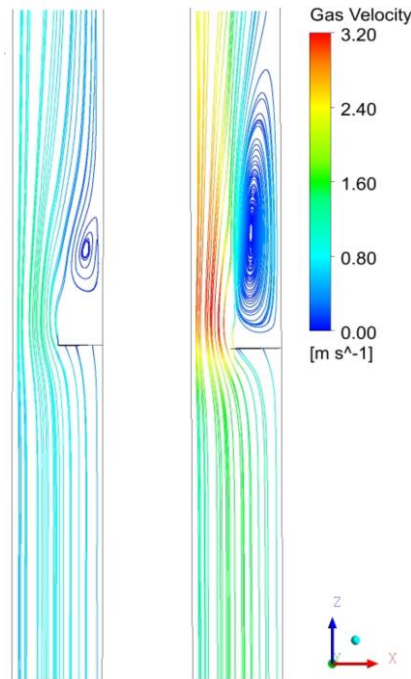


Figure 7: Streamline for test 072 (left) and 074 (right).

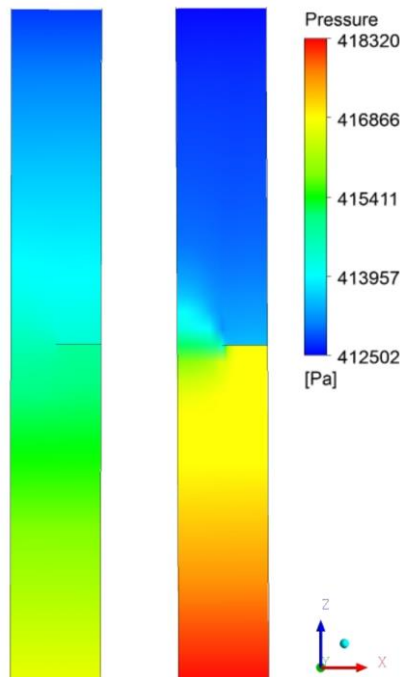


Figure 8: Pressure distribution for test 072 (left) and 074 (right).

Radial void fraction distributions at different cross sections are given in Figure 9 and Figure 10 for both test cases 072 and 074, respectively. At $Z = -200$ mm, the results of test case 072 are in good agreement with the experiments, but in the case of 074, the void fraction is underestimated in the pipe center. At $Z = -11$ mm, better agreement for the obstructed (right) side of the pipe is obtained for test case 074 than for 072. This is in contrast to the results of the unobstructed (left) side of the pipe. At $Z = 20$ mm both test cases provide better results for the unobstructed side of the pipe. Further downstream, the inconsistencies between the experiments and simulations for both sides of the pipe significantly increase for $Z = 100$ mm and both test cases, but decrease again at higher Z positions, respectively. However, discrepancies for test case 074 are significantly higher than for test case 072. Downstream of the obstacle, test case 074 is generally overestimated, especially at the obstructed side of the pipe.

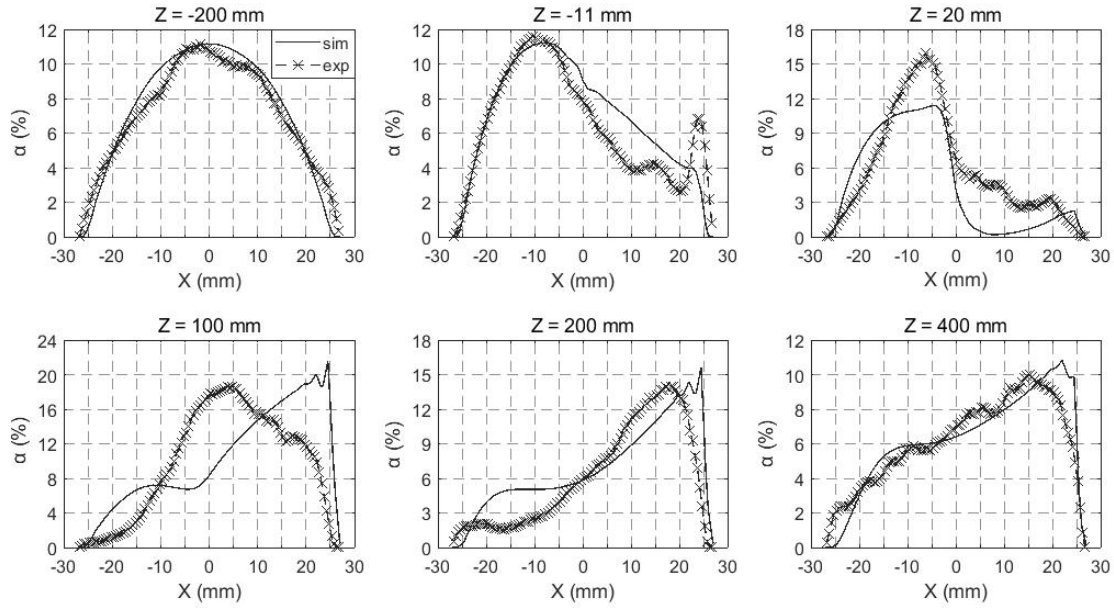


Figure 9: Radial gas fraction distribution for test 072 for different Z positions.

Another point is that without any disturbance, bubbles accumulate in the center of the pipe. Consequently, they change their position near the obstacle to the unobstructed side of the pipe until they reach the wake region. Here, they are drawn into the recirculating flow area. Thus, the bubbles start to accumulate on the obstructed side of the pipe.

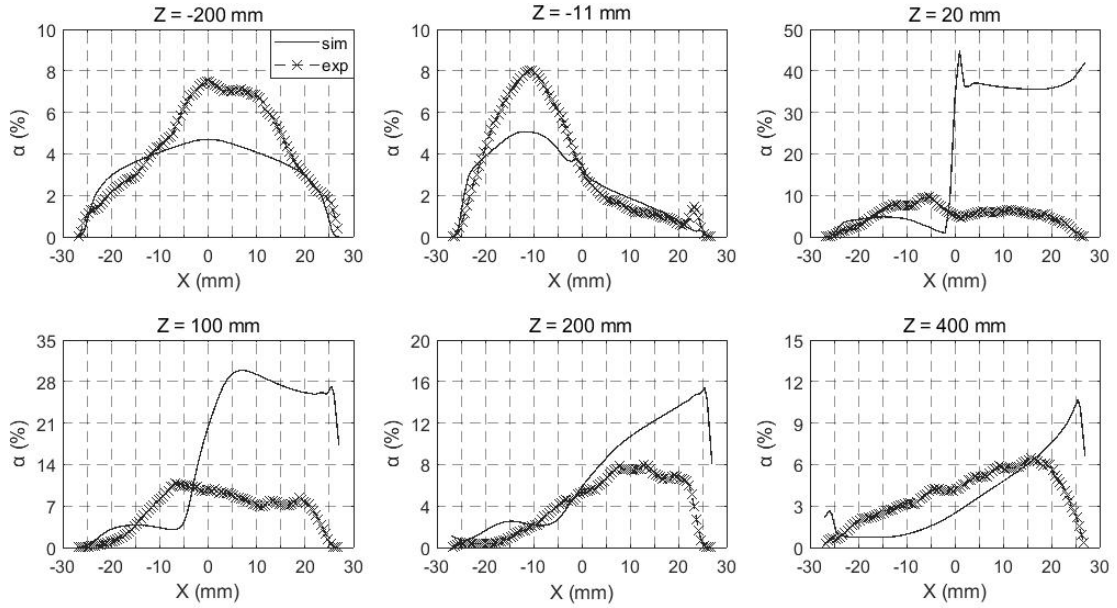


Figure 10: Radial gas fraction distribution for test 074 for different Z positions.

5.2 Bubble dynamics

In Figure 11 the average bubble diameter changes along the axial direction for both test cases are presented, showing a slight overestimation of the bubble size upstream of the flow obstacle for test case 072. However, here, simulation results for test case 074 are in better accordance with experimental results. Although simulation results are in satisfying agreement with experimental data for both tests at the obstacle, peaks that are obtained from the experiments could not be captured by the simulations. Also, according to the experiments, the average bubble diameter peaks downstream the obstacle at around $Z = 200$ mm for both test cases. None of the simulations can capture these peaks. In addition, the average bubble size is underestimated for $Z > 30$ mm for test case 074. For test case 072, though average bubble size is underestimated for $70 \text{ mm} < Z < 350$, it gives good agreement between around $350 \text{ mm} < Z < 400$ mm.

Liao (2020) investigated the inconsistencies of the population balance equation in MUSIG, and updated the model by discretizing the source and sink terms that result from bubble coalescence and breakup with an internally consistent scheme, which preserves both the mass and the number of bubbles. The comparison with the updated model is also shown in Figure 11. Whereas the updated MUSIG model provides similar results to the standard MUSIG model upstream the obstacle, it predicts differently at the downstream. For the test case 072, simulation results with the updated model are overestimated compared to experimental results, but the breakup and coalescence tendency behind the obstacle is well captured. For the test case 074, it provides better average bubble diameter prediction than the standard one.

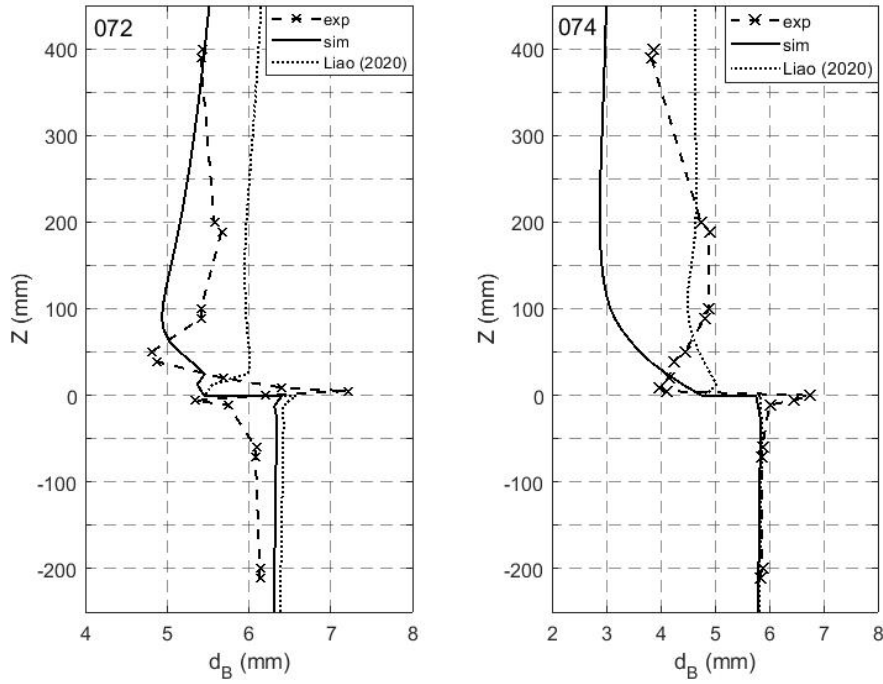


Figure 11: Average bubble diameter for test cases 072 and 074.

Figure 12 presents the average bubble diameter and turbulent dissipation visualization for $-200 \text{ mm} < Z < 200 \text{ mm}$ and both test cases. Upstream of the obstacle, the average bubble diameter near the pipe wall is larger than in the pipe center for test case 072, while it is vice versa for test case 074. This can be explained by the bubble breakup that is dominant for test case 074 due to higher turbulence as compared to test case 072, where more coalescence events take place in the near wall region. Due to the obstacle, a strong liquid jet with high velocity is established, creating a strong shear flow. This, in turn, leads to higher turbulent dissipation as can be seen from the comparison of both test cases in Figure 12. Thus, higher bubble breakup rates are induced. Downstream of the obstacle larger bubble sizes are found on the unobstructed side of the pipe, whereas smaller bubbles occur on the obstructed side because of bubble breakup and liquid circulation for both test cases. This effect increases for test case 074 due to the higher turbulent dissipation. Thus, bubble breakup is more dominant than bubble coalescence in the downstream wake region of the flow obstacle. The accumulation of small bubbles in the circulation region is more obvious (see Figure 7).

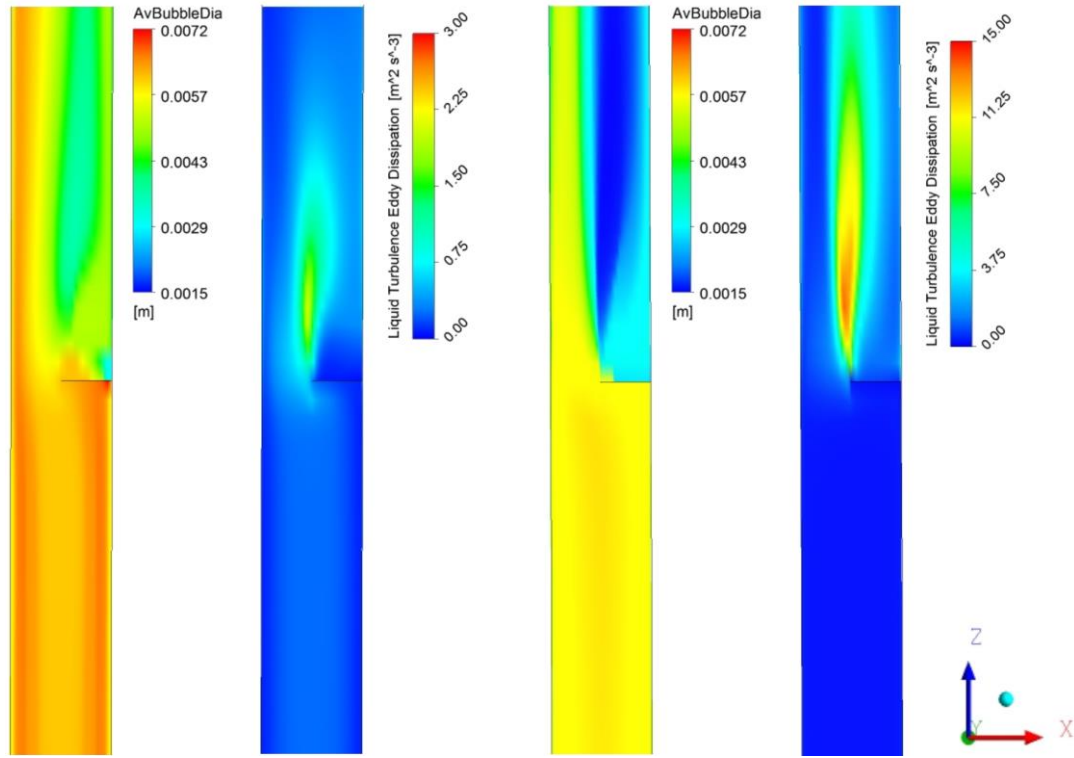


Figure 12: Comparison of average bubble diameter and turbulent dissipation for test cases 072 (left) and 074 (right).

Figure 13 presents the lift and turbulent dispersion force vectors for $-200 \text{ mm} < Z < 200 \text{ mm}$ and both test cases. For test 072, by the lift force, all the bubbles are directed to the pipe center upstream the obstacle due to a negative lift force coefficient. Unlike the lift force, the turbulent dispersion force directs the bubbles to the pipe walls, where the volume fraction is lower, and the magnitude of the turbulent dispersion force is bigger than the magnitude of the lift force near the pipe walls. As a result, as the lift force directs the bubbles to the pipe center and increases further the void fraction there. At the obstacle downstream, bubbles that are in the jet region directed to the pipe center by the lift force. On the other hand, bubbles that are in the wake region behind the obstacle are directed by the lift force to the pipe wall, because of a smaller average diameter. Besides this, the turbulent dispersion force directs the bubbles, which are in the jet region, to the pipe wall as expected to counterwork the accumulation of bubbles. Yet, on the obstacle side, the turbulent dispersion force directs the bubbles to the pipe center. The reason is that turbulent dispersion force influences from high void fraction to low void fraction since it is related to the void fraction gradient.

For test 074, whereas some bubbles, which are close to the wall, are directed to the pipe wall by the lift force upstream the obstacle, the others move to the pipe center. The turbulent dispersion forces direct all the bubbles to the pipe walls due to a core-peak volume fraction profile as shown in Figure 10. Bubbles which have higher lift force magnitude than dispersion force, move to the pipe center. At the obstacle downstream, for the bubbles that are located undisturbed part of the pipe, the lift force directs them further to pipe wall except for the area that is between the jet region and the region behind the obstacle, where negative velocity gradients prevail. Additionally, whereas turbulent dispersion force directs the bubbles, which are on the left-hand side of the pipe and right-hand side just after the obstacle, to the wall, it changes its direction from pipe wall to pipe center after a certain Z distance on the right-hand side of the pipe, because of high accumulation of bubbles there.

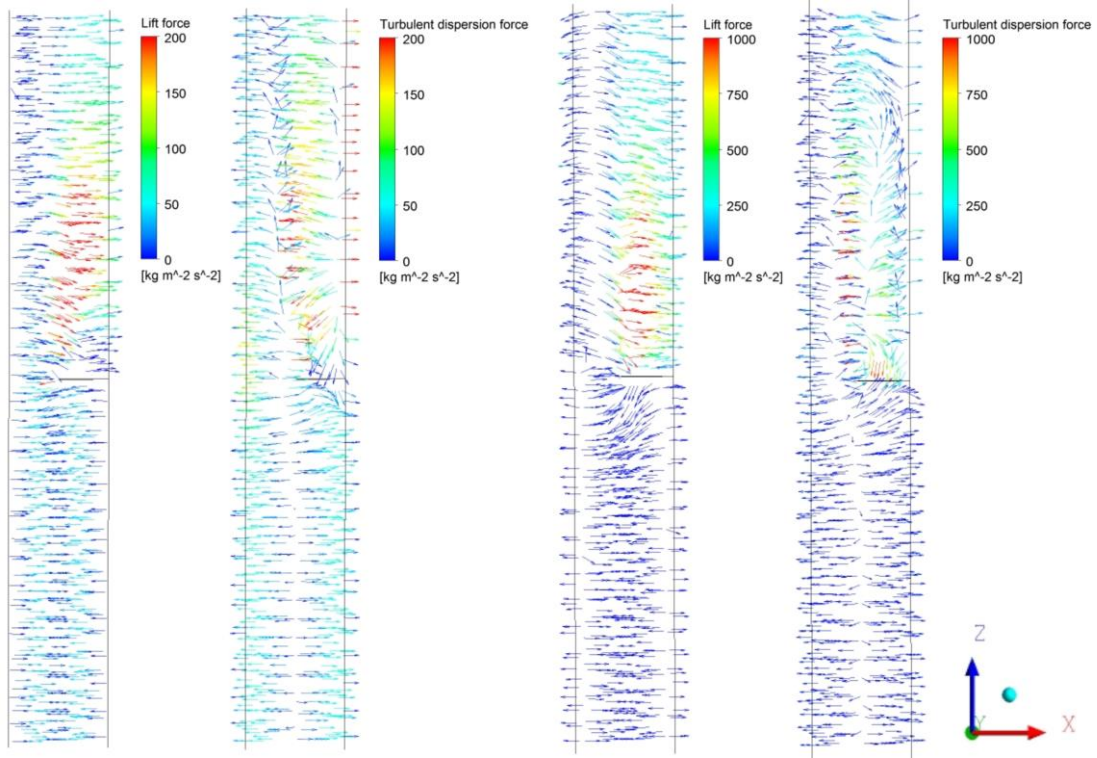


Figure 13: Bubble lift and turbulent dispersion vectors for test 072 (left) and 074 (right).

The average axial gas velocity is shown in Figure 14. It is clear that the flow experiences strong accelerations due to the obstacle. Both simulation results are generally in good agreement with the experiments. However, there are some inconsistencies according to the experiments like that the simulations could not predict the velocity peaks where are $Z = 100 \text{ mm}$ for both tests.

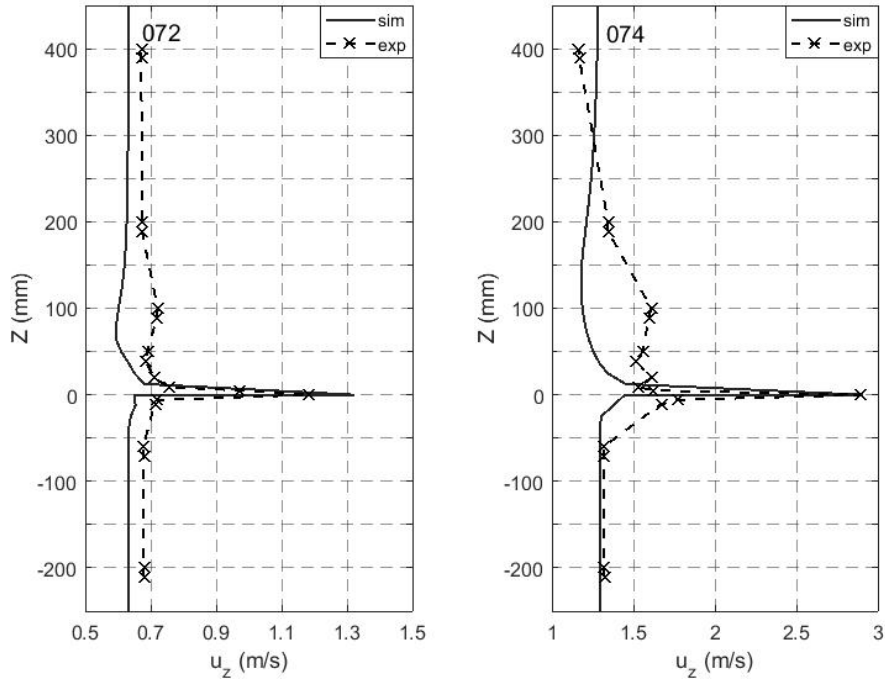


Figure 14: Cross-sectional averaged gas velocity for test 072 and 074.

5.3 Bubble breakup and coalescence

According to Liao *et al.* (2015), there are four mechanisms leading to bubble breakup: laminar shear, turbulent shear, interfacial slip and turbulence fluctuation and likewise five mechanisms leading to coalescence: buoyancy, eddy capture, velocity gradient, wake entrainment and turbulence fluctuation.

The laminar and turbulent shear mechanisms account for viscous shear force in the bulk flow and eddies, respectively. The interfacial slip mechanism considers the impact of interfacial friction. The turbulence fluctuation mechanism describes the effect of turbulent velocity fluctuation on bubble breakup. For coalescence modeling, the buoyancy mechanism accounts for the collision if a faster bubble approaches a slower one. The eddy capture mechanism occurs between bubbles, which are smaller than the Kolmogorov length scale. The velocity gradient mechanism is due to the velocity gradient in the bulk flow. The wake entrainment mechanism acts in the wake region of a bubble where relatively small bubbles can accelerate and catch up with the big one that forms the wake.

The effects of these breakup and coalescence mechanisms were investigated in this study. Thereby, we neglected the turbulent shear mechanism for breakup modelling and the eddy capture mechanism for coalescence modelling as these mechanisms are only important when bubbles are much smaller than the Kolmogorov length scale.

5.3.1 Bubble coalescence mechanisms

Bubble coalescence occurs due to bubble-bubble collision and can be described by different mechanisms as mentioned in Section 5.3. Detailed information can be found in Liao *et al.* (2015). Figure 15 shows the impact of turbulence, velocity gradient, wake entrainment and buoyancy mechanisms on the bubble size distribution at different cross-sections for test case 072. The mechanisms are switched on or off by setting C_{turb} , C_{shear} , C_{wake} and C_{buoy} respectively equal to one or zero. As can be seen from the Figure 15, considering each mechanism separately provide similar results for all Z positions. Here, calculated coalescence rate of all mechanisms might be negligible in comparison to breakup rates, leading to approximately the same predictions. Consequently, the combination of different coalescence mechanisms does not improve the simulation results, as can be seen in Figure 16.

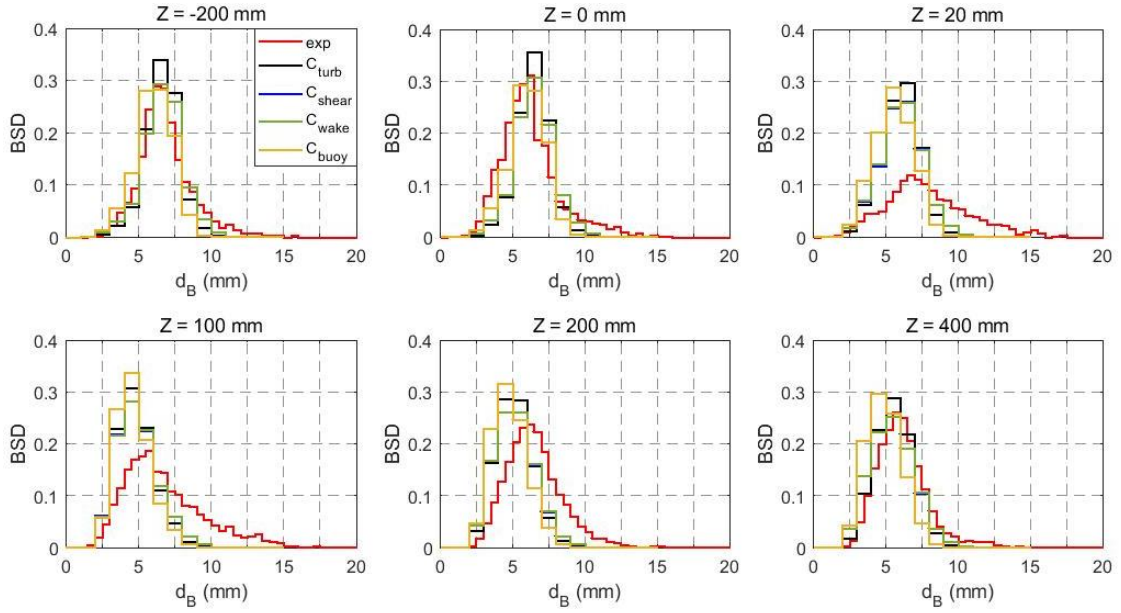


Figure 15: Comparison of bubble coalescence mechanisms for test case 072: C_{turb} , C_{shear} , C_{wake} and C_{buoy} (a legend is given in the first graph).

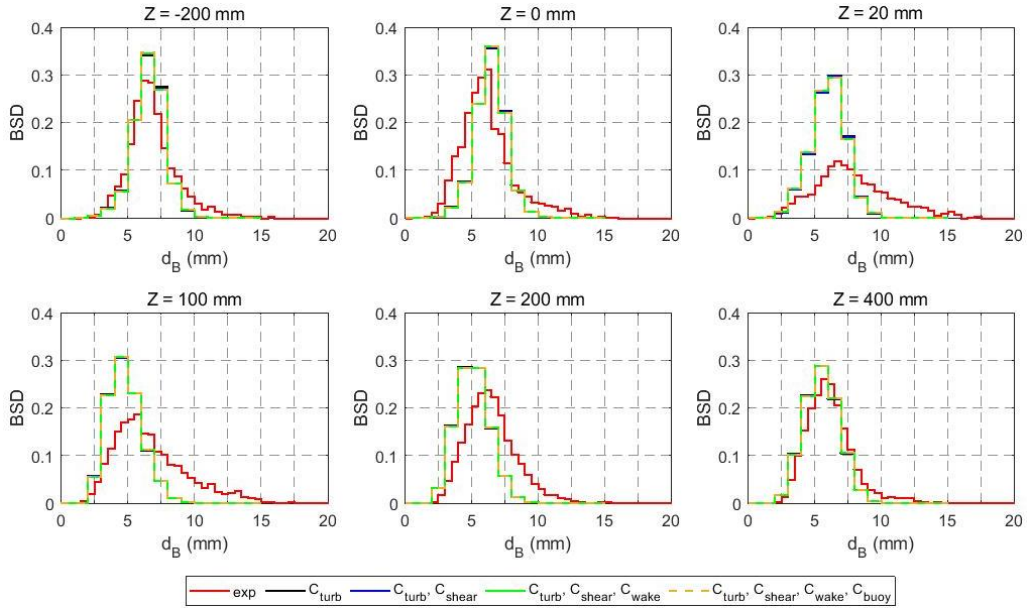


Figure 16: Comparison of bubble coalescence mechanisms for test case 072: C_{turb} , $C_{turb} + C_{shear}$, $C_{turb} + C_{shear} + C_{wake}$ and $C_{turb} + C_{shear} + C_{wake} + C_{buoy}$ (a legend is given below the graphs).

5.3.2 Bubble breakup mechanisms

Bubble breakup takes place due to flow stresses that act on the bubble surface. As mentioned in Section 5.3, there are different mechanisms causing bubble breakup. Figure 17 presents the impacts of turbulent fluctuation (B_{turb}), laminar shear (B_{shear}) and interfacial slip (B_{slip}) on the bubble size distributions for the varied Z positions. B_{shear} and B_{slip} give almost similar results for every Z positions. Also, as can be seen from Figure 18, laminar shear and interfacial slip play a negligible effect in the breakup, since it is mainly caused by turbulence.

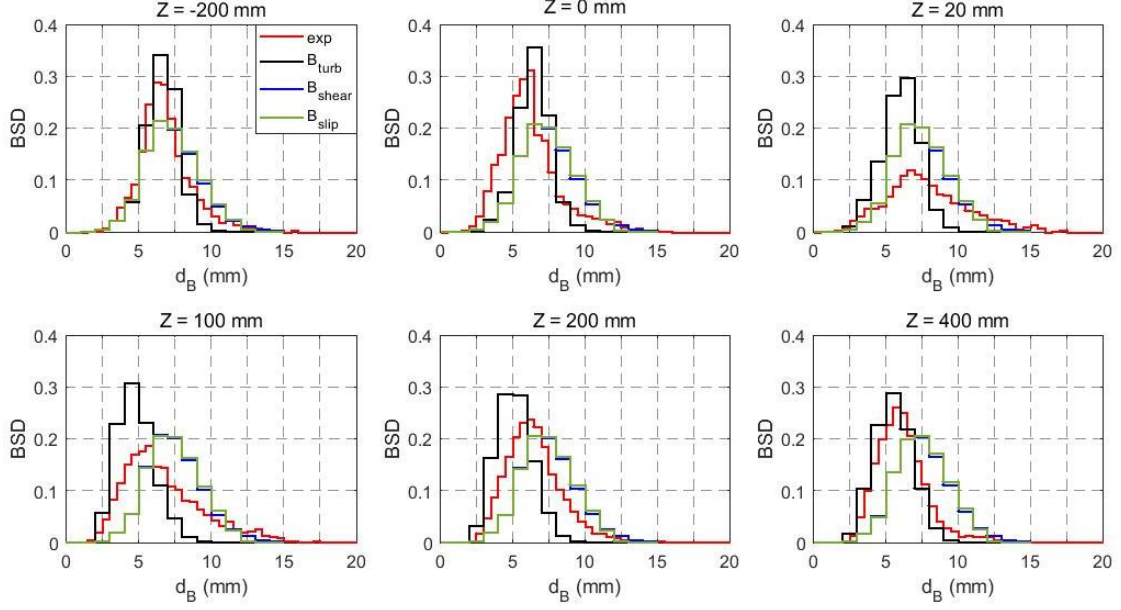


Figure 17: Comparison of bubble breakup mechanisms for test 072: B_{turb} , B_{shear} and B_{slip} (a legend is given in the first graph).

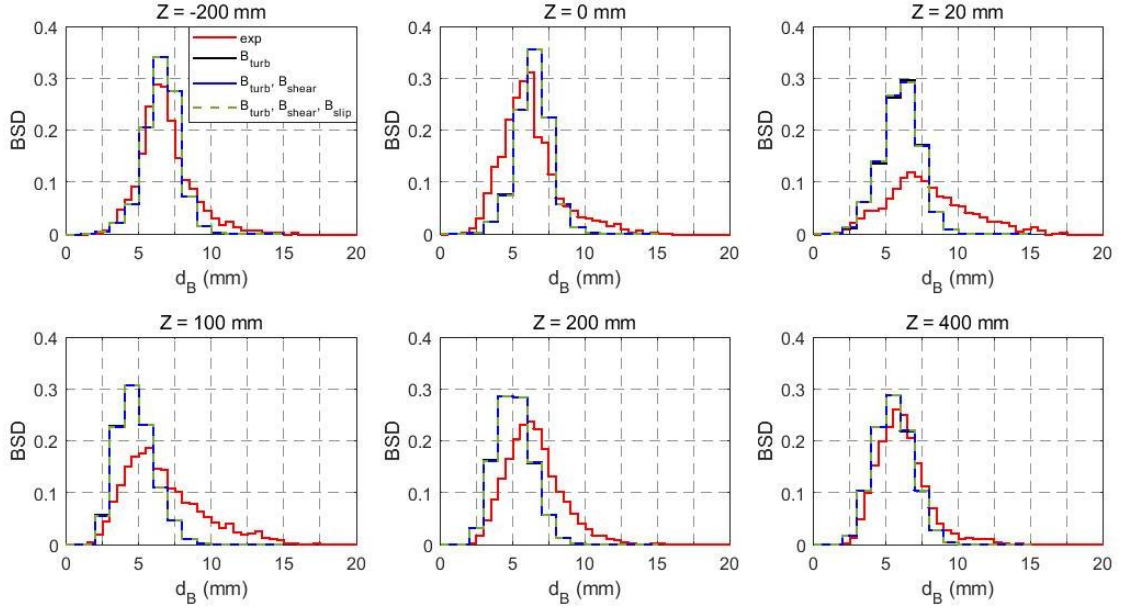


Figure 18: Comparison of bubble breakup mechanisms for test 072: B_{turb} , $B_{turb} + B_{shear}$ and $B_{turb} + B_{shear} + B_{slip}$ (a legend is given in the first graph).

As can be seen from Figure 15 to 18, other mechanisms than turbulence fluctuation have negligible effects. Thus, we considered only the turbulence fluctuation mechanism to model the breakup and coalescence in this study.

Figure 19 and Figure 20 present the bubble size distribution at different Z positions for both test cases. The bubble size distribution (BSD) is determined as gas volume fraction of each bubble size class divided by the class width and total gas void fraction. For the standard MUSIG model, there is a good agreement of simulation and experiment at position $Z = -200$ mm for test case 072. Although the simulation gives satisfying results for the larger bubbles ($d_B > 7.5$ mm) at position $Z = 0$ mm, it is underestimated for smaller ones ($d_B < 6.5$ mm). Here, slight breakup and coalescence tendency as compared to position $Z = -200$ mm is observed in the experiment, but the model captures none of them. At positions $Z = 20$ mm, $Z = 100$ mm and $Z = 200$ mm, the gas fraction of the bubbles in the size class

below 2.5 mm are well predicted. However, the simulation overestimates the gas fraction of bubbles around $2.5 \text{ mm} < d_B < 7.5 \text{ mm}$ for position $Z = 20 \text{ mm}$ and around $2.5 \text{ mm} < d_B < 6.5 \text{ mm}$ for positions $Z = 100 \text{ mm}$ and $Z = 200 \text{ mm}$, but underestimates in the remaining size classes for all three positions. Behind the obstacle, more coalescence events take place leading to a coalescence-dominant trend in the experiments, which is obviously under-predicted by the model. From position $Z = 200 \text{ mm}$ to $Z = 400 \text{ mm}$ bubble breakup is slightly overweighted, while the model predicts almost no change. However, similar to position $Z = -200 \text{ mm}$, good agreement is captured at position $Z = 400 \text{ mm}$ again. The updated MUSIG model predicts a slightly larger coalescence to breakup ratio, which leads to a larger mean bubble size as shown in Figure 11.

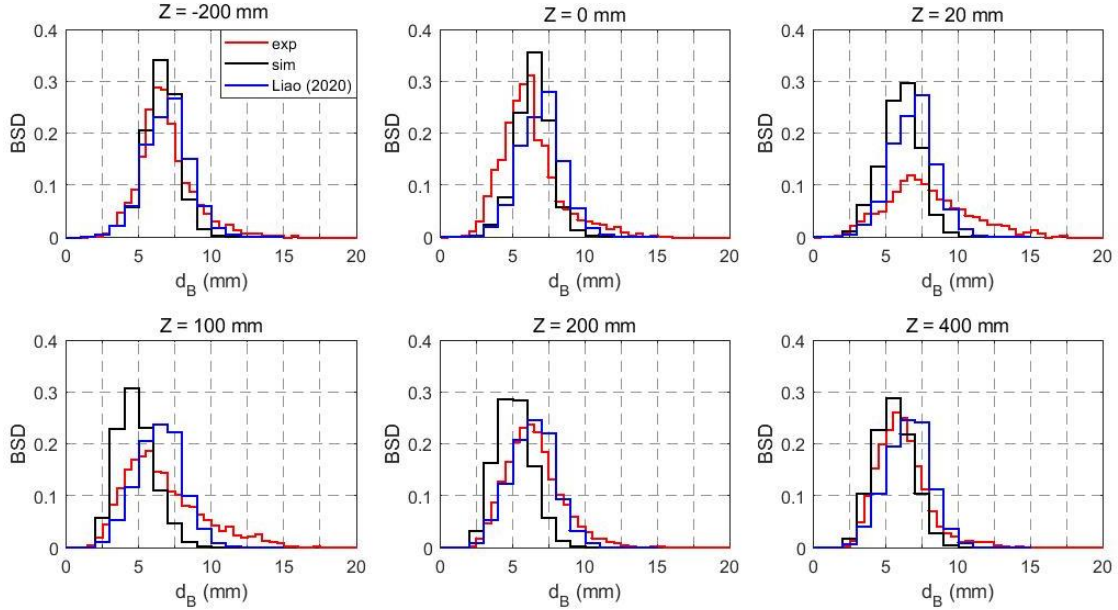


Figure 19: Bubble size distribution at different sections for test case 072 (a legend is given in the first graph).

For the standard MUSIG model, test case 074 shows similar tendencies as compared to test case 072. Good agreement is obtained at position $Z = -200 \text{ mm}$. However, a slight coalescence trend from position $Z = -200 \text{ mm}$ to $Z = 0 \text{ mm}$ is observed in the experiment, while in the simulation coalescence and breakup are almost in balance. In addition, from position $Z = 0 \text{ mm}$ to $Z = 20 \text{ mm}$ breakup seems to be dominant, which may be captured in the simulation, but the breakup rate is highly overestimated. One of the reasons may be the overprediction of the turbulence dissipation rate. Further, slight coalescence is observed again in the experiment from position $Z = 0 \text{ mm}$ to $Z = 20 \text{ mm}$ that cannot be captured by the simulation. Unlike for test case 072, the obvious inconsistency between experiment and simulation continues to exist also at position $Z = 400 \text{ mm}$.

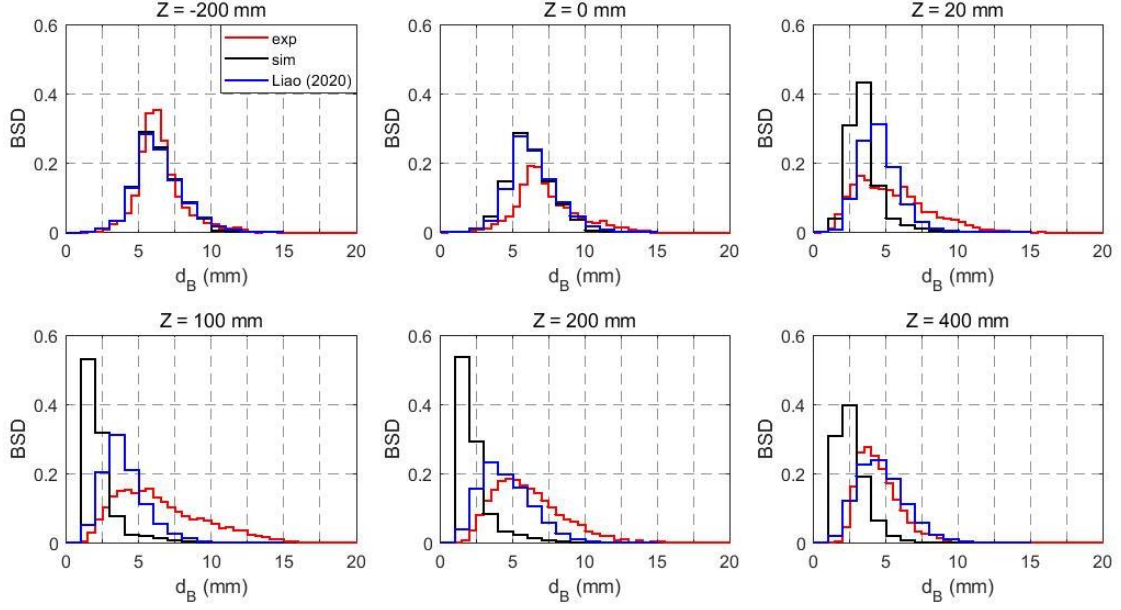


Figure 20: Bubble size distribution at different sections for test case 074 (a legend is given in the first graph).

On the one hand, the updated MUSIG model gives similar results to standard one at the positions $Z = -200$ mm and $Z = 0$ mm, where the coalescence and breakup is nearly in equilibrium. On the other hand, it improves the downstream results significantly, and captures the coalescence trend well. The improvement increases from position $Z = 20$ mm to $Z = 400$ mm. However, there are still notable inconsistencies between experiments and updated MUSIG predictions at the positions $Z = 20$ mm and $Z = 100$ mm where the flow is highly complex.

6. Conclusion

We investigated the performance of state-of-the-art bubble breakup and coalescence modelling for 3D bubbly flow around an obstacle in a pipe. For this purpose, we performed simulations with the homogeneous MUSIG model for two different liquid velocities and compared gas velocity, void fraction, mean bubble diameter and bubble size distribution with 3D UFXCT data. A main feature of the flow is that there is a vortex region behind the obstacle. This vortex region causes a strong gas accumulation downstream the obstacle. While in the high-velocity case void accumulates directly behind the obstacle it does so further downstream in the low-velocity case. The reason is that the obstacle leads to a downstream wake region whose length increases with velocity. Thus, this wake region causes void accumulation depending on the area where it acts.

While the prediction of axial and radial void fractions for the low-velocity case agrees generally well with the experimental results for both the upstream and downstream region of the obstacle, the prediction for the high-velocity case overestimates the average void fraction compared to experimental data downstream of the obstacle. Moreover, downstream of the obstacle the average bubble diameter and average gas velocity are underestimated while they are in good agreement for both the low-velocity and high-velocity cases upstream of the obstacle.

Considering the BSD, we found that coalescence is the dominant mechanism behind the obstacle for the low-velocity case in the experiments. However, the simulations could not capture it. In addition, for the high-velocity case the breakup rate is highly overestimated compared to the experimental data. The difference between experimental data and numerical results may be because of the overestimation of turbulence, which is related to the shear-induced and bubble-induced turbulence models. Simulation

results show that the predicted coalescence rate of all mechanisms might be negligible in comparison to breakup rates since all the coalescence mechanisms provide approximately the same predictions. In addition, it is clear that turbulence is the dominant mechanism for both breakup and coalescence.

The performance of the updated MUSIG model recently developed by Liao (2020) was also tested in the present study. The results show that the updated MUSIG model predicts an obviously lower breakup rate. Consequently, it is able to reproduce the coalescence-dominant trend for the low-velocity test, and predicts a reasonable mean bubble size for the high-velocity test, where turbulence-induced breakup is significant. Investigation on the effect of two-phase turbulence models and improving the coalescence and breakup model in the updated MUSIG model will be topics of future work.

As already mentioned, the low-velocity case shows good agreement with the experimental data downstream of the obstacle, whereas this is not the case for the high-velocity case. The explanation of void fraction overestimation for the high-velocity case may be due to more than one reason. Firstly, applied bubble force models, which are widely used in the literature, do not consider the turbulence effects. Turbulence effects are thought to have an impact, especially on drag force. Secondly, the bubble breakup and coalescence model may need to be improved. Thirdly, the applicability of bubble-induced turbulence that was used for the simulations is still not clear for high shear-induced turbulence cases, since it has been obtained under low turbulence conditions.

References

- Auton, T. R., Hunt, J. C. R., & Prudhomme, M. (1988). The Force Exerted on a Body in Inviscid Unsteady Non-Uniform Rotational Flow. *Journal of Fluid Mechanics*, 197, 241-257. doi:10.1017/S0022112088003246
- Besagni, G., Guedon, G. R., & Inzoli, F. (2018). Computational fluid-dynamic modeling of the mono-dispersed homogeneous flow regime in bubble columns. *Nuclear Engineering and Design*, 331, 222-237. doi:10.1016/j.nucengdes.2018.03.003
- Burns, A. D., Frank, T., Hamill, I., & Shi, J.-M. (2004). *The Favre averaged drag model for turbulent dispersion in Eulerian multi-phase flows*. Paper presented at the 5th International Conference on Multiphase Flow, ICMF, Yokohama, Japan.
- Colombo, M., & Fairweather, M. (2015). Multiphase turbulence in bubbly flows: RANS simulations. *International Journal of Multiphase Flow*, 77, 222-243. doi:10.1016/j.ijmultiphaseflow.2015.09.003
- Colombo, M., & Fairweather, M. (2019). Influence of multiphase turbulence modelling on interfacial momentum transfer in two-fluid Eulerian-Eulerian CFD models of bubbly flows. *Chemical Engineering Science*, 195, 968-984. doi:10.1016/j.ces.2018.10.043
- Frank, T., Zwart, P. J., Krepper, E., Prasser, H. M., & Lucas, D. (2008). Validation of CFD models for mono- and polydisperse air-water two-phase flows in pipes. *Nuclear Engineering and Design*, 238(3), 647-659. doi:10.1016/j.nucengdes.2007.02.056
- Hosokawa, S., Tomiyama, A., Misaki, S., & Hamada, T. (2002). *Lateral migration of single bubbles due to the presence of wall*. Paper presented at the Proceedings of the ASME Joint U.S.-European Fluids Engineering Division Conference, FEDSM2002, Montreal, Canada.
- Ishii, M., & Zuber, N. (1979). Drag Coefficient and Relative Velocity in Bubbly, Droplet or Particulate Flows. *Aiche Journal*, 25(5), 843-855. doi:10.1002/aic.690250513
- Jareteg, K., Strom, H., Sasic, S., & Demaziere, C. (2017). On the dynamics of instabilities in two-fluid models for bubbly flows. *Chemical Engineering Science*, 170, 184-194. doi:10.1016/j.ces.2017.03.063
- Jin, D., Xiong, J. B., & Cheng, X. (2019). Investigation on interphase force modeling for vertical and inclined upward adiabatic bubbly flow. *Nuclear Engineering and Design*, 350, 43-57. doi:10.1016/j.nucengdes.2019.05.005

- Krepper, E., Beyer, M., Frank, T., Lucas, D., & Prasser, H. M. (2009). CFD modelling of polydispersed bubbly two-phase flow around an obstacle. *Nuclear Engineering and Design*, 239(11), 2372-2381. doi:10.1016/j.nucengdes.2009.06.015
- Liao, Y. X. (2020). Update to the MUSIG model in ANSYS CFX for reliable modelling of bubble coalescence and breakup. *Applied Mathematical Modelling*, 81, 506-521. doi:10.1016/j.apm.2020.01.033
- Liao, Y. X., Lucas, D., Krepper, E., & Schmidtke, M. (2011). Development of a generalized coalescence and breakup closure for the inhomogeneous MUSIG model. *Nuclear Engineering and Design*, 241(4), 1024-1033. doi:10.1016/j.nucengdes.2010.04.025
- Liao, Y. X., Ma, T., Liu, L., Ziegenhein, T., Krepper, E., & Lucas, D. (2018). Eulerian modelling of turbulent bubbly flow based on a baseline closure concept. *Nuclear Engineering and Design*, 337, 450-459. doi:10.1016/j.nucengdes.2018.07.021
- Liao, Y. X., Rzehak, R., Lucas, D., & Krepper, E. (2015). Baseline closure model for dispersed bubbly flow: Bubble coalescence and breakup. *Chemical Engineering Science*, 122, 336-349. doi:10.1016/j.ces.2014.09.042
- Lo, S. (1996). *Application of the MUSIG model to bubbly flows*. Paper presented at the AEAT-1096, AEA Technology.
- Luo, H., & Svendsen, H. F. (1996). Theoretical model for drop and bubble breakup in turbulent dispersions. *Aiche Journal*, 42(5), 1225-1233. doi:10.1002/aic.690420505
- Ma, T., Santarelli, C., Ziegenhein, T., Lucas, D., & Frohlich, J. (2017). Direct numerical simulation-based Reynolds-averaged closure for bubble-induced turbulence. *Physical Review Fluids*, 2(3). doi:10.1103/PhysRevFluids.2.034301
- Menter, F. R. (1994). 2-Equation Eddy-Viscosity Turbulence Models for Engineering Applications. *Aiaa Journal*, 32(8), 1598-1605. doi:10.2514/3.12149
- Neumann-Kipping, M., Bieberle, A., & Hampel, U. (2020). Investigations on bubbly two-phase flow in a constricted vertical pipe. *International Journal of Multiphase Flow*, 130. doi:10.1016/j.ijmultiphaseflow.2020.103340
- Parekh, J., & Rzehak, R. (2018). Euler-Euler multiphase CFD-simulation with full Reynolds stress model and anisotropic bubble-induced turbulence. *International Journal of Multiphase Flow*, 99, 231-245. doi:10.1016/j.ijmultiphaseflow.2017.10.012
- Prasser, H. M., Beyer, M., Frank, T., Al Issaa, S., Carl, H., Pietruske, H., & Schutz, P. (2008). Gas-liquid flow around an obstacle in a vertical pipe. *Nuclear Engineering and Design*, 238(7), 1802-1819. doi:10.1016/j.nucengdes.2007.11.007
- Prince, M. J., & Blanch, H. W. (1990). Bubble Coalescence and Break-up in Air-Sparged Bubble-Columns. *Aiche Journal*, 36(10), 1485-1499. doi:10.1002/aic.690361004
- Rzehak, R., & Krepper, E. (2013). CFD modeling of bubble-induced turbulence. *International Journal of Multiphase Flow*, 55, 138-155. doi:10.1016/j.ijmultiphaseflow.2013.04.007
- Rzehak, R., Krepper, E., & Lifante, C. (2012). Comparative study of wall-force models for the simulation of bubbly flows. *Nuclear Engineering and Design*, 253, 41-49. doi:10.1016/j.nucengdes.2012.07.009
- Rzehak, R., Ziegenhein, T., Kriebitzsch, S., Krepper, E., & Lucas, D. (2017). Unified modeling of bubbly flows in pipes, bubble columns, and airlift columns. *Chemical Engineering Science*, 157, 147-158. doi:10.1016/j.ces.2016.04.056
- Simonin, O., & Viollet, P. L. (1990). *Predictions of an oxygen droplet pulverization in a compressible subsonic coflowing hydrogen flow*. Paper presented at the Numerical Methods for Multiphase Flows, FED91.
- Tas-Koehler, S., Lecrivain, G., Krepper, E., Unger, S., & Hampel, U. (2020). Numerical investigation on the effect of transversal fluid field deformation on heat transfer in a rod bundle with mixing vanes. *Nuclear Engineering and Design*, 361. doi:10.1016/j.nucengdes.2020.110575
- Tomiyama, A., Kataoka, I., Zun, I., & Sakaguchi, T. (1998). Drag coefficients of single bubbles under normal and micro gravity conditions. *Jsme International Journal Series B-Fluids and Thermal Engineering*, 41(2), 472-479. doi:10.1299/jsmeb.41.472
- Tomiyama, A., Tamai, H., Zun, I., & Hosokawa, S. (2002). Transverse migration of single bubbles in simple shear flows. *Chemical Engineering Science*, 57(11), 1849-1858. doi:10.1016/S0009-2509(02)00085-4

609 Troshko, A. A., & Hassan, Y. A. (2001). A two-equation turbulence model of turbulent bubbly flows.
610 *International Journal of Multiphase Flow*, 27(11), 1965-2000. doi:10.1016/S0301-
611 9322(01)00043-X
612 Yeoh, G. H., & Tu, J. Y. (2009). *Computational Techniques for Multiphase Flows*: Butterworth-
613 Heinemann.
614

FIGURES

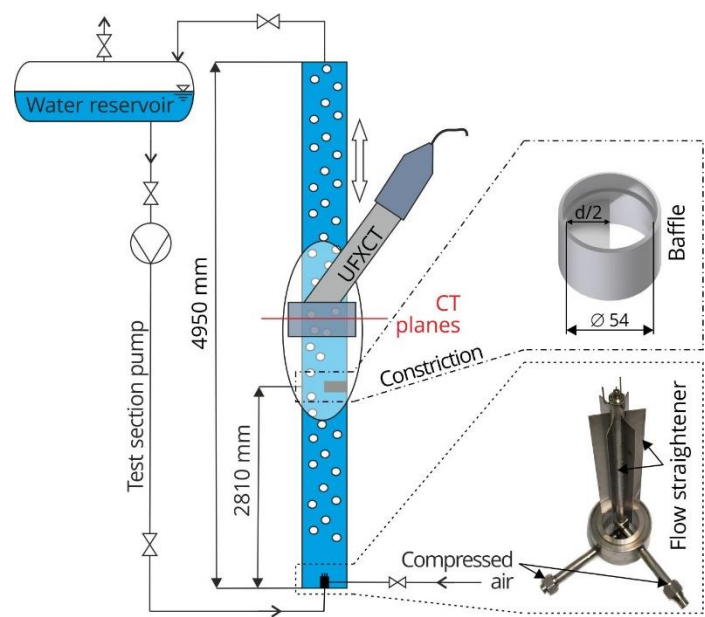


Figure 1: Schematic representations of the vertical test section (left) with details of the gas injection module (bottom right) and the flow obstacle for generation of three-dimensional flow fields (top right).

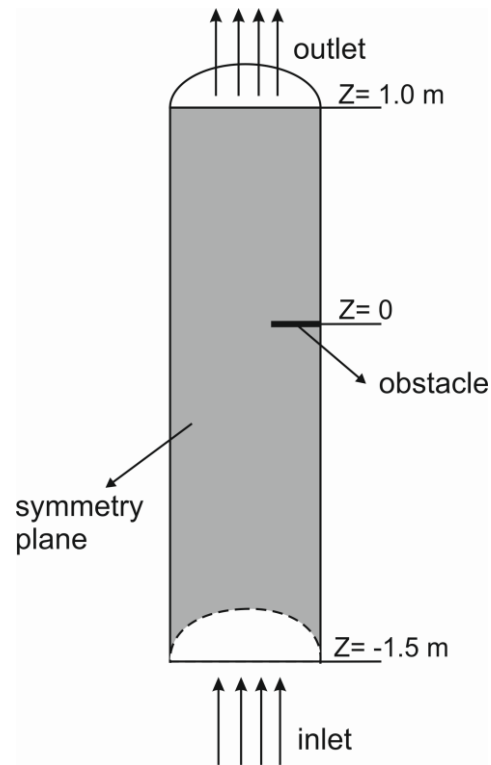


Figure 2: Schematic view of computational domain.

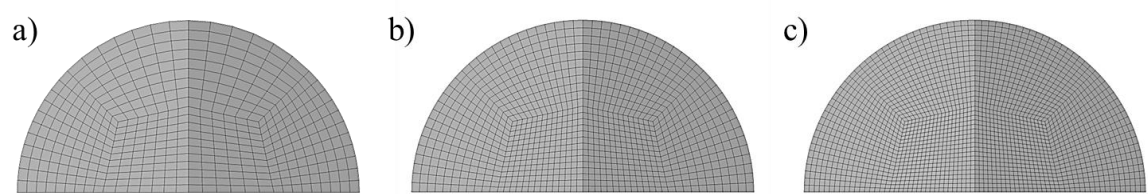


Figure 3: Mesh views: a) mesh 1 b) mesh 2 and c) mesh 3.

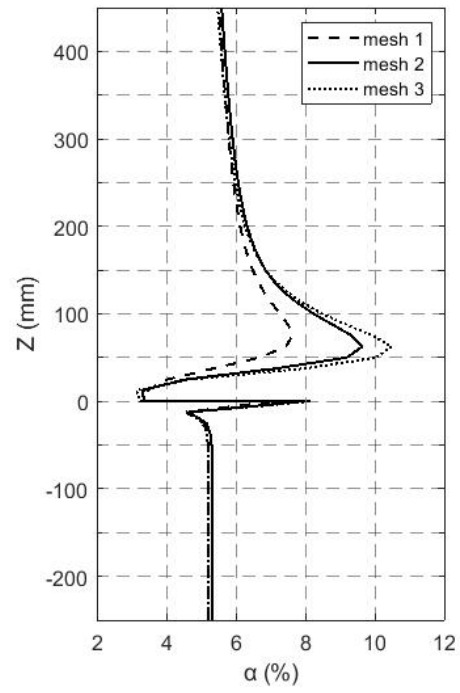


Figure 4: Effect of grid refinement on the average gas fraction for test 072.

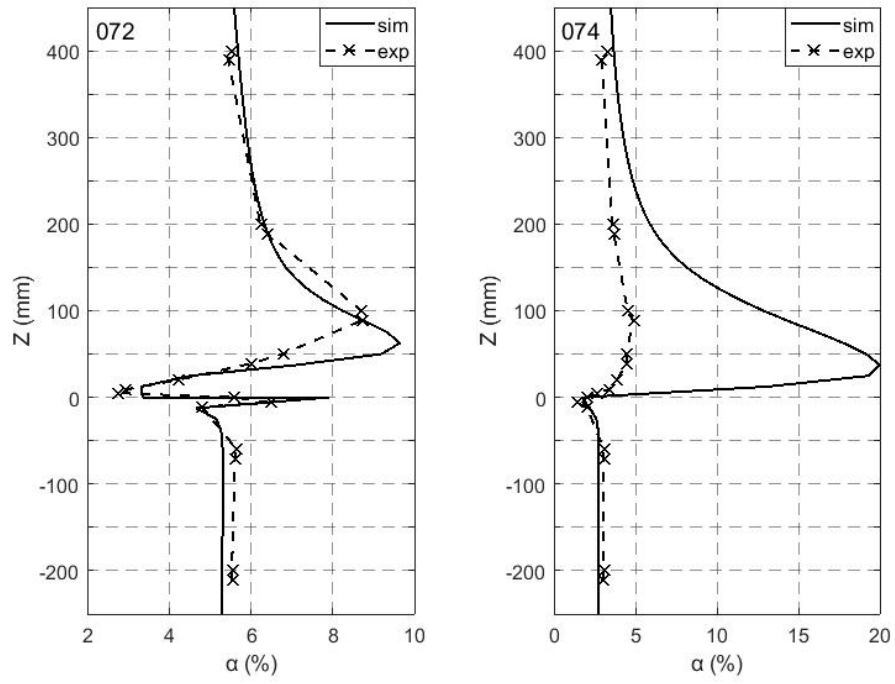


Figure 5: Cross-sectional averaged void fraction along the axial direction for test cases 072 and 074.

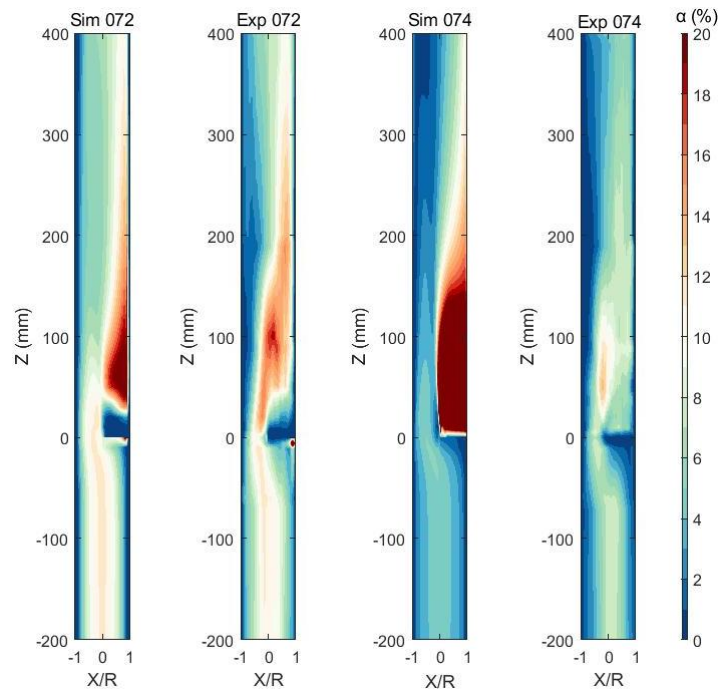


Figure 6: Visualization plots of simulated and measured void fraction for test cases 072 and 074.

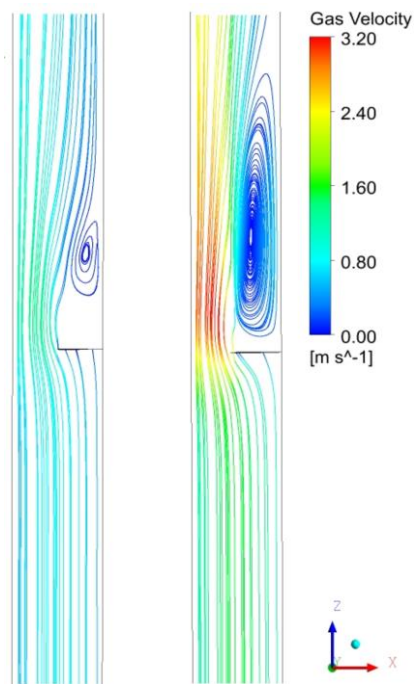


Figure 7: Streamline for test 072 (left) and 074 (right).

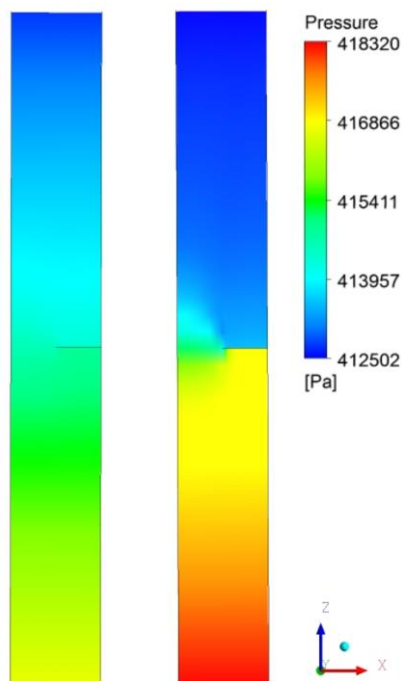


Figure 8: Pressure distribution for test 072 (left) and 074 (right).

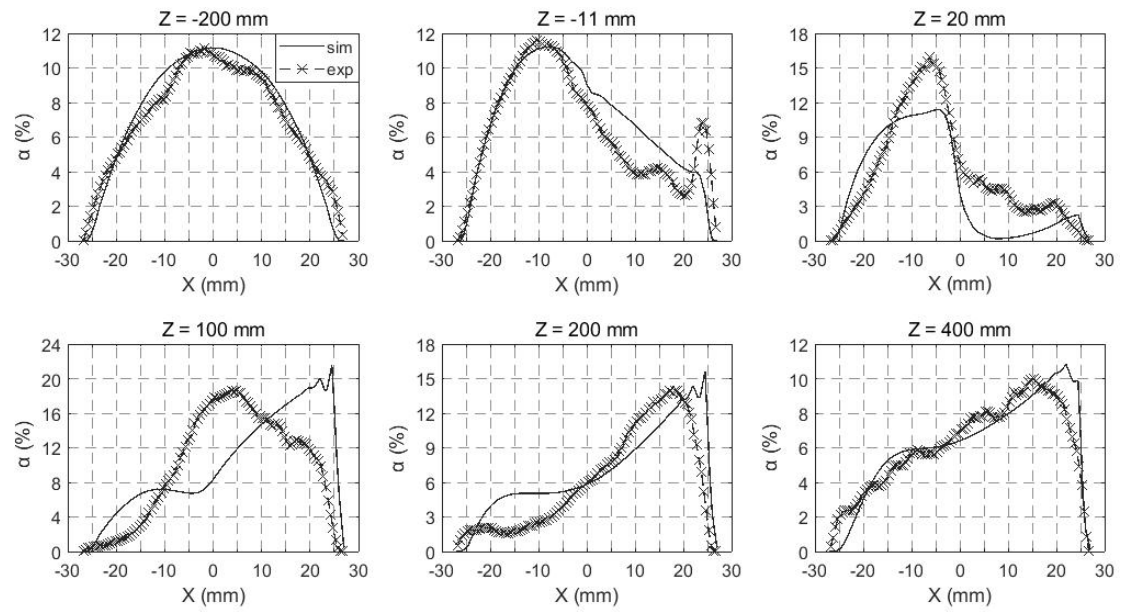


Figure 9: Radial gas fraction distribution for test 072 for different Z positions.

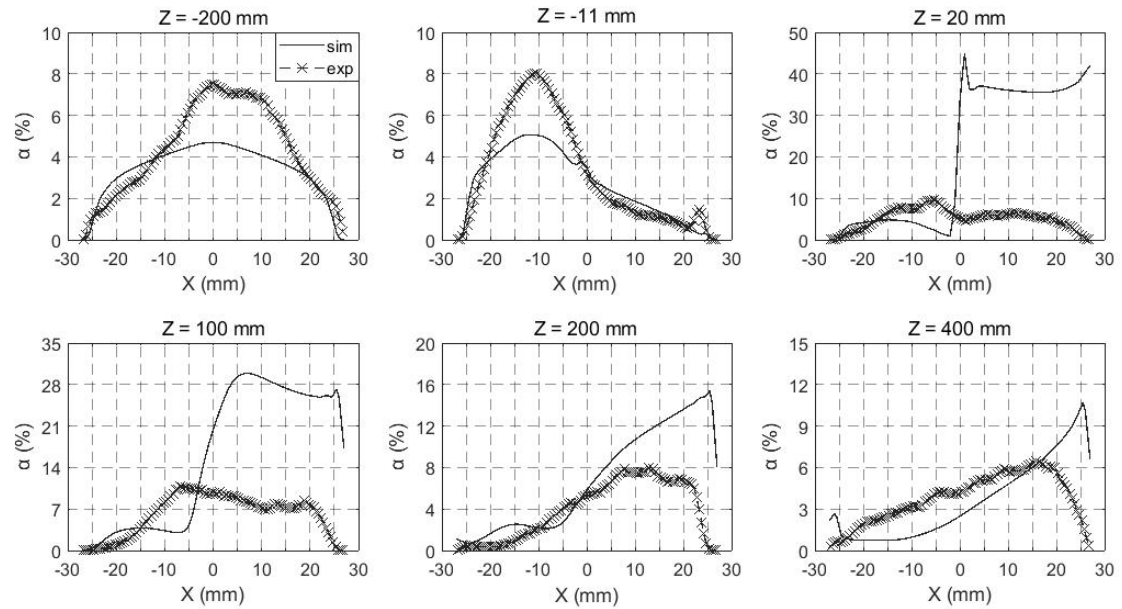


Figure 10: Radial gas fraction distribution for test 074 for different Z positions.

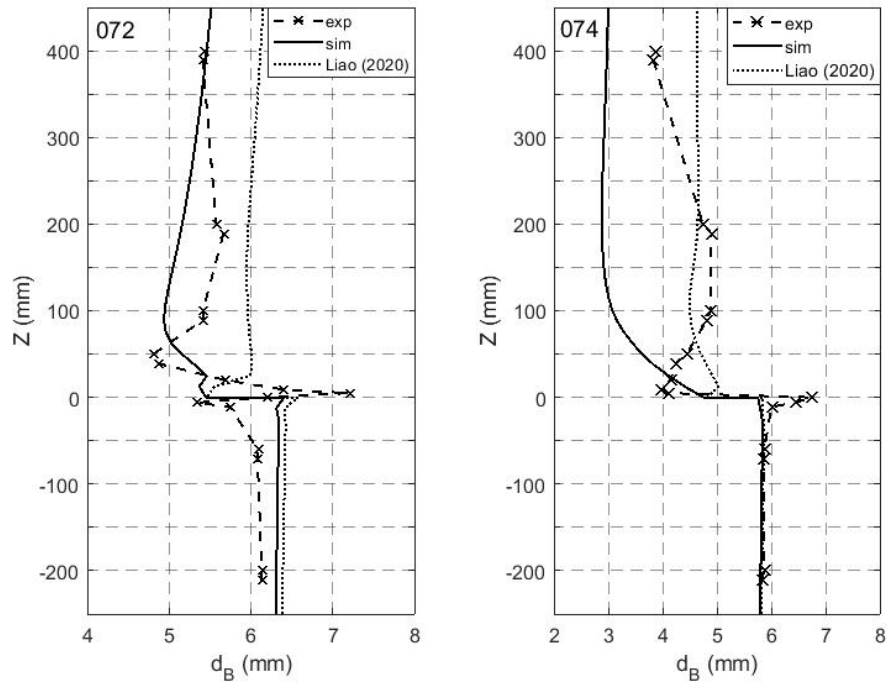


Figure 11: Average bubble diameter for test cases 072 and 074.

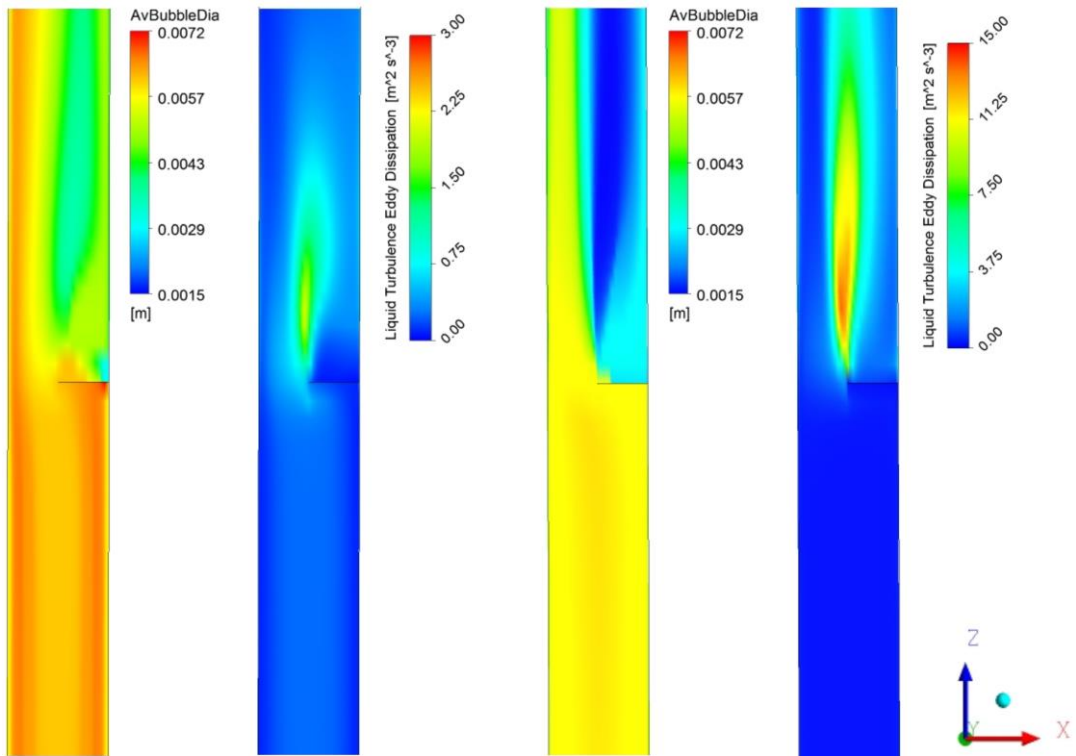


Figure 12: Comparison of average bubble diameter and turbulent dissipation for test cases 072 (left) and 074 (right).

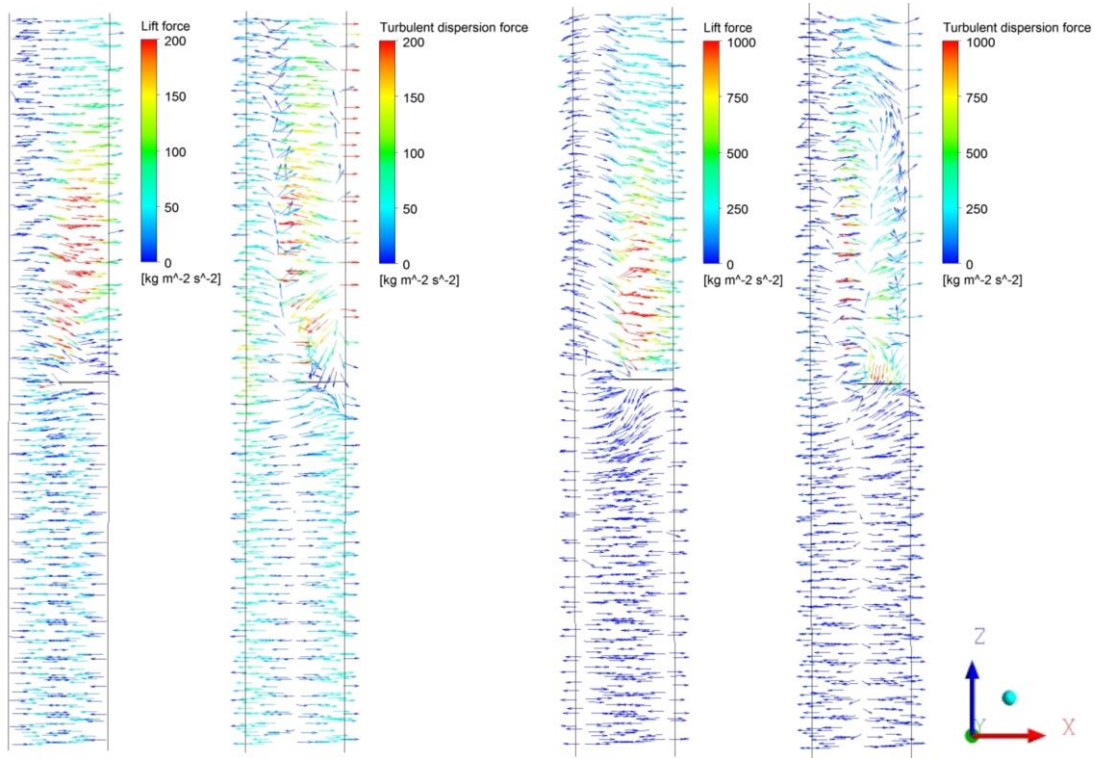


Figure 13: Bubble lift and turbulent dispersion vectors for test 072 (left) and 074 (right).

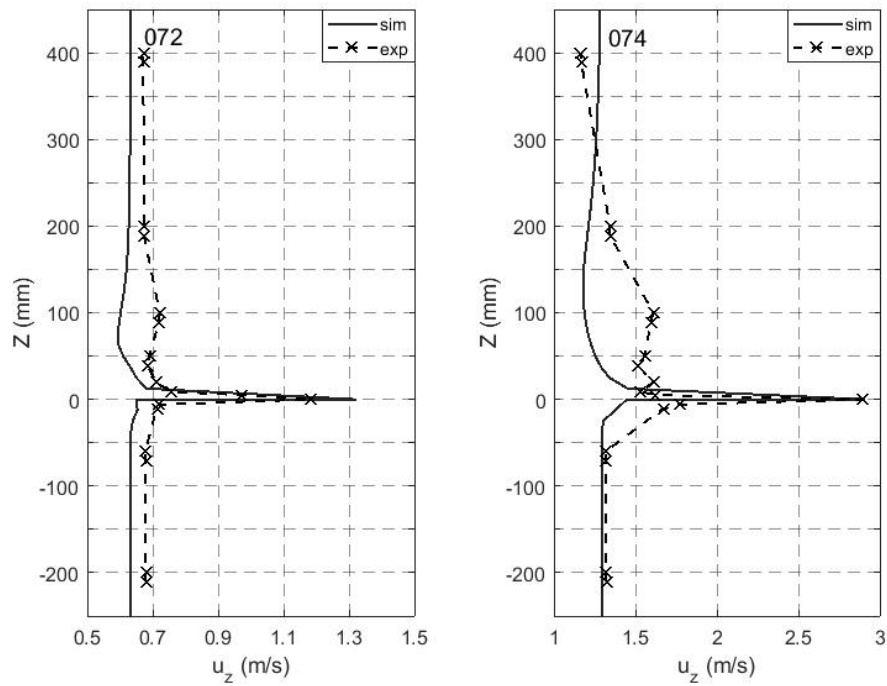


Figure 14: Cross-sectional averaged gas velocity for test 072 and 074.

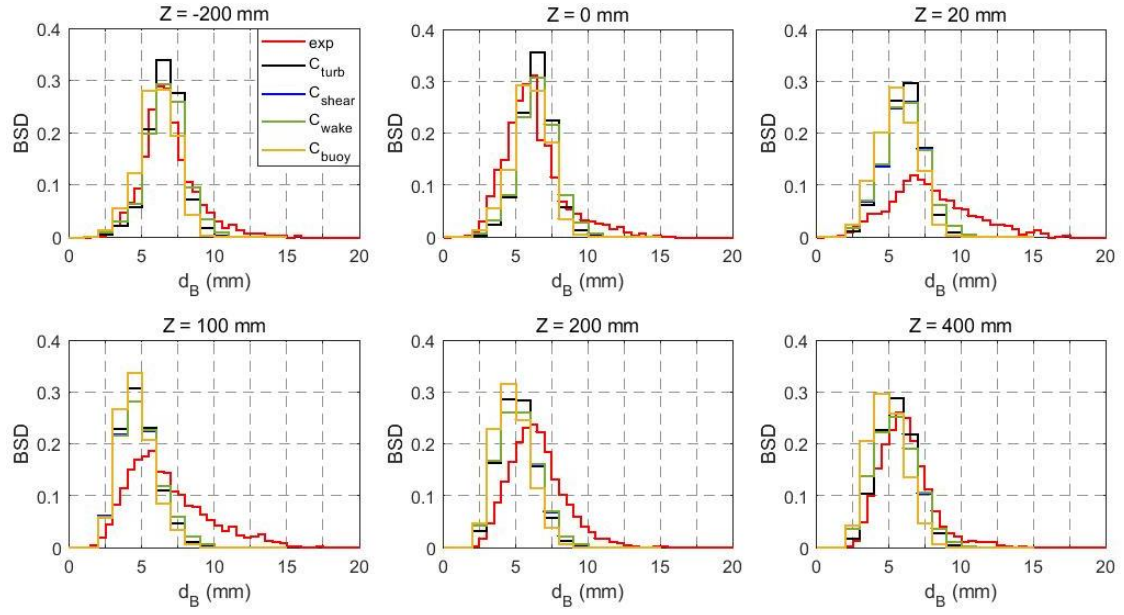


Figure 15: Comparison of bubble coalescence mechanisms for test case 072: C_{turb} , C_{shear} , C_{wake} and C_{buoy} (a legend is given in the first graph).

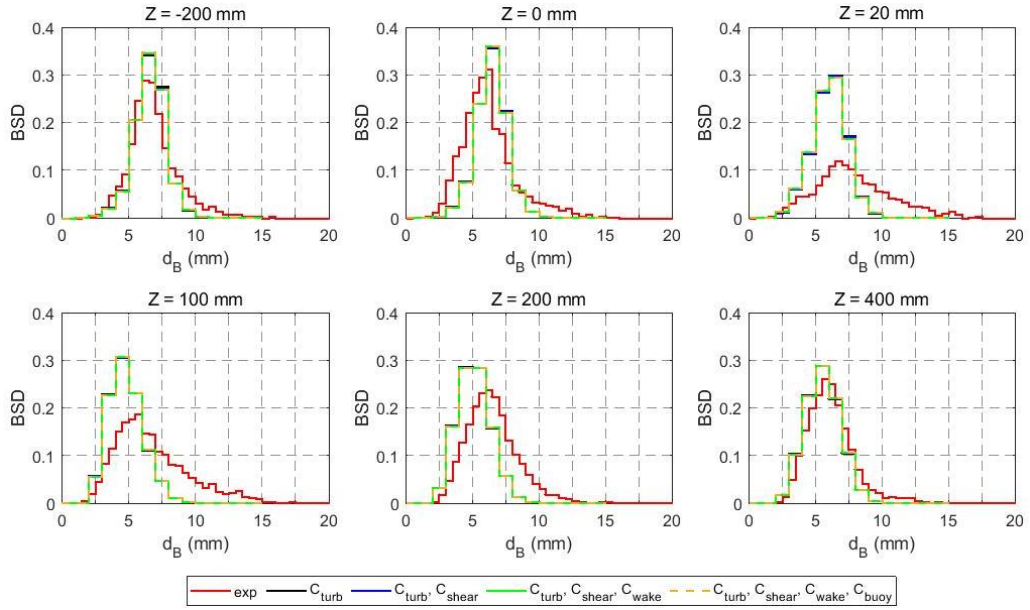


Figure 16: Comparison of bubble coalescence mechanisms for test case 072: C_{turb} , $C_{\text{turb}} + C_{\text{shear}}$, $C_{\text{turb}} + C_{\text{shear}} + C_{\text{wake}}$ and $C_{\text{turb}} + C_{\text{shear}} + C_{\text{wake}} + C_{\text{buoy}}$ (a legend is given below the graphs).

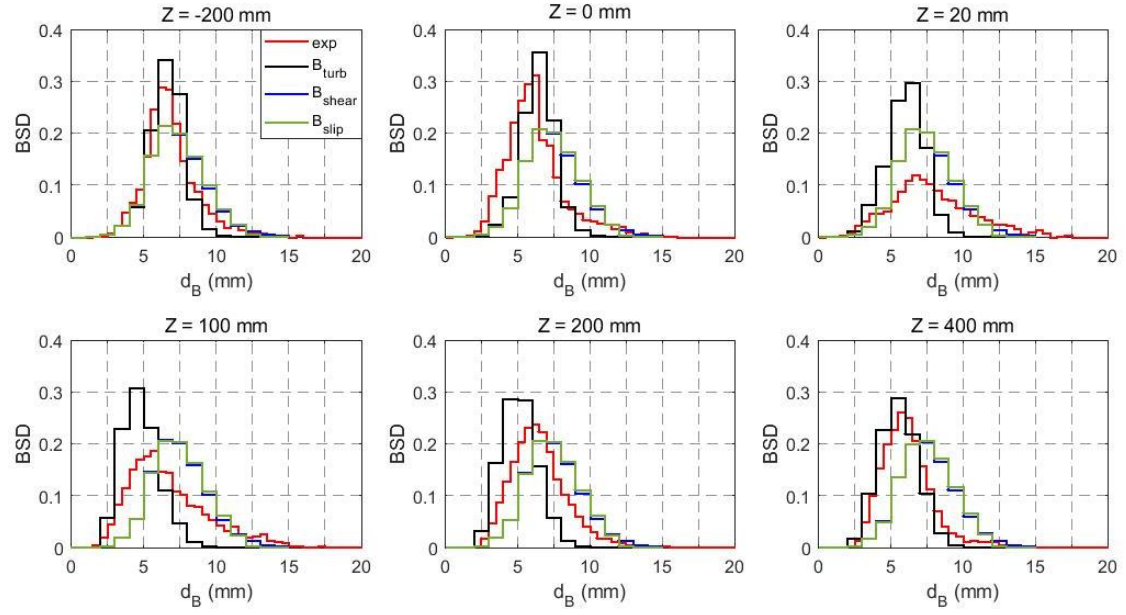


Figure 17: Comparison of bubble breakup mechanisms for test 072: B_{turb} , B_{shear} and B_{slip} (a legend is given in the first graph).

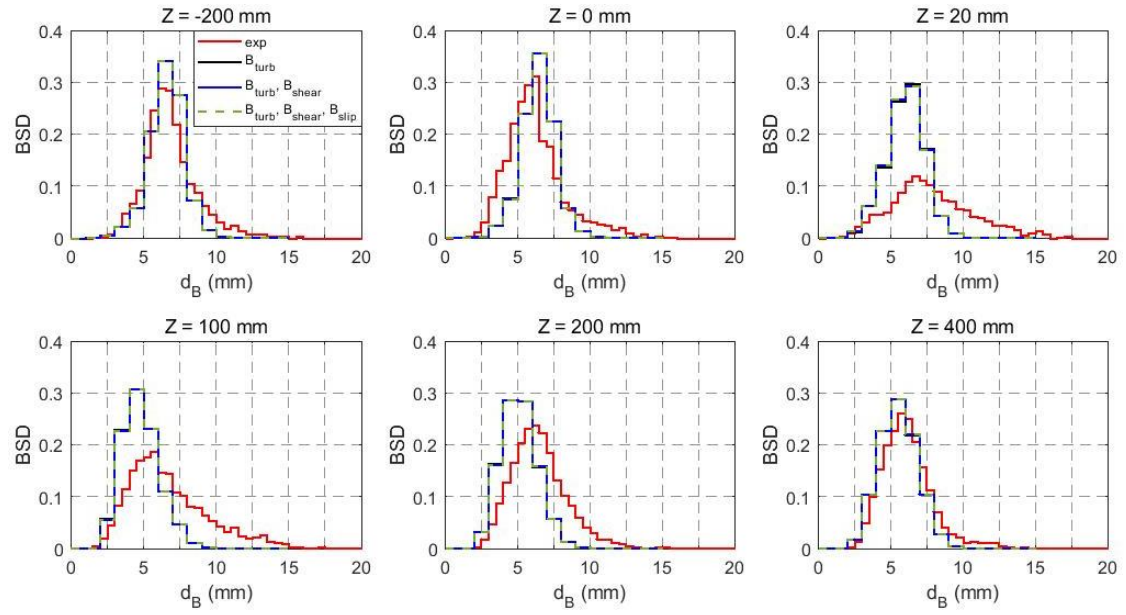


Figure 18: Comparison of bubble breakup mechanisms for test 072: B_{turb} , $B_{\text{turb}} + B_{\text{shear}}$ and $B_{\text{turb}} + B_{\text{shear}} + B_{\text{slip}}$ (a legend is given in the first graph).

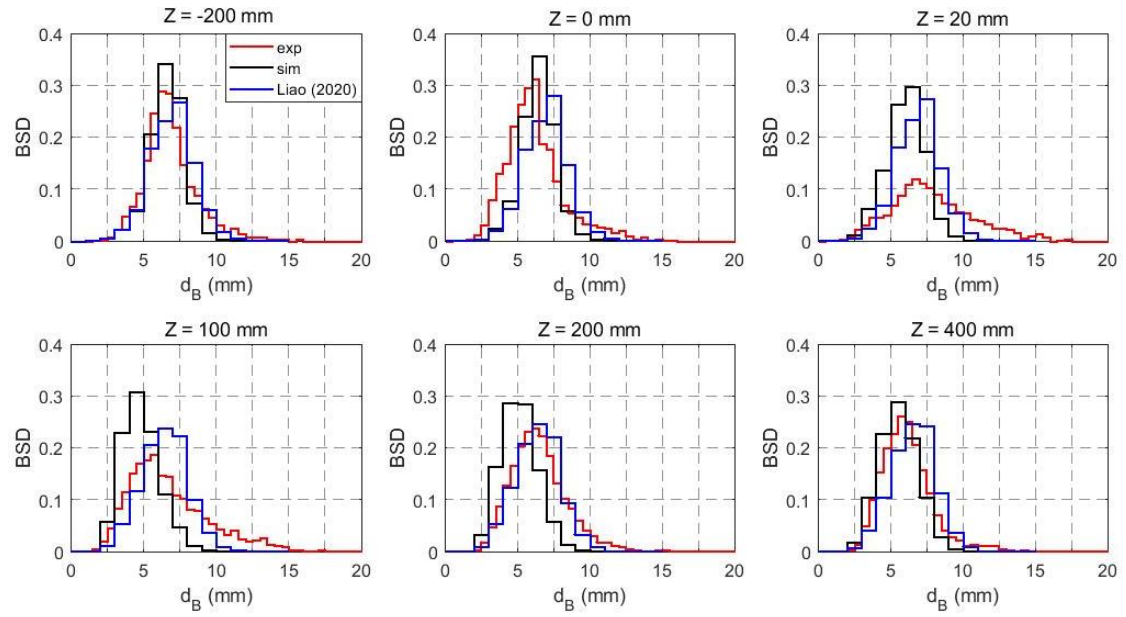


Figure 19: Bubble size distribution at different sections for test case 072 (a legend is given in the first graph).

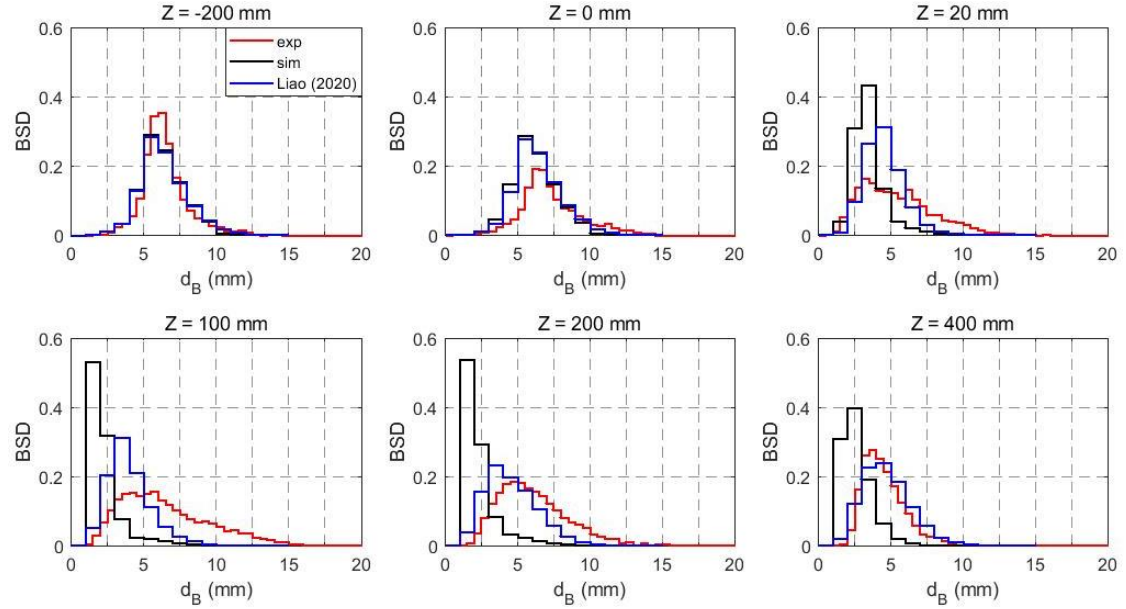


Figure 20: Bubble size distribution at different sections for test case 074 (a legend is given in the first graph).

TABLES

Table 1: Experimental operating conditions based on combinations of liquid and gas superficial velocities.

Test run	j_l [m·s ⁻¹]	j_g [m·s ⁻¹]
#072	0.4050	0.0368
#074	1.0170	0.0368

Table 2: Image plane identifier along the vertical test section with relative distances of the upper image plane to the center of the flow constriction.

Identifier	A	B	C	D	E	F	G	H	I
Z (mm)	-200	-60	0	5	20	50	100	200	400

Table 3: Mathematical description for interfacial force coefficients.

Force	Reference	Mathematical description
Drag	Ishii <i>et al.</i> (1979)	$C_D = \max[C_{Dsphere}, \min(C_{Dellipse}, C_{Dcap})]$ $C_{Dsphere} = \frac{24}{Re_d} (1 + 0.1Re_d^{3/4}), C_{Dellipse} = \frac{2}{3} \sqrt{Eo}, C_{Dcap} = \frac{8}{3}$
Lift	Tomiyama <i>et al.</i> (2002)	$C_L = \begin{cases} \min[0.288 \tanh(0.121Re), f(Eo_\perp)] & Eo_\perp < 4 \\ f(Eo_\perp) & 4 < Eo_\perp < 10 \\ -0.27 & 10 < Eo_\perp \end{cases}$ $f(Eo_\perp) = 0.00105Eo_\perp^3 - 0.0159Eo_\perp^2 - 0.0204Eo_\perp + 0.474$ $Eo_\perp = \frac{g(\rho_L - \rho_L)d_\perp^2}{\sigma} \quad d_\perp = d_B \sqrt[3]{1 + 0.163 Eo^{0.757}}$
Wall lubrication	Hosokawa <i>et al.</i> (2002)	$C_W(y) = f(Eo) \left(\frac{d_B}{2y} \right)^2, \quad f(Eo) = 0.021Eo$
Turbulent dispersion	Burns <i>et al.</i> (2004)	Favre averaging the drag force
Virtual mass	Auton <i>et al.</i> (1988)	Constant coefficient $C_{VM} = 0.5$

Conflict of Interest

15.06.2020

Dear Editor,

The authors certify that they have no affiliations or involvement in any organization or entity with any financial interest or non-financial interest in the subject matter or materials discussed in this manuscript.

We confirm that this work is original and has not been published elsewhere, nor is it currently under consideration for publication elsewhere.

Sincerely,

Sibel Tas-Koehler

Credit Author Statement

19.10.2020

Dear Editor,

The authors are responsible and ensure an accurate description. All authors contributed to scientific content and the editorial content of the present paper. The order of the authors represents the share of the contribution to the article.

Sincerely,

Tas-Koehler Sibel, Neumann-Kipping Martin, Liao Yixiang, Krepper Eckhard, Hampel Uwe